

<https://doi.org/10.15388/vu.thesis.115>  
<https://orcid.org/0000-0002-5373-373X>

VILNIUS UNIVERSITY  
CENTER FOR PHYSICAL SCIENCES AND TECHNOLOGY

Domas  
JOKUBAUSKIS

# Development and Applications of Compact Spectroscopic Terahertz Imaging Systems Using Principles of Optical Beam Engineering

DOCTORAL DISSERTATION

Natural Sciences,  
Physics (N 002)

---

VILNIUS 2020

This dissertation was written between 2014 and 2019 in the Center for Physical Sciences and Technology. The research was supported by Research Council of Lithuania:

Mobility funding – P-DAK-19-91.

**Academic supervisor:**

**prof. habil. dr. Gintaras Valušis** (Center for Physical Sciences and Technology, Natural Sciences, Physics – N 002).

This doctoral dissertation will be defended in a public meeting of the Dissertation Defence Panel:

**Chairman – prof. habil dr. Jūras Banys** (Vilnius University, Natural Sciences, Physics – N 002).

**Members:**

**prof. dr. Artūras Jukna** ( Vilnius Gediminas Technical University, Natural Sciences, Physics – N 002);

**doc. dr. Edvardas Kazakevičius** (Vilnius University, Natural Sciences, Physics – N 002);

**dr. Ignas Nevinskas** (Center for Physical Sciences and Technology, Natural Sciences, Physics – N 002);

**dr. Evaldas Stankevičius** (Center for Physical Sciences and Technology, Natural Sciences, Physics – N 002).

The dissertation shall be defended at a public meeting of the Dissertation Defence Panel at 2 p.m. on 10<sup>th</sup> December 2020 in room A101 of the Center for Physical Sciences and Technology. Address: Saulėtekio av. 3, A101, Vilnius, Lithuania. Tel. +37052648884; e-mail: office@ftmc.lt.

The text of this dissertation can be accessed at the libraries of Center for Physical Sciences and Technology and Vilnius University, as well as on the website of Vilnius University: <http://www.vu.lt/lt/naujienos/ivykiu-kalendorius>.

**Open Access** This work is distributed under the terms of the Creative Commons Attribution 4.0 International (CC BY 4.0) License (<http://creativecommons.org/licenses/by/4.0/>) unless noted otherwise.

VILNIUS UNIVERSITETAS  
FIZINIŲ IR TECHNOLOGIJOS MOKSLŲ CENTRAS

Domas  
JOKUBAUSKIS

Kompaktiškų spektroskopinių  
terahercinių vaizdų fiksavimo  
sistemų vystymas ir taikymas  
naudojant optinio pluošto inžinerijos  
principus

**DAKTARO DISERTACIJA**

Gamtos mokslai,  
Fizika (N 002)

Disertacija rengta 2014–2019 metais Fizinių ir technologijos mokslų centre. Mokslinius tyrimus rėmė Lietuvos mokslo taryba:

Parama išvykoms – P-DAK-19-91.

**Mokslinis vadovas:**

**prof. habil. dr. Gintaras Valušis** (Fizinių ir technologijos mokslų centras, gamtos mokslai, fizika – N 002).

Gynimo taryba:

**Pirmininkas – prof. habil dr. Jūras Banys** (Vilniaus universitetas, gamtos mokslai, fizika – N 002).

**Nariai:**

**prof. dr. Artūras Jukna** (Vilniaus Gedimino technikos universitetas, fizika – N 002);

**doc. dr. Edvardas Kazakevičius** (Vilniaus universitetas, gamtos mokslai, fizika – N 002);

**dr. Ignas Nevinskas** (Fizinių ir technologijos mokslų centras, gamtos mokslai, fizika – N 002);

**dr. Evaldas Stankevičius** (Fizinių ir technologijos mokslų centras, gamtos mokslai, fizika – N 002).

Disertacija ginama viešame Gynimo tarybos posėdyje 2020 m. gruodžio mėn. 10 d. 14 val. Fizinių ir technologijos mokslų centro A101 auditorijoje. Adresas: Saulėtekio av. 3, Vilnius, tel. +37052648884; el. paštas: office@ftmc.lt.

Disertaciją galima peržiūrėti Fizinių ir technologijos mokslų centro bei VU bibliotekose ir VU interneto svetainėje adresu:

<https://www.vu.lt/naujienos/ivykiu-kalendorius>.

**Atviroji prieiga** Šis darbas platinamas pagal licenzijos

„Creative Commons Priskyrimas 4.0 Tarptautinė (CC BY 4.0)“

(<http://creativecommons.org/licenses/by/4.0/>) sąlygas, jei nenurodyta kitaip.

Abbreviation	Meaning
2D	two dimensional
3D	three dimensional
ADC	analog-to-digital converter
BEP	beam equivalent pressure
CW	continuous wave
DMD	digital micro-mirror device
DOF	depth of field
ESD	electrostatic discharge
FDTD	finite-difference time-domain method
FDTS	frequency-domain terahertz spectroscopy
FKO	Franz–Keldysh oscillations
HDPE	high-density polyethylene
HRXRD	high-resolution X-ray diffraction
LDW	industrial-scale laser-direct-write
LNA	low-noise amplifier
MBE	molecular beam epitaxy
NEP	noise equivalent power
OAP	off-axis parabolic (mirror)
PLL	phase-locked loop
PP	polypropylene
PR	photoreflectance
PTFE	polytetrafluoroethylene (Teflon)
RHEED	reflection high-energy electron diffraction
SNR	signal-to-noise ratio
Si	silicon
TDS	time domain spectroscopy
THz	terahertz, $10^{12}$ Hz
THz spectroscopy	Spectroscopy in terahertz region
Ti-mB	titanium microbolometer
UHMWPE	ultra high molecular weight polyethylene
px	pixel

# 1. ACKNOWLEDGEMENTS

I am most grateful to my supervisor *Gintaras Valušis* for unending support, creative writing and wild ideas.

*Linas Minkevičius* helped me immensely in preparation for experiments, simulation, execution of the experiments and finally analysis of the experimental data. Furthermore, I would like to thank:

*Rimvydas Venckevičius* for developing THz image acquisition system.

*Dalius Seliuta* and *Andrzej Urbanowicz* for providing spectra of different materials for homodyne experiment.

*Simonas Indrišiūnas* for fabricating Fibonacci zone plate.

*Sergej Orlov* for deep insights into optics in Bessel experiment.

*Mindaugas Karaliūnas* for help executing the Fibonacci experiment.

*Agnieszka Siemion* for providing novel ideas on spatial filtering.

*Liang Qi* for being effective experimenter in spatial filtering experiment.

*Irmantas Kašalynas* for keeping order in our laboratory.

*Vytautas Jakštas* for support and insightful discussions.

*Rusnė Ivaškevičiūtė-Povilauskienė* for always being catful.

*Ignas Grigelionis* and *Vytautas Janonis* for insightful discussions.

*Vladislovas Čižas* for beautiful figures for Bessel paper.

*Justinas Jorudas* for being the master of the tables.

*Mažena Mackoit-Sinkevičienė* and *Renata Butkutė* for cheerfulness.

*Ignas Nevinskas* and *Evaldas Stankevičius* for reading the thesis and useful feedback.

FTMC LDEL team for introducing me to the metrology field.

Finally, I would like to thank my mother *Zita*, father *Jonas*, brother *Robertas*, sister-in-law *Dalia*, grandmother *Joana* and my greatest wife *Jurga* for constant support during my life and this undertaking.

Sorry for others who were out of the scope of this thesis.

# TABLE OF CONTENTS

<b>1</b>	<b>ACKNOWLEDGEMENTS</b>	<b>6</b>
<b>2</b>	<b>INTRODUCTION</b>	<b>9</b>
2.1	Major Goal . . . . .	11
2.2	Tasks of this Work . . . . .	11
2.3	Scientific Novelty . . . . .	12
2.4	Statements for Defence . . . . .	14
2.5	Author Contribution . . . . .	15
<b>3</b>	<b>OVERVIEW OF TERAHERTZ IMAGING TECHNIQUES</b>	<b>16</b>
3.1	Introduction . . . . .	16
3.2	Terahertz imaging schemes . . . . .	16
3.3	Terahertz beam engineering . . . . .	20
3.4	Terahertz detection at room temperature . . . . .	22
<b>4</b>	<b>INVESTIGATION METHODS</b>	<b>24</b>
<b>5</b>	<b>HOMODYNE IMAGING</b>	<b>27</b>
<b>6</b>	<b>INGaAs DIODES FOR TERAHERTZ SENSING</b>	<b>32</b>
<b>7</b>	<b>FIBONACCI (BIFOCAL) IMAGING</b>	<b>41</b>
<b>8</b>	<b>BESSEL ZONE PLATES FOR THICK OBJECT IMAGING</b>	<b>50</b>
<b>9</b>	<b>IMAGING WITH SPATIAL FILTERING METHODS</b>	<b>56</b>
<b>10</b>	<b>MAIN RESULTS AND CONCLUSIONS</b>	<b>61</b>
<b>11</b>	<b>PUBLICATIONS AND CONFERENCES</b>	<b>64</b>

<b>12</b>	<b>CURRICULUM VITAE</b>	<b>68</b>
12.1	About the author . . . . .	68
12.2	Apie autorių . . . . .	68
<b>13</b>	<b>SANTRAUKA</b>	<b>69</b>
13.1	Įvadas . . . . .	69
13.2	Darbo tikslas . . . . .	70
13.3	Darbo uždaviniai . . . . .	71
13.4	Darbo naujumas . . . . .	71
13.5	Ginamieji teiginiai . . . . .	73
13.6	Autoriaus indėlis . . . . .	74
13.7	Rezultatų apžvalga . . . . .	74
13.8	Diskusija ir išvados . . . . .	76
13.9	Padėka šeimai . . . . .	77
	<b>REFERENCES</b>	<b>78</b>
<b>14</b>	<b>REPRINTED PUBLICATIONS</b>	<b>91</b>
	Terahertz homodyne spectroscopic imaging of concealed low- absorbing objects . . . . .	92
	InGaAs Diodes for Terahertz Sensing—Effect of Molecular Beam Epitaxy Growth Conditions . . . . .	97
	Fibonacci terahertz imaging by silicon diffractive optics . . . . .	111
	Bessel terahertz imaging with enhanced contrast realized by silicon multi-phase diffractive optics . . . . .	116
	Titanium-Based Microbolometers: Control of Spatial Profile of Terahertz Emission in Weak Power Sources . . . . .	127



## 2. INTRODUCTION

If one consider observation using invisible parts of the light's spectrum, as a rule, the first association that usually arises is photos taken in X-ray light because of medical tests or security inspection. It is indeed strong and useful tool allowing to see "inside" the different objects allowing thus to discriminate them or to identify affected tissues in a human body. Despite of many advantages of this approach, X-rays are not so friendly for human body or other living beings because of the ionizing nature of the radiation [1,2]. As concerns other applications, for instance, detection of low density materials (like clothing, plastics, carton etc.) novel access routes are required. One of possible ways to proceed could be employment of terahertz (THz) radiation (sometimes also called T-rays), which can penetrate through non-conducting materials without undesirable hazard to living organisms.

It is generally agreed that THz frequencies span the range from 100 GHz up to 10 THz. It is a particular place in the electromagnetic spectrum – between microwaves and the infrared one – defining the requirement to merge together rather different concepts – classical carrier transport and quantum mechanics-based – in the development of devices (see Fig. 2.1). On the other hand, from the point of view of applications, the THz range has opened a large variety of potential applications in many fields – in addition to aforementioned security [3–5], and medical [6–8] purposes, one can non-invasively enumerate materials [9–11] and implement industrial diagnostics [12], broad bandwidth communication systems [13,14] and radars [15,16], detection of chemical compounds [17] and biological agents [18], use THz radiation to discriminate different packaged substances [19,20] and apply to quality control [21].

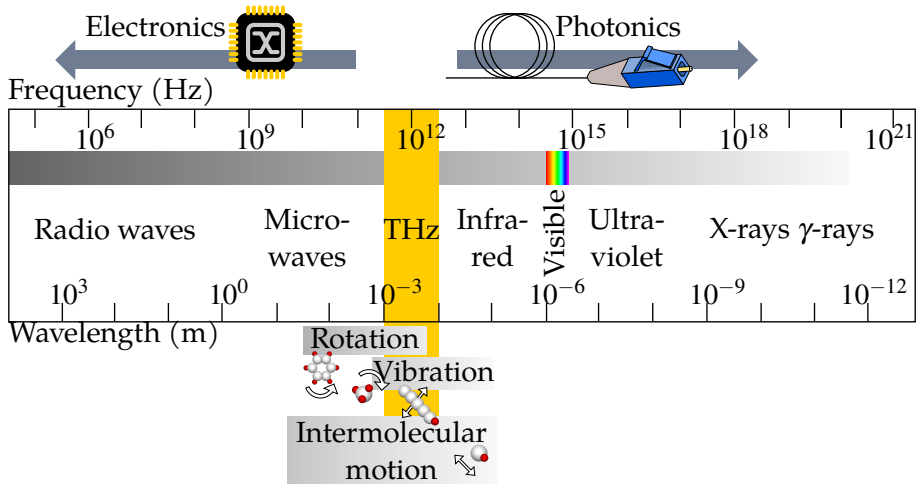


Figure 2.1: THz range lies in frequencies between 100 GHz and 10 THz of electromagnetic spectra.

A particular role in development of THz technology can be attributed to the THz imaging as it can serve as very powerful tool in security and medicine. Since breakthrough work by B. B. Hu and M. Nuss [22] the THz imaging gained tremendous advancements [9, 23, 24] both in development of the technique itself and its active and passive components as well as prospects in a large variety of applications.

It is worth noting two different aspects of applied research in THz imaging. The first one concerns development and demonstration of innovations and applications in scientific laboratory; the second one deals with direct implementation in real conditions of operation. If in the first case alignment, size of optics and even operational temperature is not critical, in the second one situation drastically changes – real operational conditions do not tolerate inconvenience in usage of the systems, they must operate in room temperature, system size needs to be reduced as much as possible, optical alignment issues must be minimized. Therefore, reduction of their dimensions and preference to on-chip solutions in emission/beam shaping or detection/optical coupling remains one of the prime interests for direct implementation aims. That is why solid-state-based solutions and diffractive optics ideas in miniaturization of THz imaging systems arise as one of the most important tasks in over-

coming issues in real implementation [25,26]

The given work is exactly dedicated to this purpose. In what follows we concentrated our efforts to the development of compact THz imaging aiming to make them more closer to real operational implementation applying principles of optical beam engineering. Initially, we manipulate with THz radiation in homodyne detection scheme via phase management seeking to find effective, cost-effective and simultaneously simple solutions for reliable homodyne THz imaging; secondly, by using THz beam engineering tools via employment of diffractive optical components based on high-resistivity silicon, we intend to evidence that it can be well suited approach in reducing size of THz imaging and still keeping strongly expressed abilities to reveal and discriminate weakly THz radiation absorbing objects placed in boxes of conventional postal packages size.

## **2.1 Major Goal**

The major goal of the thesis is development and characterization of compact spectroscopic terahertz imaging system using principles of optical beam engineering.

The goal is twofold.

Firstly, to develop and characterise reliable compact THz homodyne imaging scheme seeking to find efficiency and cost-effectiveness containing solutions.

Secondly, applying THz beam engineering tools via employment of silicon diffraction optics components to develop and characterise compact THz imaging system enabling to reveal and discriminate weakly THz radiation absorbing packaged objects.

The goal can be decomposed into the following tasks.

## **2.2 Tasks of this Work**

1. To develop efficient and cost-effective compact homodyne THz imaging using reliable bow-tie diodes and compare it with alternative heterodyne THz imaging technique to identify low absorbing objects.

2. To examine and characterize its operation at 0.3 THz and 0.6 THz frequencies, estimate signal-to-noise ratios and dynamic range; consider efficient and cost-effective solutions for phase shifting.
3. To investigate effect of molecular beam epitaxy growth conditions on InGaAs/InP layers dedicated for bow-tie diodes fabrication and determine optimal growth regime with respect to InGaAs diodes parameters.
4. To design, fabricate and investigate silicon diffractive optics-based bifocal THz lens.
5. To implement the designed silicon based bifocal THz lens into THz imaging, demonstrate simultaneous multi-focal THz imaging, to characterise and estimate main parameters of the developed compact THz imaging set-up.
6. To develop diffractive THz lens allowing Bessel THz imaging with extended focal depth up to 20 mm suitable for imaging of objects hidden in post packages.
7. To demonstrate purely silicon optics based Bessel THz imaging; estimate signal-to-noise ratios and dynamic range; consider effective and cost-effective solutions for enhancement of the contrast and compare it with conventional THz imaging.
8. To manipulate THz beam using spatial filtering methods and apply it for THz imaging technique; reveal its advantages in comparison with other beam engineering methods; define requirements for detector parameters needed for such kind of THz imaging.

## 2.3 Scientific Novelty

Scientific novelty of the thesis relies on the following key-findings:

1. THz homodyne and direct imaging using InGaAs bow-tie diodes as sensors was demonstrated to discriminate low-absorbing materials packaged between up to six layers of cotton fabric at 0.3 THz and 0.6 THz. Operation features and imaging parameters between direct and homodyne scheme were discussed and compared.

2. The homodyne phase-shifting scheme was realized here in a simple way by varying the number of office paper sheets in the optical path. It is shown that homodyne THz imaging can serve as a convenient imaging tool to screen low-contrast suspicious inclusions in textiles.
3. Different technological conditions for the InGaAs devices fabricated from InGaAs layers grown by molecular beam epitaxy (MBE) on semi-insulating InP substrate are considered. It was shown that structures exhibit presence of strong built-in electric fields reaching up to 49 kV/cm, which were derived from the photoreflectance spectra.
4. It was demonstrated that the spectral density of voltage fluctuations in InGaAs bow-tie diodes at room temperature is found to be proportional to  $1/f$ , while at lower temperatures, 77–200 K, Lorentzian-type spectra dominate due to random telegraph signals caused by individual capture defects.
5. The obtained results revealed effect of InGaAs layers grown at different beam equivalent pressure (BEP) In/Ga ratios on the low-frequency noise level and the sensitivity of the THz detectors. It was determined that THz detectors grown with BEP In/Ga ratio equal to 2.06 is the most suitable choice to fabricate sensitive InGaAs bow-tie diodes for room temperature operation.
6. It was shown that compact Fibonacci (bifocal) terahertz imaging can be realized using monochromatic THz light sources using diffractive silicon lenses. The focusing performance was studied both theoretically and experimentally by measuring spatial profiles, the distance between the foci and focal depth at 0.3 THz and 0.6 THz frequencies.
7. Simultaneous imaging with the wavelength resolution of two planes separated by a 7 mm distance was experimentally demonstrated at 0.3 THz and 0.6 THz frequencies. The multifocal imaging results were compared with the performance of the phase zone plate designed of the same diameter and material.

8. Thin and compact Bessel zone plates based on silicon multi-phase diffractive optics were designed, produced and demonstrated in the THz transmission imaging system.
9. A novel experimental setup using two Bessel zone plates for enhanced imaging purposes and increased compactness was suggested. The discrete axicons containing 4 phase quantization levels were fabricated from a high-resistivity silicon by employing laser ablation technology allowed to extend the focal depth up to 20 mm with minimal optical losses and refuse employment of bulky parabolic mirrors in the imaging set up.
10. Compact THz imaging system reveals possibility to inspect objects of more than 10 mm thickness with enhanced contrast, weak dependence on the sample thickness and position due to long focal depth as well as increase its resolution up to high level by applying the deconvolution algorithms.
11. Spatial filtering methods – phase contrast and dark field – can be applied in large aperture THz imaging to resolve weakly absorbing objects in subTHz range using sensitive room temperature detectors, for instance, titanium-based microbolometers. The images of weakly absorbing objects were recorded in unfocused light at 0.3 THz using circle shaped paper sheets as filter in phase contrast and circle shaped aluminum foil in dark field experiments.

## **2.4 Statements for Defence**

1. Homodyne terahertz imaging can be employed to discriminate low absorbing objects at 0.3 THz and 0.6 THz frequencies using room-temperature InGaAs bow-tie diodes as reliable detectors and phase control – using different numbers of paper sheets.
2. InGaAs layers grown by molecular epitaxy with beam equivalent pressure In/Ga ratio equal to 2.06 is found to be the most suitable for fabrication of room temperature bow-tie THz detectors exhibiting sensitivity in the range of 10 V/W and noise equivalent power

below  $1 \text{ nW}/\sqrt{\text{Hz}}$  at 0.6 THz due to strong built-in electric field effects.

3. Compact bifocal terahertz imaging can be realized using monochromatic THz light source and phase silicon zone plates based on the Fibonacci sequence.
4. Bessel THz imaging can be implemented in compact THz imaging scheme using only high-resistivity silicon-based optical lenses and enabling thus THz imaging of thick objects in 1 cm focus depth scale at subTHz frequencies.
5. Spatial filtering methods – phase contrast and dark field – can be applied in large aperture THz imaging to resolve weakly absorbing objects in subTHz range.

## 2.5 Author Contribution

Author was involved in execution of homodyne [P1], Fibonacci bifocal [P3], Bessel zone plate [P4] and spatial filtering methods [P5] experiments starting from the designs of the setup, design preparation and validation of diffractive elements for optical beam engineering, design and fabrication of imaging samples to illustrate advantages of the novel approaches, recording of THz images and further processing as well as analyses of the obtained data.

Author was engaged in THz part of investigation (electrical characterization of the samples and estimates of bow-tie diodes sensitivity) and data analysis for publication [P2] of InGaAs bow-tie diode detectors subsequently applied for THz detection in homodyne imaging experiments.

He also improved and developed additional software utilities for data acquisition and processing. The author was involved in the preparation of scientific papers and material for the conferences.

# 3. OVERVIEW OF TERAHERTZ IMAGING TECHNIQUES

## 3.1 Introduction

Recording of THz images requires special experimental set-up consisting, as a rule, of THz emitter, passive optical components like mirrors, beam splitters or focusing elements and sensitive detectors. One can note that principles of operation of the recording systems are usually defined by features of THz radiation source.

If it is based on ultrafast laser (pulsed coherent source), optoelectronic principles of THz generation and detection are employed. In case of electronic sources, for instance, electronic multipliers, mostly operating in sub-THz frequency range, new principles of detection (bolometers, field-effect transistors or high-frequency diodes) need to be used. Generally, THz imaging techniques depending on the physical principles employed can be depicted schematically as it is given in Fig. 3.1.

Below we present short overview of THz imaging recording techniques and possible imaging with special emphasis on possible compact solutions in passive optical components.

## 3.2 Terahertz imaging schemes

The pioneering THz images recorded by B. B. Hu and M. Nuss [22] were based on usage of femtosecond laser in time domain spectrometer (TDS) system, when ultrashort laser pulse optically excites carriers in semiconductor with short carrier lifetimes, excited carrier accelerated by the electric field emits broadband coherent THz emission which is



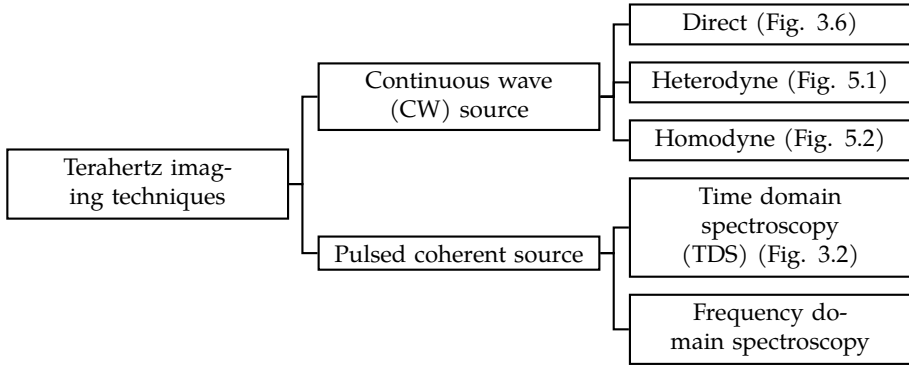


Figure 3.1: Terahertz imaging techniques. All schemes presented here display inherent feature of bulky optical elements to manipulate the laser radiation.

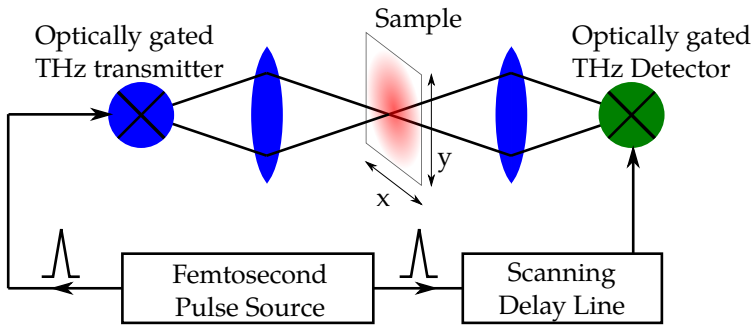


Figure 3.2: Scheme of TDS THz imaging setup for measurement in transmission geometry. Adapted from [22].

detected via optoelectronic antenna gated with a delayed optical pulse as it is shown in Fig. 3.2. As one can see, THz beam that was focused onto the sample.

This way the THz radiation transmitted through the specific point of the sample produces a pixel (px). To record every pixel the sample is translated in  $x$  and  $y$  axes to produce final two dimensional (2D) THz transmission image akin to X-ray image. This imaging process is called raster scanning and it enables best possible signal-to-noise ratio (SNR) due to the coherent scheme of the detection. Efficient imaging is of particular importance in THz range due to the low power of accessible sources. However, due to the need of mechanical movement of the sample, raster scanning is time-consuming as it is constrained by the detector integration time  $\tau$ , as an example at  $\tau = 10$  ms an image of  $100 \times 100$  px dimension takes 100 seconds to capture and  $400 \times 400$  px

image takes more than 26 minutes. As can be understood, such long THz image capture duration is not an advantage in implementing such systems into direct applications. One can note that the replacement of femtosecond laser by continuous wave (CW) sources such as electronic multiplier chains or Gunn diodes [27] and by relevant detectors do not change the situation from point of view of image recording duration.

To introduce an actual terahertz imaging system, as an example, we present novel terahertz imaging setup developed during completion of this work. Its photo is given in Fig. 3.3(a). The set-up dedicated to operation in transmission geometry utilizing two Bessel zone plates (BZP) for thick sample imaging. This system uses terahertz source, off-axis parabolic mirror (OAP) for collimating THz beam, Bessel zone plate (BZP) for focusing THz radiation, then collimating it with another BZP. Finally, OAP focuses the radiation onto the detector. Features of the imaging system and Bessel zone plates will be discussed further in Chapter 8.

For acquaintance with THz image, a typical terahertz image of objects shown in Fig. 3.3(b) is depicted in Fig. 3.3(c). The images are captured by direct raster scanning at 0.6 THz. As is easily seen, a sample consisting of hypodermic needle, steel blade and a piece of nitrile glove enveloped between 6 layers of cotton fabric can be decomposed demonstrating thus ability of THz radiation to inspect and resolve hidden objects. Metal and plastic are clearly visible and furthermore, even separate layers at the lines where the nitrile glove fingertip was cut off can be distinguished.

A linear THz detectors array [28, 29] can be a solution of the issue in reducing the image capture duration by the factor of pixel quantity in the array. This solution requires specific optical beam engineering means – either beam expansion or application of line forming cylindrical lens [30] which in turn distributes available THz source power between detectors in the array. To alleviate the loss of power multiple THz sources can be used, however, it can strongly increase cost of the imaging system due to high prices of available sources.

Similarly, multiple lines of line detector arrays could be combined into a 2D detector matrix [31–33] allowing for imaging of the whole area simultaneously via complementary metal–oxide–semiconductor

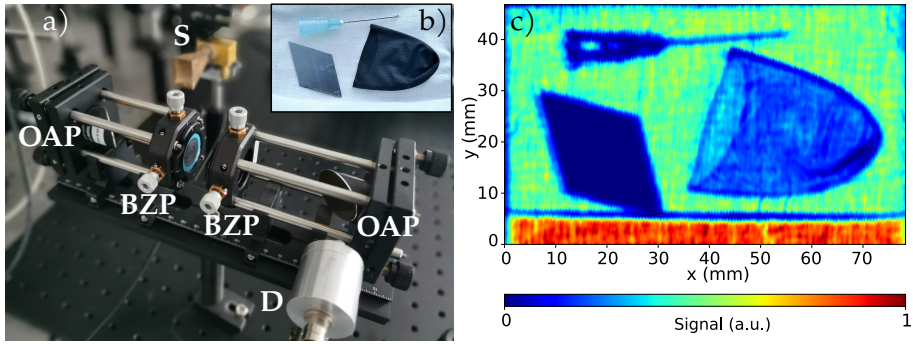


Figure 3.3: a) Novel terahertz imaging setup for operation in transmission geometry utilizing two Bessel zone plates for thick sample imaging. Components of the setup: S - THz source, OAP - off-axis parabolic mirror, BZP - Bessel zone plate, D - detector. b) Photo of an imaging sample containing hypodermic needle, steel blade and a piece of nitrile glove enveloped between 6 layers of cotton fabric. c) A transmission image of the sample at 0.6 THz.

(CMOS) or charge-coupled device (CCD) detector arrays if the THz radiation can be converted electro-optically into visible range. Due to absence of the mechanical movement during the capture 2D THz detector matrix is capable of record images at up to 450 frames per second [34] that would allow monitoring biological sample dynamics, rapid industrial processes, etc. However, as due to diffraction limit the pixel pitch of the 2D THz detector arrays is in the order of  $100 \mu\text{m}$  [35] the THz illumination intensity spread to cover the whole matrix would effectively decrease the amount of THz radiation power at a single pixel in a 2D THz array by at least two orders of magnitude compared to single pixel raster scan. This amount of decrease in THz power can be critical for imaging samples with features are at the edge of detection limit such as low absorbing objects or extremely high absorbing objects, i.e. in cases when single pixel raster scan is well-suited. It is worth noting interesting technique used for THz imaging is a single pixel camera [36–38] that allows capture of an image comprising of multiple pixels without mechanical movement of the optical system and utilizing a single pixel THz detector. Single pixel camera designs are mostly based on digital micro-mirror device (DMD) that selectively reflects THz radiation and illuminates the sample in a predefined pattern that in turn is correlated to the measured THz radiation intensity at the single pixel detector, and hence a whole image can be reconstructed.

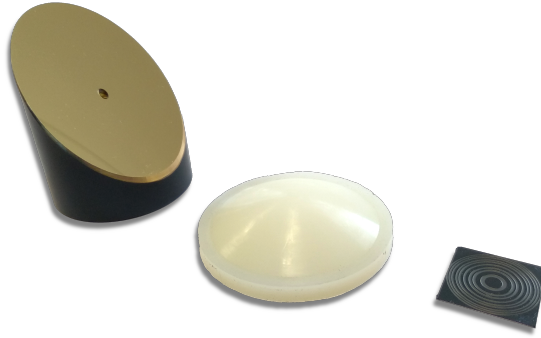


Figure 3.4: A comparison photo of focusing elements for terahertz radiation. From the left: reflective off-axis parabolic mirror with gold coating (Thorlabs MPD269H-M01), a refractive plano-convex spherical lenses made of polytetrafluoroethylene (PTFE, Teflon, custom milled), diffractive silicon based bifocal Fibonacci lens.

By a rapid switching between the illumination patterns one can achieve real-time THz imaging [39]. Since only single pixel detector is required, the illumination of the specific area of the sample is inversely proportional to the size of the imaged area and thusly overall performance is similar to the imaging scheme utilizing 2D detector matrix.

### 3.3 Terahertz beam engineering

High quality of focusing of the radiation or beam engineering aiming to manage spatial mode profile is very important in optical systems because it directly impacts the overall performance of the whole imaging system. Effective focusing performance is essential in THz range due to quite low power of the available THz sources ( $\mu\text{W}$  range [40]). This requirement brings the need of specialized solutions that achieves best performance for a given type of materials under test.

Off-axis parabolic (OAP) mirrors reflect the incident light from a metallic parabolic surface and focus collimated light into a focal point without introducing noticeable spherical aberrations. While reflective OAP mirrors introduce miniscule loss of THz beam intensity the use of OAP mirrors is hindered by sizeable dimensions, introduction of astigmatism [41] and inability to use them in line due to inherent change in direction of the beam.

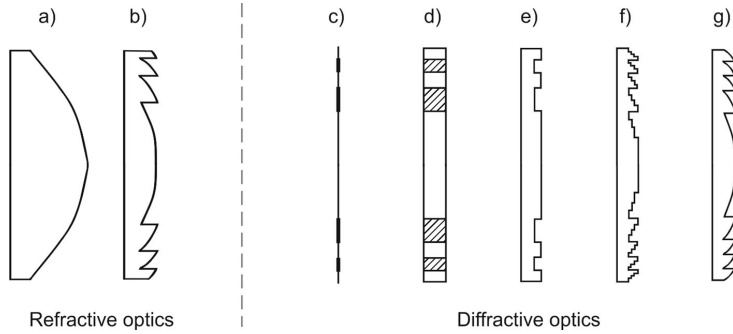


Figure 3.5: Refractive (a, b) and diffractive (c–g) lenses. a) Bulk lens. b) Fresnel lens (not used in the THz range of radiation). c) Fresnel zone plate—amplitude binary. d) Planar dielectric zone plate—structure created from two materials with different refractive indices that corresponds to phase binary grating. e) Binary phase—phase-reversing zone plate. f) Multi-level zone plate. g) Kinoform (Fresnel diffractive lens). Reprinted under Creative Commons Attribution 4.0 (CC BY 4.0) license from reference [48].

Conventional or refractive lenses can be manufactured of a variety of polymers utilizing high transmittance and high refractive index in THz range: high-density polyethylene (HDPE), polytetrafluoroethylene (PTFE, Teflon), polypropylene (PP) [42, 43], ultra high molecular weight polyethylene (UHMWPE) [44]. Even parafin-wax [45] can be used to fabricate lenses, but it relatively soft and lacks temperature stability. Spherical lenses for THz range can be produced using various methods including machining, 3D printing [46], forming powders in a press, etc. 3D printing of plastic lenses is especially interesting allowing for rapidly produced cost efficient prototypes to test novel designs as 3D printed surfaces provide satisfactory surface roughness [47] for THz range due to significantly longer wavelengths than the visible range. However, regular refractive THz lenses introduce significant loss of intensity due to the thickness of the lens material. Comparison of sizes and designs of possible THz passive optical elements is given in Fig. 3.4.

Industrial THz imaging applications require cost-effectiveness, compactness and alignment-free optical systems. One of possible routes to proceed is so called terahertz zone plates (TZP) [49], or also called Fresnel zone plates (not to be confused with Fresnel lenses as used in lighthouses).

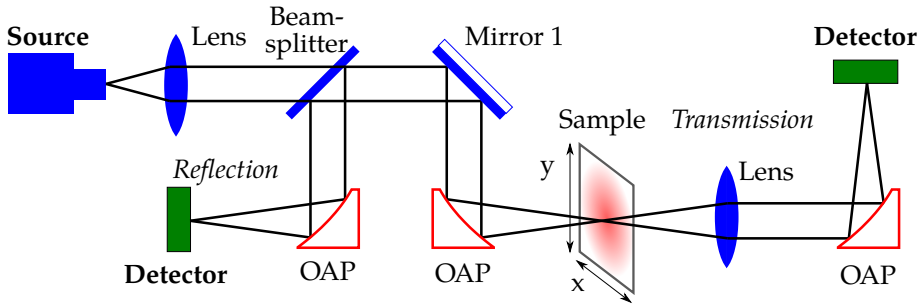


Figure 3.6: Scheme of raster THz imaging setup for measurement in both transmission and reflection geometries, where Lens – HDPE or TPX lens, Beam-splitter – high-resistivity Si wafer, Mirror – gold plated flat mirror, OAP – off axis parabolic mirror.

TZPs are diffractive focusing elements composed of alternating concentric rings that manipulates pass or block THz radiation (Fig. 3.4). Diffraction is defined as any deviation of a light ray from rectilinear propagation, which is not caused by reflection nor refraction. TZPs are planar elements, relatively simple to fabricate using one step lithography or laser ablation on widely available silicon (Si) wafers. Resulting TZPs are less than 1 mm thick [50] with the diameter of TZP depending only on the THz beam diameter to be focussed. TZPs display a quite serious disadvantage of their high chromatic aberration [51], however, it can be overcome by using narrow bandwidth THz sources. In general, TZPs as planar elements allow convenient, straightforward and reliable integration in optical systems to enable alignment-free and maintenance-free operation. One can note that even paper diffractive lenses [52] can be fabricated relatively easily, but they are not efficient enough for direct practical applications.

### 3.4 Terahertz detection at room temperature

Terahertz detection and imaging scheme is depicted schematically in Fig. 3.6. As one can see, it is composed of THz radiation source, passive optical elements like beam splitters, mirrors, lenses, xy stage and THz detectors. The THz detectors are transducers that convert an incoming THz radiation into some convenient form like voltage or current which subsequently can be recorded, processed and analyzed. Superconduct-

ing bolometers offer a distinct advantage in comparison to uncooled bolometers because of their low thermal noise [53] and can successfully be applied in astrophysics aims. However, in everyday practical applications uncooled detectors would be preferable to achieve much lower system complexity and avoid the usage of a cryocooler equipment.

Development of faster and more sensitive detectors at room temperature have yielded different approaches to sensing THz radiation, notably Schottky diodes [54], nanometric transistors [55–60], uncooled bolometers [8, 61], and bow-tie diodes concept of which was previously been developed using various materials, i.e. asymmetrically necked planar n-n<sup>+</sup> GaAs structure [62], asymmetrically-shaped 2DEG GaAs/AlGaAs layers [63], and specifically, InGaAs diodes [64–67]. InGaAs-based bow-tie diodes for the THz range are found to be well suited for development of compact THz imaging systems including spectroscopic THz imaging [68, 69].

It is original concept of sensors developed in our laboratory, and, mainly because of this reason and its reliability, we have chosen it for implementation in homodyne scheme. In more details, to further optimize design for sensitive and broadband THz detection, one needs to understand the noise origin, influence of growth conditions and role of materials defects for device operation.

## 4. INVESTIGATION METHODS

Fibonacci bifocal THz focusing element was fabricated using laser ablation technology based on an industrial-scale laser-direct-write (LDW) system [50] based on a 1064 nm wavelength, a 13 ps pulse, 1 MHz repetition rate, and a 60  $\mu$ J peak energy Atlantic 60 laser (Ekspla, Ltd., Vilnius, Lithuania) in Laser Microfabrication Laboratory, Department of Laser Technologies, FTMC. A sample with an outside diameter of 24 mm and two foci separated by a defined distance of 7 mm was fabricated on monocrystalline silicon orientation (110), with resistance 0.01–1M $\Omega$ cm and refractive index 3.46 for [P3].

Fabrication of silicon wafer was carried out in Coherent Optics Laboratory, Department of Fundamental Research, FTMC. The laser ablation set up was composed of Pharos-SP laser (Light Conversion Ltd, Vilnius, Lithuania) (wavelength 1028 nm, pulse duration = 350 fs, energy = 50  $\mu$ J, repetition rate = 100 kHz), IntelliSCAN-14 scanner (SCANLAB, GmbH, Munich, Germany) and F-Theta f100 lens (Sill Optics, GmbH & Co. KG, Wendelstein, Germany) with scanning speed = 1000 mm/s. The center hole in the optical element was used to ease the optical alignment. This laser ablated device was investigated in [P4].

Optical 2D images were obtained using KH-7700 digital microscope (Hirox Co Ltd., Tokyo, Japan) which also allowed to get 3D measurements and surface visualization using image stacking technique.

THz imaging was carried out using electronic multiplier sources (Virginia Diodes, Inc., Charlottesville, Virginia, United States of America) generating radiation of 0.15 THz, 0.3 THz and 0.6 THz frequencies in continuous wave mode with power of 29 mW, 13.2 mW and 0.56 mW, respectively. Initial frequency for the multipliers was generated using microwave analog signal generator E8257D (Agilent Technologies, Inc.,



Santa Clara, California, United States of America) operating at 12.5 GHz frequency and 10 dBm power.

3D printed parts were utilized as sample holders and for the samples themselves using additive manufacturing type printer Ultimaker 2 (Ultimaker B.V., Utrecht, Netherlands) with polylactic acid (PLA) filament which allowed for convenient printing and sufficient rigidity of the resulting parts.

xyz stage was used for automated movement of THz imaging samples, diffractive lens or detector assemblies. The stage allowed movement in the volume of  $15 \times 15 \times 15 \text{ cm}^3$  was comprised of PRO115 (Aerotech, Inc., Pittsburgh, Pennsylvania, United States of America), NST150M and LTS150M linear stages (Thorlabs, Inc., Newton, New Jersey, United States of America) which were controlled by custom data acquisition software.

Low-absorbing samples and cotton layers were characterized individually in the THz range via transmission measurements using commercial frequency-domain terahertz spectrometer (FDTS) Topptica TeraScan 780 (TOPTICA Photonics AG, Graefelfing (Munich), Germany).

The absolute power measurements were made using calibrated THz Absolute Power & Energy Meter System (Thomas Keating Ltd., West Sussex, England) based on the photoacoustic effect.

THz detection was realized using titanium resonant THz antenna-coupled microbolometers (Ti-mB) [70] operating at room temperature. Detector modules used for experiments were comprised of 4 Ti-MB pixels with pitch of 2.5 mm and pixel dimensions of  $2.5 \times 2.5 \text{ mm}^2$  combined with a preamplifier which were used one pixel at a time. Detectors were produced by Luvitera, Ltd. (Vilnius, Lithuania) a joint Terahertz Photonics Laboratory, Optoelectronics Department, FTMC (Vilnius, Lithuania) and the Laboratory for Microelectronics, Faculty of Electrical Engineering, University of Ljubljana (Ljubljana, Slovenia) company. Ti-mBs were used to record data in papers [P3], [P4] and [P5].

Three dimensional (3D) finite-difference time-domain (FDTD) method was used for modeling of the electric field distribution in space [71]. The spatial resolution was set up from 0.01 to 0.115 mm.

To simplify the simulation, symmetry conditions of the structures were applied, and the absorbing boundary conditions were set in all the directions. The normalized electric field was recorded in the whole simulation volume. A source of a multifrequency plane wave, transparent to the reflected wave, was specified in the front of the zone plate plane. Different zone plate designs can be programmatically generated to optimize THz beam engineering elements for required applications. The resulting electric field distribution in space can be used to predict the focusing performance before fabricating the zone plates. 3D FDTD method was applied in papers [P3] and [P4].

## 5. HOMODYNE IMAGING

As was already aforesaid, THz frequency radiation is widely applied for imaging samples through low-absorbing non-conducting materials, such as clothing fabrics or packaging supplies. Thus, THz imaging serves as a valuable tool to expose contents of packaged and concealed objects in various environments. However, when the concealed objects themselves exhibit low-absorption in THz frequencies, direct THz imaging approach becomes not rational due to a small signal-to-noise ratio which means low contrast prohibiting object recognition. To overcome the problem one can use coherent detection techniques like heterodyne THz imaging [66,72] which due to reduction of noise floor allows to strongly increase the dynamic range and, as a consequence, to identify low absorbing materials. Nevertheless, the heterodyne approach is not so convenient for implementation purposes as it requires at least two THz sources synchronized via a phase-locked loop (PLL) as it is shown in Fig. 5.1.

Hence, new solutions are needed aiming to make THz imaging systems more competitive in practical implementations. Our suggestion to overcome the need of two THz sources direct transmission imaging set-up was employing homodyne technique (Fig. 5.2) by splitting THz beam into two arms which then interfered in the reliable bow-tie detector [68]. To find a very simple way to manage the phase of illumination, a stack of office paper sheets was placed into one of the optical paths to change the optical length, hence, eliminating the need of moving any of the optical elements like delay lines. Despite of certain absorption by the paper sheets, the increase in contrast is still good enough to provide good image quality and avoid usage of relatively expensive optical delay line. Moreover, spectroscopic approach – for instance, two colour

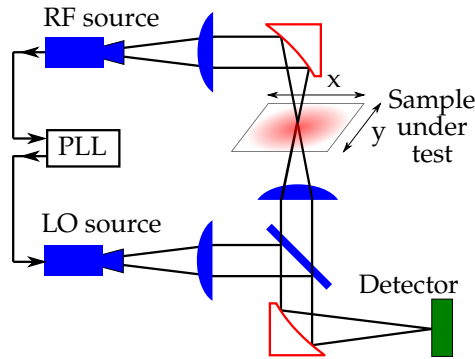


Figure 5.1: Scheme of heterodyne THz imaging setup for measurement in transmission geometry. Radio frequency (RF) and local oscillator (LO) sources linked by phase-locked loop (PLL) are combined to achieve heterodyning. Adapted from [66].

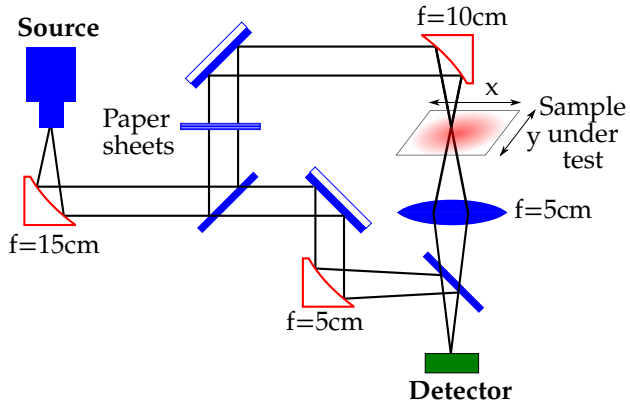


Figure 5.2: Scheme of homodyne THz imaging setup for measurement in transmission geometry where paper sheets are used to provide phase shift in one of the optical arms. Adapted from [P1].

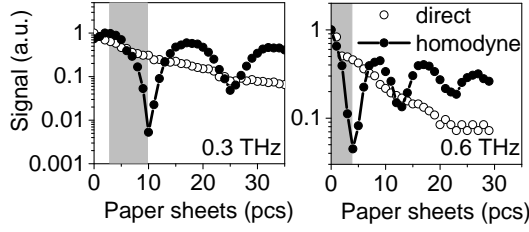


Figure 5.3: Estimates of the system dynamic range at 0.3 THz (left) and 0.6 THz (right) frequencies. Normalized detected signal recorded in both, direct and homodyne, schemes is shown as a function of paper sheets pieces, which was used to vary the phase of the radiation. Shaded area indicates the regime of optimal homodyne operation. Note the increase of dynamic range in the homodyne mode. Adapted from [P1].

experiments using 0.3 THz and 0.6 THz radiation – is also possible in this scheme extending thus discrimination possibilities of packaged materials.

In the homodyne scheme, the resulting intensity registered  $I$  at the detector is dependent of both intensity of optical path passing through the sample  $I_1$  and intensity of the optical path in a free space  $I_2$  as well as the cosine function of the difference between the phases after these different optical paths  $\phi_1 - \phi_2$ :

$$I = I_1 + I_2 + 2\sqrt{I_1 I_2} \cos[\phi_1 - \phi_2] \quad (5.1)$$

On the one hand, intensities of both optical paths are important in the resulting intensity  $I$ . On the other hand, if the imaged sample is low absorbing in THz range, it can be seen that the biggest change in the resulting intensity  $I$  will be due to change in the difference between the phases  $\phi_1 - \phi_2$  as  $I_2$ ,  $\phi_2$  will be constant and  $I_1$  will change insignificantly. Thus, for low absorbing objects homodyne imaging scheme produces an image depicting phase  $\phi_1$  change in the sample and resulting THz image in homodyne setup may be described as phase-like image.

As one can see in Eq. 5.1, the intensity of interference is a periodic function with a phase period of  $2\pi$  that results in phase-ambiguity in case when the samples are thicker than illuminating wavelength (0.5 mm for 0.6 THz and 1 mm for 0.3 THz). To overcome the phase-ambiguity restriction and extend the measurement scale for thicker

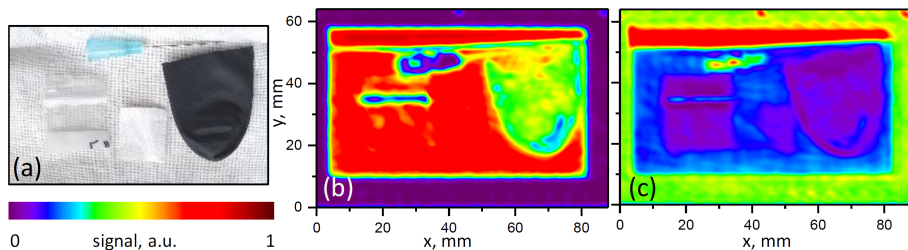


Figure 5.4: Photo of the sample (a) and its direct (b) and homodyne (c) image at 0.3 THz. The sample consisted of a sealable LDPE bag, tissue paper, nitrile glove, and hypodermic needle enveloped in two layers of cotton fabric. SNR is 100 and 200, respectively. THz imaging parameters: XY pixel size  $0.3 \times 0.3 \text{ mm}^2$ , image size  $299 \times 212$  pixels, integration time 10 ms. About 10 paper sheets were used to manage phase in the homodyne imaging. Adapted from [P1].

samples as well as higher frequencies phase-unwrapping method with a noise-suppression data processing algorithm [73] may be applied.

The imaging set-up was calibrated to determine dynamical range of the homodyne system. The experiment was carried out in both direct and homodyne modes at 0.3 THz and 0.6 THz frequency. The homodyne detected signal revealed more than two orders of magnitude higher dynamic range in comparison to the direct one at 0.3 THz range, and a factor of 25 improvement at 0.6 THz. Better contrast can thus be expected in the homodyne mode for recording THz images of low absorbing materials as shown in Fig. 5.3.

To illustrate suitability of the homodyne THz imaging for identifying of thin low-absorbing objects a sample containing sealable low-density polyethylene (LDPE) bag, tissue paper, a piece of nitrile glove, and hypodermic needle enveloped between two layers of cotton fabric was assembled. Imaging results of the sample at 0.3 THz are displayed in Fig. 5.4. THz homodyne imaging allowed to clearly resolve low absorbing thin materials – low-density LDPE bag and a tissue paper – hidden in 2 layers of cotton fabric.

To conclude, homodyne and direct imaging of materials with low-absorption features in the THz range were investigated and compared. The homodyne scheme using paper sheets as the phase tuning component allowed us to increase the detection dynamic range by more than two orders of magnitude. It was demonstrated that the homodyne THz

imaging system at 0.3 THz and 0.6 THz in transmission geometry enables to detect low-absorbing objects – LDPE bag, tissue paper, and nitrile glove – enveloped in up to 6 layers of cotton fabric.

The results on THz homodyne setup and imaging performance were published in [P1].

## 6. INGaAs DIODES FOR TERAHERTZ SENSING

The need for high sensitivity and low noise terahertz detectors is determined by the relatively low power of applicable terahertz sources which output is usually in the milliwatt range depending on the frequency [40]. Consequently, requirements for the sensors, in particular bearing in mind real-time imaging systems become strict and cover wide dynamic range, operation at room temperature, possibility to make detector arrays, preference to planar-technology-based solutions. The detection section in THz imaging setups can be implemented with a wide variety of sensors, namely Si-CMOS detector arrays [59,74], Si MOSFET [72,75–77], GaAs FET [78], etc.

Searching for a durable and technologically simple solution, broadband asymmetrically shaped n-n+ GaAs THz sensor, was presented in 2003 [62]. These type of sensors are resistant to electrostatic discharge (ESD) and do not change their properties, even illuminated by a 1 W electromagnetic radiation power in continuous wave mode. However, their sensitivity at room temperature is relatively low, about 0.3 V/W, thus, these detectors can hardly be used in practical implementation schemes. Later, in 2006, D. Seliuta and co-authors [64] suggested to use a material with a larger electron mobility, i.e. GaAs can be replaced by  $\text{In}_{0.54}\text{Ga}_{0.46}\text{As}$  as the active layer material and coupling the processed structures with a hemispherical silicon lens. Simulation results and detailed electrical characterization of modified/updated bow-tie InGaAs-based terahertz detectors [66] are presented in [67]. The investigation revealed that field-effect-induced conductivity modulation, in addition to carrier heating, can be possible mechanism contributing to the in-



creased sensitivity, reaching up to 10 V/W of the studied detectors [67].

To develop optimal design from point of view of sensitivity, it is of particular importance to understand origin of noise sources in given structures. Noise characteristic investigation is well known as highly sensitive method allowing to reveal physical processes in various structures and devices [79–87]. In addition, the low-frequency noise is a general indicator of quality and enables also reliability prediction [79,80,82,83]. On the other hand, the noise level of detector is restrictive factor of imaging system sensitivity [88].

In this section, comprehensive experimental investigation of the electrical conduction in  $\text{In}_{0.54}\text{Ga}_{0.46}\text{As}/\text{InP}$  structures grown in a various technological conditions is presented. The structures were dedicated to design and fabricate broadband room-temperature operating THz sensors. Properties of the electrical conduction in n-type  $\text{In}_{0.54}\text{Ga}_{0.46}\text{As}$  samples were analyzed and detailed low-frequency noise investigations on temperature were carried out. Obtained results allowed to reveal origin of physical processes in  $\text{In}_{0.54}\text{Ga}_{0.46}\text{As}/\text{InP}$  bow-tie detectors with monolayer of InAs in their interface.

InGaAs layers for the detector fabrication were grown using molecular beam epitaxy (MBE) in Optoelectronic Technology Laboratory in FTMC, Vilnius, Lithuania. The growth of the layers on semi-insulating InP:Fe wafers was monitored using reflection high-energy electron diffraction (RHEED) technique allowing to collect information only from the surface of the sample due to its shallow penetration depth. Different In/Ga beam equivalent pressure (BEP) ratios determining the growth rates at the sample position were chosen to demonstrate BEP In/Ga ratio effect on the noise level and the sensitivity of THz detectors. To optimize the growth conditions, the In/Ga BEP ratio was varied from 2.04 to 2.08.

In Fig. 6.1(a) one can see the overall schematic cross-section of the InGaAs THz detector.

The  $\text{In}_{0.54}\text{Ga}_{0.46}\text{As}/\text{InP}$  bow-tie THz detectors with one monolayer of InAs in the interface between the substrate and InGaAs structure have been investigated. The device was designed as asymmetric bow-tie antenna with one of two semiconductor leaves metalized [65] to enable non-uniform carrier heating. The design and geometrical dimensions

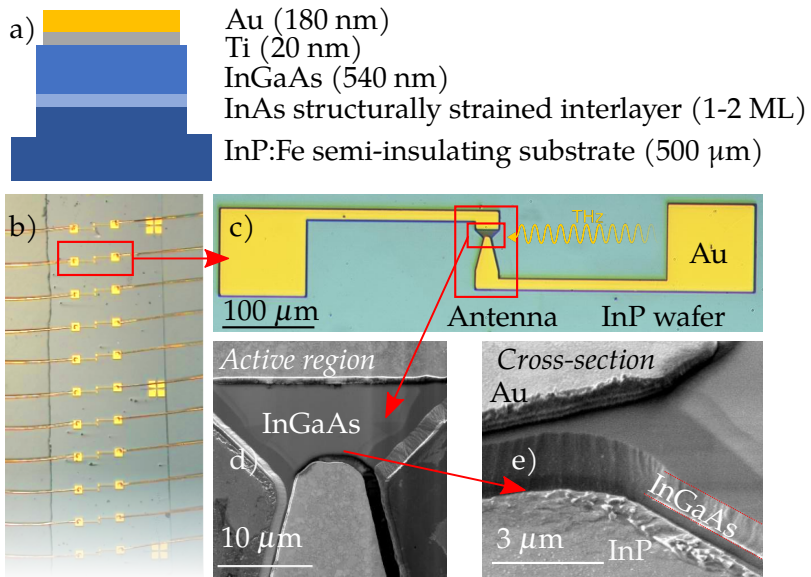


Figure 6.1: Structure of the bow-tie InGaAs diode for THz detection. a) Schematic cross-section of fabricated diode. b) A fragment of a completed sensor in total comprised of 16 bow-tie diode pixels with bonded Au wires. c) A single bow-tie diode with Au contact pads for bonding. d) AFM image of active region. e) AFM image of cross-section of active region. Adapted from [89].

of the device are given in Fig. 6.2.

The structure for device fabrication was grown using molecular-beam-epitaxy on InP semi-insulating substrate: monolayer of InAs and 534-nm thickness  $\text{In}_{0.54}\text{Ga}_{0.46}\text{As}$  over it. Electrical contacts were made by evaporation of Ti (20 nm) and Au (180 nm), followed by the annealing at 400°C temperature for 10 s and patterning of a mesa structure of 1.3  $\mu\text{m}$  height by optical lithography and wet etching [66].

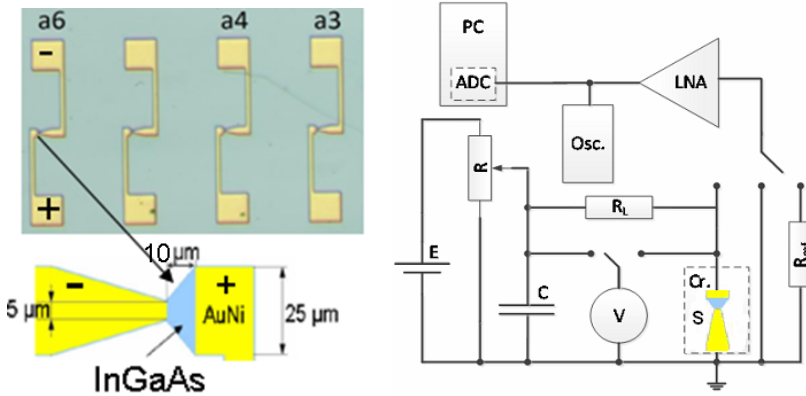


Figure 6.2: Schematic view of investigated bow-tie devices and their dimensions (on the left) and the noise measurement circuit (on the right): S is the investigated bow-tie THz detector;  $R_L$  is the load resistor;  $R_{ref}$  is the reference resistor; LNA is the low-noise amplifier; ADC is the analog-to-digital converter (National Instruments TM PCI 6115 board); PC is the personal computer; Osc. is the oscilloscope; Cr is the cryostat (DN 7704); V is the voltmeter. Adapted from [88].

After growth, the epitaxial layers were studied via series of semiconductor characterisation methods to determine the quality of the grown structure. High-resolution X-ray diffraction (HRXRD)  $\omega - 2\theta$  scans were performed to determine the crystalline structure, later, the grown structures were investigated optically. As the tool for studies, room temperature photoreflectance (PR) spectra (see Fig. 6.3(a)) for the epitaxial InGaAs layers were measured aiming to determine internal electric field in the structure. It is associated Franz-Keldysh oscillations (FKO) which in turn indicate the existence of the internal electric field in the samples. By analysing FKO (see Fig. 6.3(b)) above the band edge, it is possible to estimate the strength of the electric field from electro-optic energy [90]. Evaluation indicates that the strongest

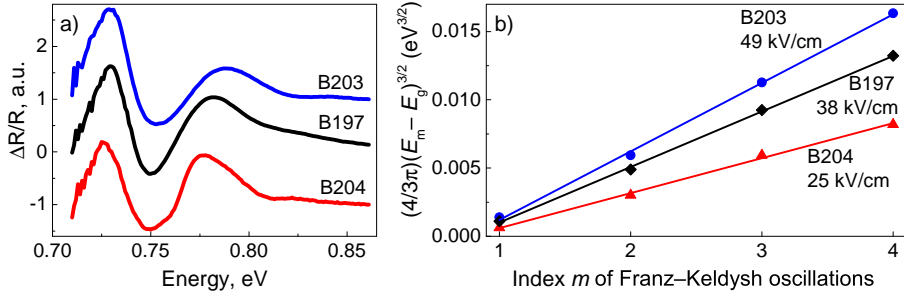


Figure 6.3: Photorefectance spectra of InGaAs layers (a), each spectrum shifted vertically by 1 for clarity; and plots of the quantity  $(4/3\pi)(E_m - E_g)^{3/2}$  versus index  $m$  of Franz-Keldysh oscillations for epitaxial layers (b). Adapted from [P2].

electric field – reaching 49 kV/cm – contains the structure B203.

To complete the characterisation, noise characteristics at forward and backward bias were measured within the frequency range from 10 Hz to 20 kHz varying lattice temperature from 77 K to 300 K. Experimental set-up for low-frequency noise investigation is given in Fig. 6.2. As one can see, the set-up is composed of low-noise amplifier, filter system and analog-to-digital converter (National Instruments PCI 6115 board). The set-up enabled noise measurements in frequency range from 10 Hz to 1 MHz [88]. During the measurements, the load resistance was normally selected to be 30-50 times higher than the resistance of the sample in order to operate in a constant current mode. The current-voltage (I-V) characteristics have been measured by Agilent Semiconductor Device Analyzer B1500A.

Typical low-frequency noise characteristics of investigated bow-tie diodes at different voltages at room temperature (295 K) with exclusion of thermal noise are presented in Fig. 6.4(a). Results show that spectrum of voltage fluctuations is close to  $1/f$ -type spectrum, and the character of spectrum does not depend on applied voltage value. The noise spectra for backward direction at room temperature are almost the same as for forward direction. Voltage fluctuations spectra of  $1/f$ -type indicate that the origin of noise in investigated devices at room temperature are due to superposition of charge carrier capture and emission processes in defects of the interface between InAs and  $\text{In}_{0.54}\text{Ga}_{0.46}\text{As}$  layers.

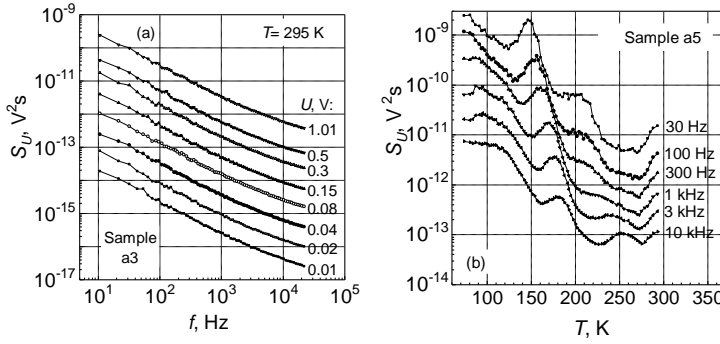


Figure 6.4: (a) Voltage fluctuation spectra of bow-tie diode at different forward voltages at room temperature (295 K). (b) The spectral density of voltage fluctuations dependencies on temperature at different frequencies at forward bias 0.3 V.

At low temperature (77 K) operation, noise features changes, asymmetry becomes pronounced, and voltage fluctuation spectral density at forward bias is about half an order larger than at backward one. One can note that the temperature variation suggests an idea that different recombination centers can be responsible for noise properties of the devices at different current directions. At higher voltages ( $> 0.5$  V) the spectral density of voltage fluctuations increases faster than  $U^2$  due to increase of differential resistance of the investigated devices. Figure 6.4(b) displays the spectral density of voltage fluctuations dependencies on temperature at different frequencies. The noise dependencies on temperature have clearly expressed peaks which are proportionally related with sample resistance increase. The noise level peaks appear at temperature where the effective relaxation time  $\tau_{ieff}$  fulfils such condition  $2\pi f_0 \tau_{ieff} = 1$ .

Besides, every measured device had its own collection of Lorentzians at a particular temperature and applied voltage ranges. On average, the noise level from device to device was nearly the same. The variation of noise level from sample to sample is due to the limited number of active centers in device and their position in the interface layer between InAs and  $\text{In}_{0.54}\text{Ga}_{0.46}\text{As}$  layers. Activation energy,  $\Delta E$ , of charge carrier capture and emission processes was calculated according

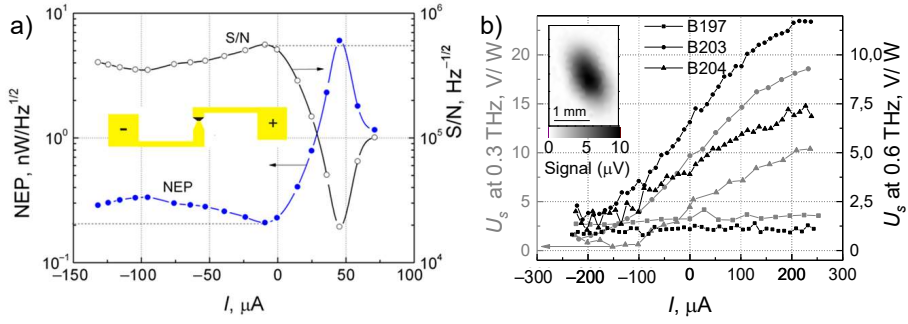


Figure 6.5: Noise equivalent power (NEP) at 0.6 THz (a) and voltage sensitivity (b) In/Ga ratios at 0.3 THz and 0.6 THz frequency with modulation frequency of 1 kHz. Inset in the panel (a) shows the schematic design of the InGaAs bow-tie diode. Inset in the panel (b) indicates the raster scan of the 0.6 THz beam profile at the focal plane obtained panel with detector B203. Adapted from [P2].

to Arrhenius law:

$$\tau_{eff} = \tau_0 \exp\left(\frac{\Delta E}{kT}\right) \quad (6.1)$$

where  $T$  is the absolute temperature. The activation energy values were found to be in the range from 0.003 eV to 0.063 eV. The values of activation energy of observed in charge carriers capture and emission processes allow us to infer that examined processes can be related to the presence of the defects in  $\text{In}_{0.54}\text{Ga}_{0.46}\text{As}/\text{InP}$  interface layer. The obtained results demonstrate that some structural defects are similar for all investigated batch of device, and they are responsible for the intensive charge carrier capture and emission processes.

Figure 6.5 depicts the noise equivalent power (NEP) and sensitivity as a function of current for all types of the studied samples at frequencies of 0.3 THz and 0.6 THz. It is seen that The NEP of the B203 sample as a function of current (panel (a) of Fig. 6.5) shows weak dependence at negative bias, and the minimal value of around around 200 pW/ $\sqrt{\text{Hz}}$  is reached when the current approaches zero value. With the increase of forward bias the NEP value reaches the maximum value when current approaches zero value. With the increase of forward bias the NEP value reaches the maximal value of 6 nW/ $\sqrt{\text{Hz}}$  at 5  $\mu\text{A}$ . It is worth noting that the minimal NEP value obtained here — around 200 pW/ $\sqrt{\text{Hz}}$  — is much smaller than that reported earlier — 4 nW/ $\sqrt{\text{Hz}}$  [66] — is

due to the more optimal growth conditions.

One can note, however, that statistically, sample to sample, the NEP varies in the range of 200 – 600 pW/ $\sqrt{\text{Hz}}$ .

As it is seen, sensitivity of InGaAs bow-tie diodes fabricated from the wafers B203 and B204 increases with current and reaches 17.5 V/W and 10 V/W at 0.3 THz and 12.5 V/W and 7 V/W at 0.6 THz, respectively, at the bias current of 0.2 mA. Higher voltage sensitivity of the detector B203 is caused by the larger asymmetry in the IV curves and stronger built-in electric fields in comparison to other studied samples.

Application of the detector B203 for THz imaging is demonstrated by raster scanning THz beam profile at 0.6 THz plotted in the inset in Fig. 6.5 (b) which illustrates suitability of the diode for THz imaging aims.

To finalise, it is reasonable to compare different types of bow-tie diodes based on different materials. The comparison is given in table 6.1 below. It shows that InGaAs bow-tie diodes fabricated using this technological approach can be compared favourably with previously reported AlGaIn/GaN, AlGaIn/GaN, GaAs, InGaAs based detectors both in sensitivity and NEP.

<b>Detector (sample)</b>	<b>R, V/W</b>	<b>NEP, nW/<math>\sqrt{\text{Hz}}</math></b>
InGaAs diode (this work)	10	0.2
AlGaIn/GaN HEMT [91]	2.6	0.60
AlGaIn/GaN BT [91]	12	0.45
InGaAs BT [68]	10	5.8
GaAs BT [63]	0.3	N/A
AlGaIn/GaN nano-HEMT [92]	N/A	5.0
AlGaIn/GaN TeraFET [93]	N/A	0.042

Table 6.1: Comparison of responsivity (R) and noise equivalent power (NEP) values of THz radiation detectors. N/A – data not available. Adapted from [91].

In conclusion, InGaAs layers grown by molecular epitaxy with beam equivalent pressure In/Ga ratio equal to 2.06 is found to be the most suitable for fabrication of room temperature bow-tie THz detectors exhibiting sensitivity in the range of 10 V/W and noise equivalent power below 1 nW/ $\sqrt{\text{Hz}}$  at 0.6 THz due to strong built-in electric field effects.

The results of effect of InGaAs bow-tie diode growth conditions,

characterization and sensing performance characterization were published in P2.



## 7. FIBONACCI (BIFOCAL) IMAGING

Practical usage of compact THz imaging and spectroscopy systems in real outside laboratory environment still meets significant obstacles. One the main hurdles is a challenging need to overcome low THz emitters power issue, which in optoelectronic photoconductive THz systems, as a rule, is in the range of microwatt, while in the case of compact, electrically pumped THz emitter, e. g., room-temperature quantum cascade lasers, it does not exceed mW scale [94]. Exciting development in increasing sensitivity and reducing noise equivalent power (NEP) of THz sensors, for instance, in microbolometers [8] and nanometric field effect transistors [95,96] can, in principle, partly compensate this difficulty. However, these technological achievements do not provide satisfactory solutions for practical implementations of THz imaging systems – effective operation requires not only reliable, compact design of optical elements and their alignment-free solutions – to deliver a versatile application of the system one needs to have an option to engineer the THz optical beam varying focus shape in accordance to the requirements of an implementation task.

In this section, we suggest, discuss and demonstrate advantages of so-called Fibonacci or bifocal THz imaging at 0.6 THz based on silicon diffractive zone plate fabricated by laser ablation technology [50]. We show that Fibonacci or bifocal imaging can be realized using monochromatic THz light via specially designed zone plate. Zone plates modelled by three-dimensional finite-difference-time-domain method displayed bifocal focusing operation. Features of the performance were investigated both theoretically and experimentally via spatial beam profiles, the distance between the foci and the focal depth at frequencies of 0.3 THz and 0.6 THz. Terahertz images of various packaged objects at

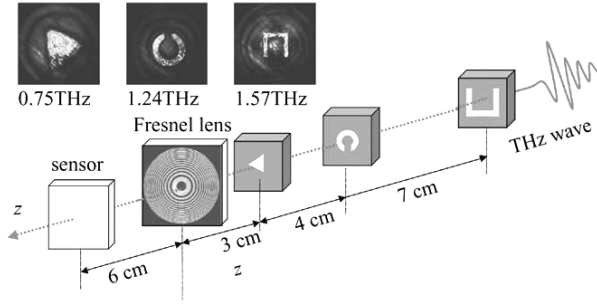


Figure 7.1: Schematic illustration of the tomographic imaging with a Fresnel lens. Targets at various locations along the beam propagation path are uniquely imaged on the same imaging sensor plane with different frequencies of the imaging beam. Three plastic sheets were cut with different patterns placed 3 cm, 7 cm, and 14 cm away from the Fresnel lens. The multiple patterns are imaged on the sensor at a distance of 6 cm from the Fresnel lens, with inverted tomography images of the patterns at the frequencies of 0.75 THz, 1.24 THz and 1.57 THz, respectively. The measured image size is determined by the frequency dependent magnification factor, which is defined as  $z'/z$ . Reprinted by permission from Springer Nature Customer Service Centre GmbH: T-ray imaging and tomography, *Journal of Biological Physics*, S. Wang et al. [97], ©2003

0.6 THz frequency were simultaneously recorded with the spatial resolution of the wavelength in two different planes of the packaged volume.

As it is known [97], the focal length of a Fresnel lens is linearly proportional to the frequency of the light illumination:

$$f_v = \frac{r_p^2}{2\lambda} = \frac{r_p^2}{2c} v \propto v \quad (7.1)$$

where  $r_p^2$  is the Fresnel zone period with a dimension of area,  $\lambda$  is the wavelength,  $c$  is the speed of light, and  $v$  is the frequency. The focal length  $f_v$  is linearly proportional to frequency  $v$ .

Femtosecond-lasers based optoelectronic THz time-domain systems using even different materials for THz generation, as a rule, exhibit broadband spectra of THz radiation [98]. This unique property of THz time-domain systems allows tomographic imaging of a target using multiple frequencies. In other words, using a Fresnel lens at different frequencies of the imaging beam, it is possible to image the objects at various positions along the beam propagation path onto the same imaging plane as it seen in Fig. 7.1.

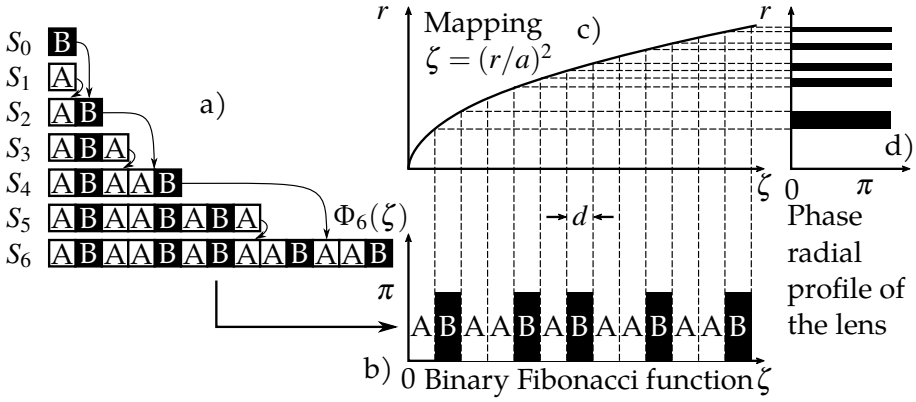


Figure 7.2: Scheme for the construction of the radial profile of a Fibonacci zone plate from Fibonacci sequence. (a) Generation of Fibonacci structures based on the Fibonacci sequence according to the rule  $S_{j+1} = \{S_j S_{j-1}\}$ . (b) A binary  $(0, \pi)$  phase function,  $\Phi_j(\zeta)$  is constructed from a previously generated Fibonacci structure. (c) A nonuniform mapping function. (d) Resulting phase radial profile on the lens. Adapted from [100].

This procedure enables the reconstruction of an object's tomographic contrast image by assembling the frequency-dependent images.

In this section, the aforementioned concept was converted into the continuous wave and discrete frequency operation mode via engagement of a Fibonacci diffractive lenses. In contrast to recently presented 3D-printed diffractive THz lenses [99], we demonstrate design, operation, and high-resolution imaging of a high-resistivity silicon-based Fibonacci lens for 0.6 THz frequency. The focusing performance and engineered beam features were investigated theoretically and experimentally by measuring spatial profiles, the distance between the foci and focal depth at 0.3 and 0.6 THz. The ability to perform simultaneous imaging with the wavelength resolution of two planes separated by a 7 mm distance was experimentally revealed. The multifocal imaging results were compared with the performance of the phase zone plate designed of the same diameter and material.

The Fibonacci lens design relies on the Fibonacci sequence principle when the next number of the sequence is obtained adding up the two preceding ones:

$$\{0, 1, 1, 2, 3, 5, 8, 13, 21, 34, \dots\}.$$

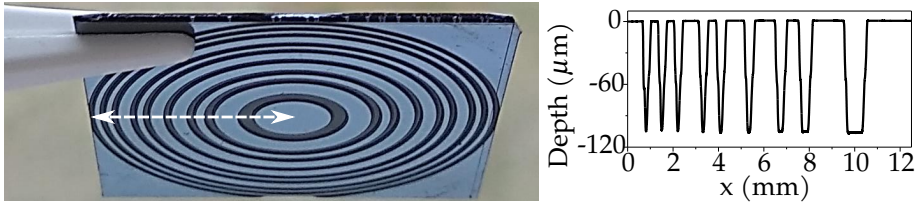


Figure 7.3: The photo of the silicon Fibonacci lens for 0.6 THz and its cross-section profile of laser ablated grooves in the silicon surface. Adapted from [PR2].

Based on the Fibonacci numbers, a binary periodic Fibonacci structure can be composed indicating that each element of the sequence is found as the concatenation of the two previous elements.

Fibonacci sequence has been employed in the development of different photonic devices [101], and spiral zone plates [102]. It was shown that Fibonacci lenses are inherently bifocal with the ratio of the two focal distances approaching the golden mean [100]:

$$\phi = \lim_{x \rightarrow \infty} F_j / F_{j-1} = (1 + \sqrt{5})/2 \approx 1.61803... \quad (7.2)$$

Based on the Fibonacci numbers, a binary aperiodic Fibonacci sequence can also be generated of the sequence is obtained simply as the concatenation of the two previous element with two seed elements as shown in Fig. 7.2. For example,  $S_1 = \{A\}$  and  $S_0 = \{B\}$ . Then, each element  $S_{j+1} = \{S_j S_{j-1}\}$ . Therefore,  $S_2 = \{AB\}$ ,  $S_3 = \{ABA\}$ ,  $S_4 = \{ABAAB\}$ ,  $S_5 = \{ABAABABA\}$ , etc.

The design of the lens was constructed using the Fibonacci sequence, i. e. the next number of the sequence was obtained, adding up the two preceding terms  $F(n) = F(n-1) + F(n-2)$ , where  $F(0) = 0$  and  $F(1) = 1$ . In optical language, the Fibonacci lens structure represents itself as a sequence in which every next element is determined as the concatenation of the two previous elements resulting in a non-uniform structure with the radial profile [100].

We extend the given concept using silicon diffractive optics approach calculating electric field distribution in a space after the bifocal diffractive silicon zone plate using the three-dimensional finite-difference-time-domain (3D FDTD) method [71]. The normalized

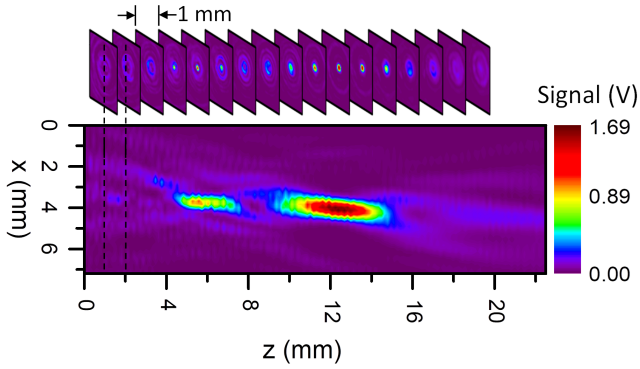


Figure 7.4: Experimental demonstration of 0.6 THz radiation beam profiles focusing evolution along the beam propagation path. The cross sections represent the beam change in the focal plane direction. The distance between cross sections is 1 mm. 2D images consist of  $66 \times 67$  pixels. Pixel size,  $0.1 \text{ mm} \times 0.1 \text{ mm}$ . The dashed line represents the cross section position in the  $xz$  plane.

electric field was calculated in the whole simulation volume varying the spatial resolution from 0.01 to 0.115 mm. To simplify the simulation, symmetry conditions of the structure were brought into action, and the absorbing boundary conditions were set in all the directions. Silicon as a highly efficient material for phase Fresnel lenses [50] was chosen for the Fibonacci (bifocal) lens fabrication. More specifically, monocrystalline silicon orientation (110), with resistance 0.01–1M $\Omega$ cm and refractive index 3.46 was used to produce a lens with the outside diameter of 24 mm. The lenses were made-up via direct laser writing technique based on industrial-scale laser-direct-write (LDW) system using a 1064 nm wavelength, 13 ps duration pulse, 1 MHz repetition rate, and a 60  $\mu$ J peak energy laser (Atlantic 60 from Ekspla Ltd.) [50].

The photo of the silicon Fibonacci lens for 0.6 THz and its cross-section profile of ablated grooves in the silicon surface are given in Fig. 7.3. Nonuniform structure of the lens is clearly visible; cross-section profile indicates that the ablated grooves near the center and the edge of the diffractive element are nearly equally ablated to the depth of 100  $\mu$ m.

Experimental demonstration of the Fibonacci focusing at 0.6 THz is presented in Fig. 7.4.

The THz radiation delivered by an electronic multiplier source was

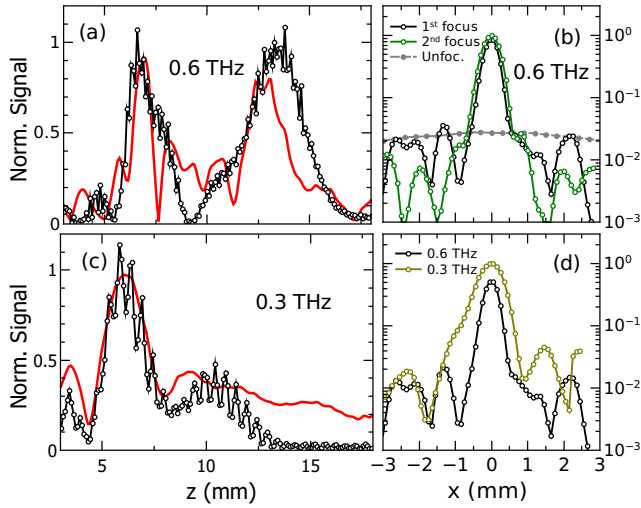


Figure 7.5: Normalized THz radiation power distribution along (a)  $z$  axis and along (b)  $x$  axis at the 1st and 2nd focus measured for 0.6 THz frequency radiation. The unfocused relatively scaled 0.6 THz radiation profile is depicted for comparison. The THz power distribution for 0.3 THz is depicted along (c)  $z$  axis and (d)  $x$  axis where it is compared with the distribution along  $x$  axis for 0.6 THz measured at the 1st focus. Red solid lines in panels (a) and (c) are the results of simulation using 3D FDTD method. Adapted from [P3].

collimated by a 12 cm focal length high-density polyethylene lens and recorded by a resonant THz antenna-coupled microbolometer detector [8]. The distribution along the beam propagation direction revealed two clearly resolved foci, at 6.7 and 13.4 mm away from the lens, located at positions determined by the Fibonacci numbers. One can note that Airy disks were observed between the first and the second focal spots. The distance between the foci and the focal depth at frequencies of 0.3 THz and 0.6 THz confirmed the origin of the Fibonacci lens performance. Both experimental and 3D FDTD simulation results of THz beam power distribution along both  $x$  and  $z$  axes formed by Fibonacci lens are presented in Fig. 7.5.

Terahertz images of objects given in Fig. 7.6.(a) at 0.6 THz are displayed in panels (b) and (c). Results show that using multilevel phase Fresnel lens the THz images of good quality (signal-to-noise ratio, SNR, is more than 800) can be recorded aligning imaging to relevant foci. It is clearly seen from panel (b), when the focus is tuned to the first plane, it enables to image objects in the first plane, even pencil-written letters

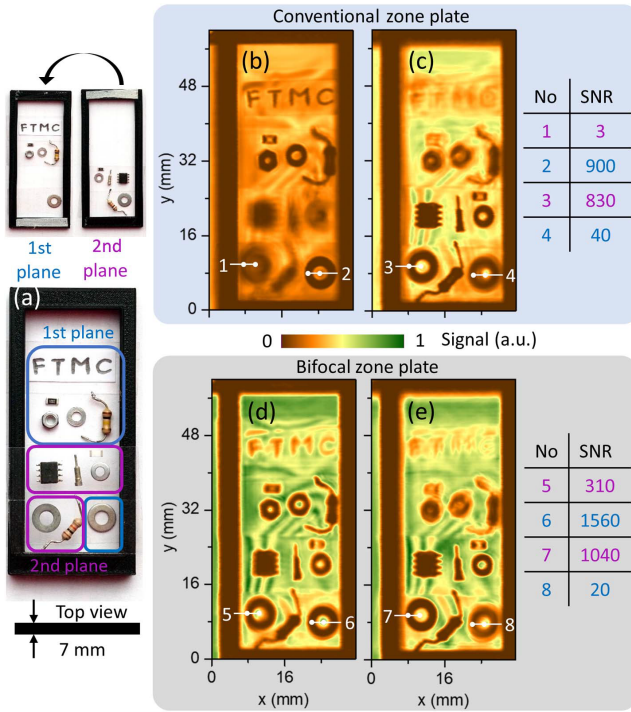


Figure 7.6: THz images at two planes, separated by 7 mm spacer obtained simultaneous recording at 0.6 THz. Photos of the sample (a). THz images at 0.6 THz obtained using conventional zone plate: image focused on the 1st plane (b) and focused on the 2nd plane (c). Images obtained using bifocal zone plate: optimal image taken by moving the sample along z-axis to achieve the best contrast in both sample planes (d) and image taken at the highest contrast in the 2nd plane contrast (e). Positions of signal amplitudes used for SNR calculations are represented as white lines with dots. Reprinted from [P3].

©2018 Optical Society of America.

“FTMC” are evidently resolved. However, the image quality of the objects placed in the second plane is not tolerable — images are blurred and SNR is in the range of 40. A similar picture was obtained with the tuning to the second plane.

In contrast, in the bifocal lens case, THz image was recorded collecting the THz light from both foci in a single scan. Results are shown in Fig. 7.6(d). Since both planes are in focus now, all the objects placed in both planes as well as pencil-written letters “FTMC” are clearly resolved. S/N ratio in the first and the second foci is, respectively, in the order of 1500 and 300.

For comparison, at the same recording conditions, the imaging system was tuned for collection of the THz radiation just from the second focus of the bifocal zone plate in order to compare the resolution with the conventional Fresnel lens. If compare image given in Fig. 7.6(e) with that in Fig. 7.6(c), one can see that second sample plane spatial resolution is comparable to the conventional zone plate image, while the image resolution in the first plane is strongly decreased. It allows to infer that two-plane THz imaging can be performed using a Fibonacci (bifocal zone) plate reaching simultaneous wavelength resolution in both foci.

Spatial resolution in the bifocal recording was estimated to be of 1.6 factor of wavelength, i.e.  $1.6 \times \lambda$ .

Hence, we enriched the previously reported [49] arsenal of tools to engineer THz beam profile in imaging experiment opening thus new area for spectroscopic THz imaging applications [69].

In conclusion, Fibonacci or bifocal terahertz (THz) imaging based on silicon diffractive zone plate in a continuous wave mode at 0.6 THz is demonstrated both theoretically and experimentally. Zone plates were simulated using the three-dimensional finite-difference time-domain method. Silicon as a low absorbing material was used in the laser ablation process to fabricate the Fibonacci structures. To illustrate the Fibonacci focusing, the performance was studied both theoretically and experimentally by determining spatial profiles, the distance between the foci and the focal depth at frequencies of 0.3 THz and 0.6 THz. Terahertz images of various packaged objects at 0.6 THz frequency were simultaneously recorded with the spatial resolution of wave-



length in two different planes separated by 7 mm distance. Imaging performance using the Fibonacci lens is compared with the operation of the conventional silicon phase zone plate.

Results on Fibonacci focusing performance were published in article [P2].

## 8. BESSEL ZONE PLATES FOR THICK OBJECT IMAGING

Narrow depth of field is one of the most critical properties of imaging systems that determine whether the object is in focus or is blurred in the resulting image. Next step in evolution of facilities of bifocal Fibonacci THz imaging [P3] to a system that would not be constrained by predefined focal lengths and would allow significantly less precision in sample placement is to extend the focus of the systems. In other words, arrangement of Bessel beams can be possible solution for the mentioned issues. Bessel beam has a remarkable property that it does not diverge with propagation in the  $z$  direction and maintain an unreduced transversal distribution as the beam propagates in a non-diffractive way.

In particular, it is important in postal security applications where there is a strong requirement to scan and identify content of thick packaging objects. One can note that the thickness of conventional post packages can vary from several millimeters up to 20 mm. Hence, to provide correct inspection, it is essential to have a possibility to change the focus distance or to engineer the THz optical beam so that the image quality cannot be strongly affected even if objects are spatially distributed in a bulky and relatively thick volume.

In experiment and in practical implementation, an axicon can be used to generate quasi-Bessel beam, almost non-diffracting beam within the depth of field (DOF) of the axicon. In visible range, unique non-diffracting nature of Bessel beams is applied in a variety of areas such as different types of microscopy [105–107], laser ablation [108, 109], etc. While Bessel beam generation in THz range was demonstrated in

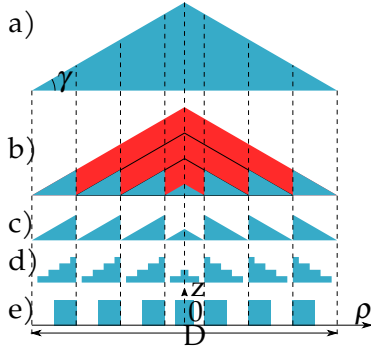


Figure 8.1: Steps to transform bulk axicon into a diffractive Bessel zone plate. (a) A bulk axicon. (b) An axicon with the unwanted material (red part) removed. (c) An equivalent axicon with continuous profile. (d) An equivalent diffractive Bessel zone plate (BZP) quantized into four levels. (e) An equivalent binary axicon. Adapted from [103].

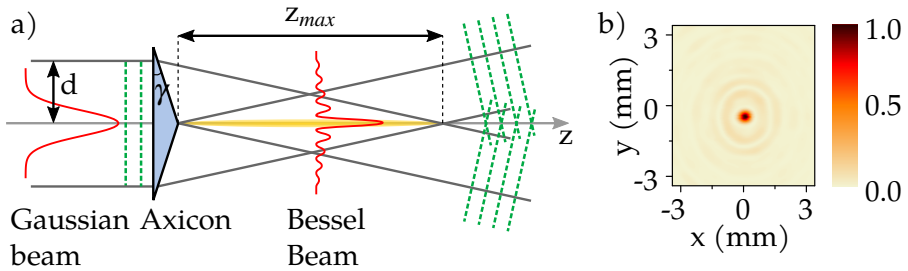


Figure 8.2: (a) Bessel beam formation from incoming Gaussian beam by axicon (adapted from [104]). (b) Beam intensity distribution  $xy$  scan at the center of the Bessel zone formed by Bessel zone plate at 0.6 THz.

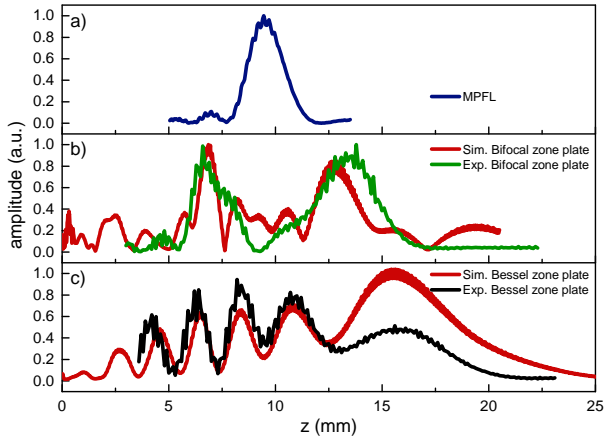


Figure 8.3: Comparison of diffractive beam focusing element power distribution along  $z$  axis at 0.6 THz frequency. a) Experimental results of multi level Fresnel zone plate [50] with 4 phase quantization levels and 10 mm focal length, b) experimental and simulation results of bifocal Fibonacci diffractive element and c) experimental and simulation results of Bessel zone plate.

free THz tomography [110], detection of insects in flour [111], etc., the Gaussian beam was converted into the Bessel beam using bulk axicons. As one of the aims of contemporary optical systems is overall compactness bulk axicons [112], one needs to reduce their dimensions. It can be done by replacing conventional bulk axicons into a diffractive Bessel zone plate (BZP) [103].

A classical bulk axicon was first introduced by McLeod in 1954 [113] as illustrated in Fig. 8.1(a), where  $D$  is the aperture diameter and  $\gamma$  is the prism angle. As with other optical lenses bulk axicon profile can be well approximated with discrete axicon, whose performance is equivalent to that of the bulk axicon.

In the given chapter, thin and compact Bessel zone plates (BZP) based on silicon multi-phase diffractive optics is suggested to engineer the THz optical beam. The BZP design was calculated to be used with 0.6 THz source in transmission geometry. Designed zone plate was simulated employing three-dimensional finite-difference time-domain (3D FDTD) modeling method. The Bessel zone plate producing 10 mm depth of field can be suited for compact solutions in security-oriented THz imaging systems. A design THz focusing Bessel zone plate with dimensions of 20 mm  $\times$  20 mm  $\times$  0.5 mm (W $\times$ H $\times$ D) was based on sili-

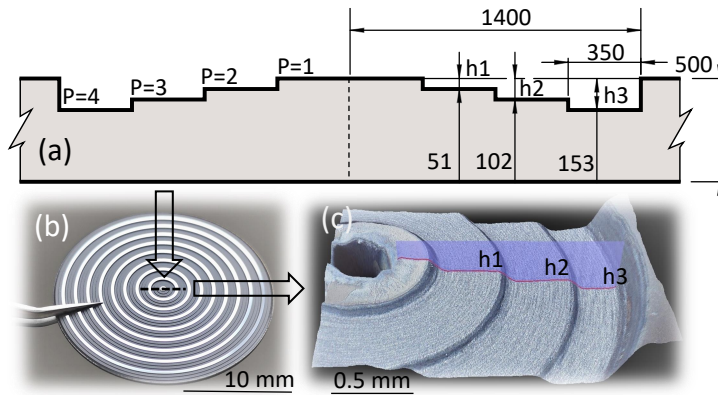


Figure 8.4: (a) Bessel zone plate design and its cross-section of the central part with marked dimensions in microns of four phase quantization levels. (b) The photo of thin silicon-based Bessel diffractive element for the 0.6 THz. (c) 3D reconstruction of the zoomed area in the center part displays ablated and polished silicon surface,  $h$  indicates places where groove depth was measured using Hirox digital microscope. Reprinted from [P4].

con. It intends to resolve a problem of focusing THz beam into desired areas when the sample is thick.

Optical setup was based on idea of use of two identical axicons [113] (in this case BZPs) to form a Bessel beam with the first BZP and to use in the experimental setup the second BZP for enhanced imaging purposes in terms of increased compactness. The discrete axicons containing 4 phase quantization levels were fabricated from a high-resistivity silicon by employing laser ablation technology allowed to extend the focal depth up to 20 mm with minimal optical losses and refuse employment of bulky parabolic mirrors in the imaging set up.

To illustrate the quality of the Bessel THz imaging, a specially designed stack of targets for thick media imaging measuring  $30 \times 60 \times 3 \text{ mm}^3$  was 3D printed with PLA filament using Ultimaker 2 printer. Figure 8.5(a) demonstrates principle of the imaging procedure, where the object, with thickness varied from 3 mm to 12 mm, was placed between two silicon BZP, i. e. no parabolic mirrors were employed in focusing of collimated beam onto the sample and collimating the transmitted radiation. For comparison, the same imaging procedure was also performed using conventional multilevel phase Fresnel lens with  $f = 10 \text{ mm}$  and  $P = 4$  characterized in Fig. 8.3(a). Imaging

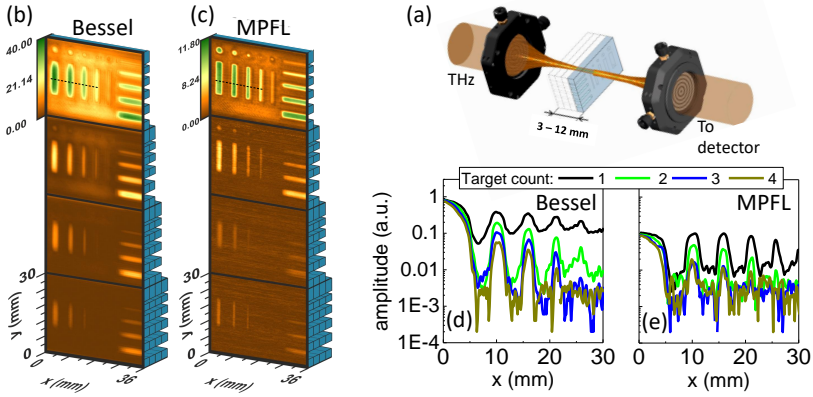


Figure 8.5: (a) Part of Bessel imaging setup displaying object under test placed between two silicon BZP. (b) and (c) – Stacks of 1 to 4 identical targets were imaged using Bessel zone plates and conventional MPFL, respectively, aiming to evaluate THz imaging performance of thick objects. (d) Beam profiles at  $y=17$  mm (position is marked as dashed black line in (b) and (c)) of obtained images using BZP. (e) MPFL beam profiles are shown for comparison. Reprinted from [P4].

results of the different sample thicknesses using Bessel zone plate and MPFL are given in Figs. 8.3(b) and 8.3(c). Varying the content of the stack from 1 to 4 identical targets, the Bessel imaging advantage is revealed via obtained horizontal profiles up to stack thickness of 12 mm in Figs. 8.3(d) and 8.3(e). As we can see in Figs. 8.3(d) and 8.3(e), in the case of 3 mm aperture and thickness of 1 sample  $\text{SNR} = 8$  is achieved with multilevel phase Fresnel lens while  $\text{SNR} = 4$  was obtained with BZP is worse due to self-healing effect [114] and much longer depth of field of Bessel beam. The advantage of BZP appears when the stack is composed of 2 or more samples:  $\text{SNR}$  achieved with BZP increases from 2 to 4 times better values than multilevel phase Fresnel lens.

Additionally, up to 5-fold enhanced contrast and increased resolution up to  $0.6 \lambda$  by applying deconvolution algorithms can be achieved in the recorded images.

To conclude, Bessel terahertz imaging of thicker than 10 mm objects using silicon multi-phase diffractive elements in continuous wave mode at 0.6 THz was designed and experimentally demonstrated. Discrete axicon containing 4 phase quantization levels manufactured from high-

resistivity silicon wafer allowed to extend the focal depth up to 20 mm with minimal optical losses permitting significantly less precise imaging sample placement in the optical axis. Furthermore, deconvolution algorithms allowed for up to 5-fold enhanced contrast and increased resolution up to  $0.6 \lambda$  in the recorded images. Simulated focusing performance of Bessel zone plates using three-dimensional finite-difference time-domain method agreed well with experimental data.

The results on BZP design and imaging performance was published in [P4].

## 9. IMAGING WITH SPATIAL FILTERING METHODS

As was mentioned above, THz imaging can serve as a versatile instrument to disclose contents of various packages or discriminate its constituents. The image itself can be recorded using differently engineered optical beam – either focused or collimated. The first method allows so called raster scan – THz images come from scanning the object with the focused beam and registering the focused radiation on the detector making thus induced signal much larger. Quality of the image can be good due higher signal-to-noise ratio. However, the time needed to record the image pixel-to-pixel can be relatively long, in particular, if there is a need to resolve weakly absorbing objects or discriminate them in a packaged stuff.

As one of the possible compact solutions for sources in subTHz range can be advanced by SiGe bipolar CMOS (BiCMOS) devices operating at 60 GHz that are more widely adopted for automotive radars [115]. They also can serve in wireless internet service or in unlicensed 5G cellular communication [116]. Also, semiconductor industry is planning mass production of higher frequency subTHz devices [117] and, furthermore, the fact that current state of the art research SiGe BiCMOS devices reach higher than 60 mW output power at frequencies higher than 200 GHz [118, 119] as well as rapid development of CMOS based THz detector arrays [32, 120] pave way for cost effective THz imaging using the second method – usage of collimated beams – which would allow real-time imaging as whole object images can be captured without raster scanning. Additionally, collimated beams employment will require uniform illumination of



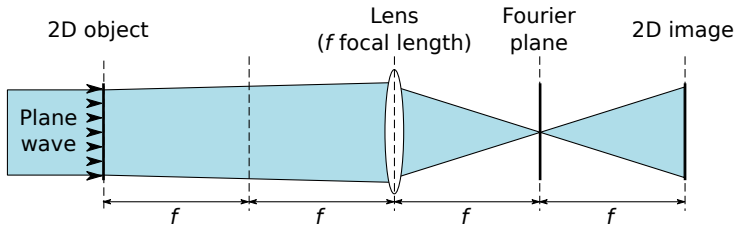


Figure 9.1: Schematic view of two-dimensional object, lens, Fourier plane and the resulting two-dimensional image positions relative to focal length  $f$  of the lens.

the the whole area [121, 122] which, as a consequence, will introduce precise adjustment challenges. Moreover, apertures of imaging optical elements need to be large in comparison with diameters of optical elements and propagation distances. Therefore, novel optical solutions are needed both in optical beam engineering as well as design and manufacturing compact optical elements with large aperture sizes and reasonable focal lengths.

In what follows, we introduce spatial filtering methods into THz imaging employing both single pixel and arrays of the sensitive antenna-coupled titanium-based microbolometers [8]. Terahertz images of low absorbing objects are under unfocused THz illumination at 0.3 THz frequency. Spatial filtering methods — dark field and phase contrast — are used to create a THz image of object inducing phase changes (uniform amplitude). These methods differ in principles and type of the filter; however, all of them permit to create an intensity pattern corresponding to phase changes in the object. The phase contrast method enables linear mapping between phase shift introduced by the object and recorded intensity pattern.

Spatial filtering methods are well known in microscopy [123]. Conventional or in microscopy usually called the bright field image is usually widely applied if objects under test exhibit strong absorption. The dark field imaging enables good contrast for sub-resolution features, since it only captures high-angle scattered light. Meanwhile, the phase contrast is mostly suitable for weakly absorbing or transparent samples. For instance, in biology, where it allows visualization of shape and density variations.

Spatial filtering requires special type of filter that must be inserted

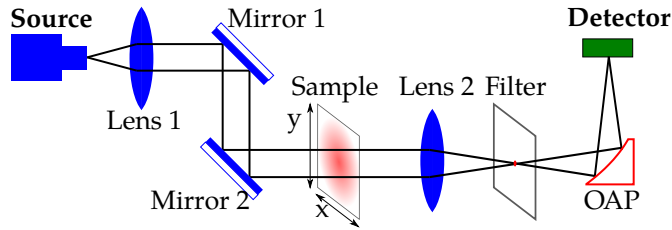


Figure 9.2: Principal scheme of spatial filtering imaging set up for 0.3 THz, where Lens 1 – HDPE lens with  $f = 12$  cm, Mirror 1, Mirror 2 – gold plated flat mirrors, sample, Lens 2 – TPX lens with  $f = 6$  mm, Filter – (1):  $\varnothing 2$  mm circle shaped four paper sheets, (2) –  $\varnothing 2$  mm circle shaped aluminum foil, OAP – off axis parabolic mirror with  $f = 5$  cm. Adapted from [P5].

in the Fourier plane in the used imaging system, and it will affect only some spatial frequencies of the Fourier spectrum of the object. Schematic view of two-dimensional object, lens, Fourier plane and the resulting two-dimensional image positions relative to focal length  $f$  of the lens is shown in Fig 9.1.

Experimental scheme to record THz images using spatial filtering is given in Fig. 9.2.

The dark field imaging [124], schlieren imaging [125] and phase contrast imaging [126, 127] uses different type of filters as specified below.

Two types of filters were used in the experiments: the filter 1, consisting of 2 mm circle shaped four paper sheets, was a phase filter introducing a phase retardation of  $\pi/2$  only in the central part of the Fourier spectrum and enabling thus to create an image using phase contrast method; second one, filter 2, circle shaped aluminum foil of 2 mm diameter, was an amplitude filter, blocking low spatial frequencies, which resulted in creating an intensity image of phase object having dark background (which is related to removal of low spatial frequencies). Photos of the filters are given in Fig. 9.3(e).

We concentrated ourselves to the case of low absorbing or transparent samples, when the object observation and registration of its internal structure grow into a tremendous challenge. It is related to the fact that power detectors record intensity of the radiation which suffers almost no observable change in the given circumstances, and the shift of the phase of incident radiation becomes a single quantity to be recorded.

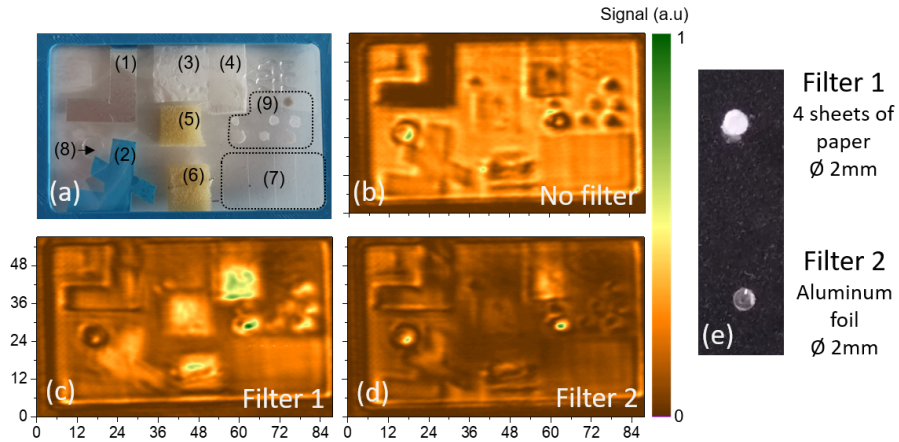


Figure 9.3: Photo of the sample with plastic substrate film, it consists of: (1) metal, (2) rubber, (3) paper towel, (4) napkin, (5) sponge, (6) sponge with metal wire inside, (7) plastic (from 1 to 4 layers), (8) aperture  $\varnothing 4$  mm, (9) dots, made of silicone, acrylic and wax (a). Direct raster scan image of the sample at 0.3 THz (b). Phase contrast images obtained using filter 1 (c) and filter 2 (d). THz image pixel size:  $0.3 \text{ mm} \times 0.3 \text{ mm}$ ; images consist of  $292 \times 190$  pixels. Photo of phase filters (e): filter 1 (4 sheets of paper  $\varnothing 2$  mm), filter 2 (aluminum foil  $\varnothing 2$  mm). Adapted from [P5].

Sample photo and its direct image as well as two corresponding intensity images of phase objects are shown in the corresponding panels (a–d) of Figure 9.3.

It can be easily seen that even direct imaging nicely resolves shapes of all the objects under test. Deeper insight allows to infer that transparent objects like sponge (5 and 6) and paper tissue (4) are much better visible in case of phase contrast method (filter 1), whilst dark field method (filter 2) gives much better results for imaging of thin rubber glove (2), where we can clearly see edges of the rubber shape.

Therefore, spatial filtering methods – phase contrast and dark field methods – can be applied in large aperture THz imaging to resolve weakly absorbing objects in subTHz range using sensitive room temperature detectors, for instance, titanium-based microbolometers. The images of weakly absorbing objects were recorded in unfocused light at 0.3 THz frequency using circle shaped paper sheets as filter in phase contrast and circle shaped aluminum foil in dark field experiments.

In conclusion, terahertz spatial filtering was shown to be useful op-

tical beam engineering tool in THz imaging enabling to resolve and discriminate weakly absorbing or nearly transparent objects in THz range.

The results of spacial filtering method were published in [P5].

## 10. MAIN RESULTS AND CONCLUSIONS

1. It is shown that homodyne phase-shifting scheme can be realized in a simple way by varying the number of office paper sheets in the optical path. It is shown that homodyne THz imaging can serve as a convenient imaging tool to screen low-contrast suspicious inclusions in textiles.
2. Different technological conditions for the InGaAs devices fabricated from InGaAs layers grown by molecular beam epitaxy (MBE) on semi-insulating InP substrate are considered. It was shown that structures exhibit presence of strong built-in electric fields reaching up to 49 kV/cm, which were derived from the photoreflectance spectra.
3. It was demonstrated that for bow-tie InGaAs diodes the spectral density of voltage fluctuations at room temperature is found to be proportional to  $1/f$ , while at lower temperatures, 77–200 K, Lorentzian-type spectra dominate due to random telegraph signals caused by individual capture defects.
4. The obtained results revealed effect of InGaAs layers grown at different beam equivalent pressure (BEP) In/Ga ratios on the low-frequency noise level and the sensitivity of the THz detectors. It was determined that THz detectors grown with BEP In/Ga ratio equal to 2.06 is the most suitable choice to fabricate sensitive InGaAs bow-tie diodes for room temperature operation enabling thus sensitivity in the range of 10 V/W and noise equivalent power below  $1 \text{ nW}/\sqrt{\text{Hz}}$  at 0.6 THz.
5. It was shown that compact Fibonacci (bifocal) terahertz imaging

can be realized using monochromatic THz light sources using diffractive silicon lenses. The focusing performance was silicon phase plates with different quantisation levels were studied both theoretically and experimentally by measuring spatial profiles, the distance between the foci and focal depth at 0.3 THz and 0.6 THz frequencies. The obtained results are compared with relevant data using multilevel phase Fresnel lens.

6. Simultaneous imaging with the wavelength resolution of two planes separated by a 7 mm distance was experimentally demonstrated at 0.3 THz and 0.6 THz frequencies. The multifocal imaging results were compared with the performance of the phase zone plate designed of the same diameter and material.
7. Thin and compact Bessel zone plates based on silicon multi-phase diffractive optics were designed, produced and demonstrated in the THz transmission imaging system.
8. A novel experimental setup using two Bessel zone plates for enhanced imaging purposes and increased compactness was suggested. The discrete axicons containing 4 phase quantization levels were fabricated from a high-resistivity silicon by employing laser ablation technology allowed to extend the focal depth up to 20 mm with minimal optical losses and refuse employment of bulky parabolic mirrors in the THz imaging set up.
9. Compact THz imaging system reveals possibility to inspect objects of more than 10 mm thickness with enhanced contrast, weak dependence on the sample thickness and position due to long focal depth as well as increase its resolution up to high level by applying the deconvolution algorithms.
10. Spatial filtering methods – phase contrast and dark field – can be applied in large aperture THz imaging to resolve weakly absorbing objects in subTHz range using sensitive room temperature detectors, for instance, titanium-based microbolometers. The images of weakly absorbing objects were recorded in unfocused light

at 0.3 THz using circle shaped paper sheets as filter in phase contrast and circle shaped aluminum foil in dark field experiments.

# 11. PUBLICATIONS AND CONFERENCES

## Publications

The main results of the dissertation were published in 5 scientific publications.

- P1 **D. Jokubauskis**, L. Minkevičius, D. Seliuta, I. Kašalynas and G. Valušis, Terahertz homodyne spectroscopic imaging of concealed low-absorbing objects, *Optical Engineering* **58**(02), p. 023104, 2019. DOI: 10.1117/1.OE.58.2.023104
- P2 V. Palenskis, L. Minkevičius, J. Matukas, **D. Jokubauskis**, S. Pralgauskaitė, D. Seliuta, B. Čechavičius, R. Butkutė and G. Valušis, InGaAs Diodes for Terahertz Sensing—Effect of Molecular Beam Epitaxy Growth Conditions, *Sensors* **18**(11), p. 3760, 2018. DOI: 10.3390/s18113760
- P3 **D. Jokubauskis**, L. Minkevičius, M. Karaliūnas, S. Indrišiūnas, I. Kašalynas, G. Račiukaitis and G. Valušis, Fibonacci terahertz imaging by silicon diffractive optics, *Optics Letters* **43**(12), p. 2795, 2018. DOI: 10.1364/OL.43.002795
- P4 L. Minkevičius, **D. Jokubauskis**, I. Kašalynas, S. Orlov, A. Urbas and G. Valušis, Bessel terahertz imaging with enhanced contrast realized by silicon multi-phase diffractive optics, *Optics Express* **27**(25), pp. 36358-36367, 2019. DOI: 10.1364/OE.27.036358
- P5 L. Minkevičius, L. Qi, A. Siemion, **D. Jokubauskis**, A. Sešek, A. Švigelj, J. Trontelj, D. Seliuta, I. Kašalynas and G. Valušis, Titanium-Based Microbolometers: Control of Spatial Profile of Terahertz Emission in Weak Power Sources, *Applied Sciences* **10**(10), p. 3400, 2020. DOI: 10.3390/app10103400

The reprinted articles can be found in the in the end of the thesis. The published articles are available as Open Access from respective publishers with



an exception of [P3] which is provided as preprint version due to copyright considerations.

Scientific publications not included in this thesis:

- N1 R. Ivaškevičiūtė-Povilauskienė, L. Minkevičius, **D. Jokubauskis**, A. Urbanowicz, S. Indrišiūnas, G. Valušis, Flexible materials for terahertz optics: advantages of graphite-based structures, *Optical Materials Express*, **9**(11), p. 4438, 2019. DOI: 10.1364/OME.9.004438
- N2 R. Miškinis, **D. Jokubauskis**, E. Urba, D. Smirnov, L. Gaidamovičiūtė, K. Mikalauskas, A. Sereika, R. Rimeika, D. Čiplys, Investigation of a GaN-Based SAW Oscillator with respect to UV Illumination and Temperature, *Acta Physica Polonica A* **127**, p. 90–92, 2015. DOI: 10.12693/APhysPolA.127.90

The results of this thesis were presented in the following conference proceedings:

- PR1 R. Venckevičius, L. Minkevicius, A. Reklaitis, V. Tamošiūnas, I. Kašalynas, B. Voisiat, D. Seliuta, G. Račiukaitis, **D. Jokubauskis**, G. Valušis, Compact solutions for spectroscopic solid-state-based terahertz imaging systems, *Terahertz Emitters, Receivers, and Applications VIII*, p. 27, 2017. DOI: 10.1117/12.2273353
- PR2 **D. Jokubauskis**, L. Minkevičius, M. Karaliūnas, I. Kašalynas, S. Indrišiūnas, G. Račiukaitis, G. Valušis, Fibonacci subterahertz imaging: features and applications, *Terahertz Emitters, Receivers, and Applications X*, p. 33, 2019. DOI: 10.1117/12.2529012

The results of the thesis were presented at the following conferences:

- C1 **D. Jokubauskis**, L. Minkevičius, D. Seliuta, I. Kašalynas, G. Valušis, Terahertz Homodyne Imaging For Inspection Of Low Absorbing Objects, *44th International Conference on Infrared, Millimeter, and Terahertz Waves*, (Paris, France, 2019), Oral presentation
- C2 L. Minkevičius, **D. Jokubauskis**, I. Kašalynas, S. Orlovas, A. Urbas, G. Valušis, "Imaging of thick objects using silicon Bessel zone plates at 0.6 THz," in *International Conference on Infrared, Millimeter, and Terahertz Waves, IRMMW-THz*, (Paris, France, 2019), Oral presentation
- C3 **D. Jokubauskis**, L. Minkevičius, M. Karaliūnas, S. Indrišiūnas, D. Seliuta, I. Kašalynas, G. Valušis, Homodyne and bifocal imaging approaches for advanced terahertz systems, *French-German THz Conference 2019*, (Kaiserslautern, Germany, 2019), Oral presentation

- C4 **D. Jokubauskis**, L. Minkevičius, M. Karaliūnas, S. Indrišiūnas, D. Seliuta, I. Kašalynas, G. Valušis, Homodyne and bifocal imaging approaches for advanced terahertz systems, *10th THz-Young Scientists meeting*, (Frankfurt am Main, Germany, 2019), Oral presentation
- C5 **D. Jokubauskis**, R. Butkutė, L. Minkevičius, Effect of Molecular Beam Epitaxy Growth Conditions for Terahertz Sensing InGaAs Diodes, *21st International Conference-School "Advanced Materials and Technologies 2019"*, (Palanga, Lithuania, 2019), Poster presentation
- C6 **D. Jokubauskis**, L. Minkevičius, M. Karaliūnas, I. Kašalynas, S. Indrišiūnas, G. Račiukaitis, G. Valušis, Fibonacci subterahertz imaging: features and applications, *SPIE Optical Engineering + Applications*, (San Diego, California, United States, 2019), Oral presentation
- C7 **D. Jokubauskis**, R. Butkutė, L. Minkevičius, Influence Of Molecular Beam Epitaxy Growth Conditions On Terahertz Detection For In-GaAs Diodes, *Open Readings 2019*, (Vilnius, Lithuania, 2019), Oral presentation
- C8 **D. Jokubauskis**, L. Minkevičius, M. Karaliūnas, S. Indrišiūnas, I. Kašalynas, G. Račiukaitis, G. Valušis, Fibonačio terahercinis vaizdinimas, *FTMC FizTech*, (Vilnius, Lithuania, 2018), Oral presentation
- C9 **D. Jokubauskis**, L. Minkevičius, M. Karaliūnas, S. Indrišiūnas, I. Kašalynas, G. Račiukaitis, G. Valušis, Fibonacci terahertz imaging, *Advanced Properties and Processes in Optoelectronic Materials and Systems (Apropos 16)*, (Vilnius, Lithuania, 2018), Poster presentation
- C10 R. Ivaškevičiūtė, L. Minkevičius, D. Jokubauskis, A. Urbanovič, A. Lukša, A. Sakavičius, A. Šetkus, G. Valušis, Carbon nanolayers for diffractive terahertz optics, *Advanced Properties and Processes in Optoelectronic Materials and Systems (Apropos 16)*, Vilnius, 2018 m. spalio 10 d.
- C11 L. Minkevičius, **D. Jokubauskis**, V. Janonis, S. Indrišiūnas, G. Račiukaitis, V. Tamošiūnas, I. Kašalynas, G. Valušis, High Numerical Aperture Diffractive Optics For Imaging Applications At 0.6 THz Frequency, *43rd International Conference on Infrared, Millimeter and Terahertz Waves (IRMMW-THz 2018)*, (Nagoya, Japan, 2018), Oral presentation
- C12 R. Venckevičius, L. Minkevičius, A. Reklaitis, V. Tamošiūnas, I. Kašalynas, **D. Jokubauskis**, D. Seliuta, B. Voisiat, G. Račiukaitis, G. Valušis, Compact solutions for spectroscopic solid-state-based terahertz imaging systems, *SPIE Optical Engineering + Applications*, (San Diego, California, United States, 2017), Oral presentation

- C13 **D. Jokubauskis**, L. Minkevičius, M. Karaliūnas, S. Orlovas, G. Valušis, Bessel Zone Plate Design For Terahertz Imaging, *Open Readings 2018*, (Vilnius, Lithuania, 2018), Poster presentation
- C14 **D. Jokubauskis**, L. Minkevičius, D. Seliuta, I. Kašalynas, G. Valušis, Paslėptų mažos sugerties objektų aptikimas naudojant terahercinę spinduliuotę, *FTMC FizTech*, (Vilnius, Lithuania, 2017), Oral presentation
- C15 **D. Jokubauskis**, L. Minkevičius, D. Seliuta, I. Kašalynas, G. Valušis, Paslėptų mažos sugerties objektų aptikimas naudojant terahercinę spinduliuotę, *42-oji Lietuvos nacionalinė fizikos konferencija*, (Vilnius, Lithuania, 2017), Poster presentation
- C16 **D. Jokubauskis**, L. Minkevičius, R. Venckevičius, D. Seliuta, G. Valušis, Detection Of Low Density Hidden Objects Using Terahertz Radiation, *Open Readings 2017*, (Vilnius, Lithuania, 2017), Poster presentation

## 12. CURRICULUM VITAE

### 12.1 About the author

Domas Jokubauskis was born in 1987 in Šilalė, Lithuania. In 2010 he received his bachelor degree in Computing Physics at Faculty of Physics, Vilnius University. In 2012 he received his masters degree in Physical Technology and Management at Faculty of Physics, Vilnius University. In 2014 he started doctoral studies in Center for Physical Sciences and Technology (FTMC).

### 12.2 Apie autorių

Domas Jokubauskis gimė 1987 metais Šilalėje. 2006 metais baigė Šilalės Stepono Dariaus ir Stasio Girėno vidurinę mokyklą. 2010 metais baigė Kompiuterinės fizikos bakalauro studijų programą Vilniaus universiteto Fizikos fakultete. 2012 metais baigė Fizikinių technologijų ir jų vadybos magistro studijų programą Vilniaus universiteto Fizikos fakultete. 2014 metais buvo priimtas į doktorantūros studijas Fizinių ir technologijos mokslų centre.

# 13. SANTRAUKA

## 13.1 Įvadas

Kalbant apie nematomas šviesos – arba elektromagnetinės spinduliuotės – spektro dalis dažniausiai galvojama apie rentgeno spinduliuotę, naudojamą rentgeno nuotraukų fiksavimui medicinos srityje ir krovinių turiniui tikrinti saugumo srityje. Tai naudinga priemonė, leidžianti pažvelgti į akimi nepermatomų objektų vidų, pvz., identifikuoti paveiktus žmogaus kūno audinius ar išskirti bagažo turinį. Nepaisant privalumų, rentgeno spinduliai yra žalingi žmogaus kūnui ir kitoms gyvoms būtybėms dėl spinduliuotės jonizuojančiosios prigimties [1, 2]. Kita vertus, mažo tankio (pvz., drabužių, plastikų, popieriaus ir pan.) aptikimas rentgeno spinduliuote yra sudėtingas, tad reikia ieškoti kitų technologijų. Viena tokių technologijų yra terahercinė (THz) spinduliuotė (1 THz yra  $10^{12}$  Hz), kuri prasiskverbia per akimi nepermatomas medžiagas be nepageidaujamo poveikio gyviems organizmams.

THz dažniai apima diapazoną nuo 100 GHz iki 10 THz. Tai ypatinga elektromagnetinio spektro vieta – tarp mikrobangų ir infraraudonųjų spindulių – kurioje prietaisų kūrimui reikia sujungti gana skirtingas sampratas – klasikinę krūvininkų pernašą ir kvantinę mechaniką. Kita vertus, THz ruožas daugelyje sričių atvėrė daugybę pritaikymo galimybių – be saugumo [3–5] ir medicinos [6–8] taikymų, THz ruožą galima taikyti pramonės tikslams [12], plačiajuosčio ryšio sistemoms [13,14], radarams [15,16], cheminių junginių [17] bei bakterijų atpažinimui [18], skirtingų supakuotų medžiagų išskyrimui [19,20] ir kokybės kontrolei [21].

Viena svarbiausių THz technologijos vystymo sričių gali būti laikoma THz vaizdų fiksavimas (arba vaizdinimas), kuris yra labai veiksmingas įrankis saugumui ir medicinai. Nuo pirmojo proveržio su B. B. Hu ir M. Nuss [22] darbu THz vaizdų fiksavimas buvo ženkliai patobulintas technologiškai [9,23,24], taip pat išvystyti aktyvūs ir pasyvūs komponentai bei išplėstas taikymų spektras.

Svarbu paminėti dvi THz vaizdų fiksavimo taikomųjų tyrimų kryptis.

Pirmoji apima inovacijų ir taikymų vystymą bei demonstravimą mokslinėse laboratorijose; antroji nagrinėja taikymus realiomis veikimo sąlygomis už laboratorijos ribų. Pirmu atveju optinių elementų dydis, jų derinimas ir net veikimo temperatūros palaikymas yra savaime suprantami, o realiomis sąlygomis veikiančiose sistemose komponentų derinimo neturi reikėti, sistemos dydis privalo būti minimalus, jos turi veikti plačiame temperatūrų režyme. Taigi, matmenų mažinimas ir orientavimasis į vienlusčius (*angl. on-chip*) sprendimus emisijai ir pluošto formavimui bei detekcijai ir optinei sąsajai lieka vieni pagrindinių uždavinių sistemų taikymams. Todėl THz vaizdų fiksavimo sprendimai puslaidininkių pagrindu ir jų matmenų mažinimas naudojant difrakcinės optikos komponentus vietoje įprastų masyvių parabolinių veidrodžių yra vieni pagrindinių uždavinių taikymams už laboratorijų ribų [25,26].

Šis darbas ir skiriamas kompaktiškų THz vaizdų fiksavimo sistemų kūrimui naudojant optinio pluošto valdymo principus, kurie leistų priartinti jas prie įdiegimo esant tikros aplinkos sąlygoms. Pirmiausiai THz pluošto valdymui mes naudojome homodininę detekcijos schemą su fazės keitimu efektyviems, prieinamiems ir tuo pačiu nesudėtingai įgyvendinamiems sprendimams, patikimam homodiniam THz vaizdų fiksavimui; antra, naudodami difrakcinės optikos komponentus pagamintus iš aukštos varžos silicio kaip THz pluošto valdymo įrankius mes parodėme, jog jie yra tinkami THz vaizdų fiksavimo sistemų matmenų mažinimui išlaikant galimybę išskirti mažai spinduliuotę sugeriančius objektus sudėtus į pakuotes, atitinkančias įprastų pašto siuntinių dydį.

## 13.2 Darbo tikslas

Pagrindinis disertacijos tikslas yra kompaktinių spektroskopinių terahercinių vaizdų fiksavimo sistemų vystymas, charakterizavimas ir panaudojimas, įdiegiant optinių pluoštų inžinerijos principus.

Tikslas yra dvilypis.

Pirma, sukurti ir charakterizuoti patikimą kompaktišką THz homodininę vaizdų fiksavimo schemą siekiant rasti sprendimus, kurie būtų našūs ir būtų prieinamos kainos.

Antra, taikant THz pluošto valdymo įrankius – silicio difrakcinės optikos komponentus – sukurti ir charakterizuoti kompaktišką THz vaizdų fiksavimo sistemą, leidžiančią atskleisti ir išskirti silpnai THz spinduliuotę sugeriančius objektus pakuotėse.

Tikslas gali būti skaidomas į toliau išvardintus uždavinius.

### 13.3 Darbo uždaviniai

1. Sukurti prieinamą našią kompaktišką THz homodininę vaizdinimo sistemą naudojant patikimus peteliškės tipo diodus ir ją palyginti su alternatyvia heterodinine THz vaizdų fiksavimo technika mažai spinduliuotę sugeriančių objektų aptikimui.
2. Ištirti ir charakterizuoti sistemos veikimą 0,3 THz ir 0,6 THz dažniuose, nustatyti signalo-triukšmo santykius bei dinaminį diapazoną; apsvastyti prieinamus našius sprendimus fazės postūmiui.
3. Ištirti molekulių pluoštelių epitaksinio auginimo sąlygų poveikį InGaAs/InP sluoksniams, skirtiems „peteliškės“ tipo diodų gamybai, ir nustatyti optimalų auginimo režimą atsižvelgiant į InGaAs diodų parametrus.
4. Suprojektuoti, pagaminti ir ištirti silicio difrakcine optika paremtus bifokalinius THz lęšius.
5. Panaudoti sukurtą silicio bifokalinį THz lęšį THz vaizdų fiksavimui, pademonstruoti vienalaikį kelių židinių THz vaizdų fiksavimą, charakterizuoti ir įvertinti sukurtos THz vaizdų fiksavimo sistemos pagrindinius parametrus.
6. Sukurti difrakcinius THz lęšius, skirtus Beselio THz vaizdų fiksavimui su iki 20 mm išplėstu židinio gyliu, tinkamą pašto siuntose esančių objektų vaizdų fiksavimui.
7. Pademonstruoti tik silicio optiką naudojančią Beselio THz vaizdų fiksavimą; nustatyti signalo-triukšmo santykius bei dinaminį diapazoną; įvertinti prieinamus našius sprendimus kontrasto gerinimui bei palyginti su įprastiniu THz vaizdų fiksavimu.
8. Valdyti THz pluoštą naudojant erdvinio filtravimo metodus ir tai pritaikyti THz vaizdinimui; atskleisti pranašumus lyginant su kitais pluoštų valdymo metodais; nustatyti detektorių parametrus reikalingus tokio tipo THz vaizdų fiksavimui.

### 13.4 Darbo naujumas

Mokslinis darbo naujumas remiasi šiais pagrindiniais teiginiais:

1. Pademonstruotas THz homodininis ir tiesioginis vaizdų fiksavimas, skirtas išskirti mažai spinduliuotę sugeriančias medžiagas supakuotas tarp iki šešių medvilninio audinio sluoksnių panaudojant InGaAs

- peteliškės tipo diodus kaip detektorius. Aptartos ir palygintos veikimo savybės ir užfiksuotų vaizdų parametrai tiek tiesioginei, tiek homodininei schemai.
2. Homodininė fazės postūmio schema buvo įgyvendinta nesudėtingu būdu keičiant įprasto biuro popieriaus lapų kiekį optiniame kelyje. Parodyta, kad homodininis THz vaizdų fiksavimas gali būti naudojamas kaip patogus vaizdų fiksavimo būdas įtartinų žemo kontrasto objektų paslėptų tekstilėje aptikimui.
  3. Iširtos ir aptartos skirtingos technologinės sąlygos InGaAs diodams, pagamintiems iš InGaAs sluoksnių, užaugintų molekulinį pluoštelių epitaksija (*angl. molecular beam epitaxy, MBE*) ant pusiau izoliuojančio InP padėklo. Parodyta, kad struktūrose pastebimas stiprus vidinis elektrinis laukas siekiantis iki 49 kV/cm, kuris buvo nustatytas iš fotoatspindžio spektrų.
  4. Parodyta, kad įtampos fliktuacijų spektrinis tankis InGaAs dioduose kambario temperatūroje yra proporcingas  $1/f$ , o žemesnėse – 77–200 K – temperatūrose vyrauja Lorenciano tipo spektras dėl atsitiktinių telegrafo signalų, sukeltų pavienių pagavos defektų.
  5. Gauti rezultatai atskleidė InGaAs sluoksnių, užaugintų skirtingais pluoštelių slėgių (*angl. beam equivalent pressure, BEP*) In/Ga santykiais, įtaką žemo dažnio triukšmo lygiui ir THz detektorių jautriui. Nustatyta, kad THz detektoriai, užauginti su BEP In/Ga santykiu, lygiu 2.06, yra geriausiai tinkantys kambario temperatūroje veikiančių jautrių InGaAs peteliškės tipo diodų gamybai.
  6. Parodyta, kad kompaktiška Fibonači (bifokalinė) terahercinių vaizdų fiksavimo sistema gali būti įgyvendinta naudojant monochromatinius THz šaltinius su difrakciniais silicio lęšiais. Fokusavimo savybės buvo įvertinti tiek teoriškai, tiek eksperimentiškai išmatavus erdvinius profilius, atstumus tarp židinio taškų ir židinio gylio 0,3 THz ir 0,6 THz dažniuose.
  7. Vienalaikis dviejų plokštumų, atskirtų 7 mm atstumu, vaizdų fiksavimas su bangos ilgio raiška buvo parodytas eksperimentiškai 0,3 THz ir 0,6 THz dažniuose. Vaizdų fiksavimas keliuose židinio taškuose buvo palygintas su tokio paties diametro ir pagamintos iš tos pačios medžiagos fazinės zoninės plokštelės veikimu.
  8. Plonos ir kompaktiškos Beselio zoninės plokštelės, pagrįstos silicio daugialygės difrakcine optika, buvo suprojektuotos, pagamintos ir pademonstruotos THz pralaidumo vaizdų fiksavimo sistemoje.



9. Pasiūlytas naujoviškas kompaktiškesnis eksperimentinis stendas panaudojus dvi Beselio zonines plokšteles su pagerintomis THz vaizdų fiksavimo galimybėmis. Diskretiniai aksikonai (*angl. axicons*) su 4 fazės kvantavimo lygiais buvo pagaminti iš aukštos varžos silicio naudojant lazerinės abliacijos technologiją (*angl. laser ablation technology*) leido praplėsti židinio gylį iki 20 mm su minimaliais optiniais nuostoliais ir išvengti stambių parabolinių veidrodžių naudojimo vaizdų užrašymo stende.
10. Kompaktiška THz vaizdinimo sistema suteikė galimybę tirti storesnius nei 10 mm objektus su pagerintu kontrastu, silpna priklausomybe nuo bandinio storio ir padėties dėl ilgo židinio gylio ir ženkliai pagerinta raiška pritaikius dekonvoliucijos algoritmus.
11. Erdvinio filtravimo metodai – fazės kontrasto ir tamsaus lauko metodai– gali būti pritaikyti plačios apertūros THz vaizdinimui, kur galima išskirti mažai sugeriančius objektus subTHz ruože naudojant jautrius kambario temperatūroje detektorius, pavyzdžiui, iš titano pagamintus mikrobolometrus. Užfiksuoti mažai sugeriančių objektų vaizdai nefokusuotoje 0,3 THz dažnio šviesoje naudojant apskritimo formos popieriaus lapelius kaip filtrą fazės kontrasto ir apskritimo formos aliuminio folijos filtrą tamsaus lauko eksperimentuose.

## 13.5 Ginamieji teiginiai

1. Homodininis terahercinių vaizdų fiksavimas gali būti pritaikytas mažos sugerties objektams atpažinti 0,3 THz ir 0,6 THz dažniuose naudojant kambario temperatūros InGaAs „peteliškės“ tipo diodus kaip patikimus detektorius ir fazės kontrolei keičiant popieriaus lapų skaičių.
2. InGaAs sluoksniai užauginti molekuline epitaksija su pluoštelių slėgių In/Ga santykiu lygiu 2.06 yra tinkamiausi kambario temperatūros peteliškės tipo THz detektorių gamybai su jautriu 10 V/W diapazone ir triukšmų ekvivalenčia galia (*angl. noise equivalent power, NEP*) žemesne nei  $1 \text{ nW}/\sqrt{\text{Hz}}$  prie 0,6 THz dažnio dėl stipraus vidinio elektrinio lauko efektų.
3. Kompaktiška bifokalinių terahercinių vaizdų fiksavimo sistema gali būti įgyvendinta naudojant monochromatinį THz šviesos šaltinį ir fazinę silicio zoninę plokštelę Fibonači sekos pagrindu.
4. Beselio THz vaizdų fiksavimas gali būti įgyvendintas kompaktiškoje THz vaizdų fiksavimo schemoje naudojant tik aukštos varžos silicio

pagrindo optinius lęšius, kurie įgalina storų objektų THz vaizdų fiksavimą 1 cm židinio gylio diapazone subTHz dažniuose.

5. Erdvinio filtravimo metodai – fazės kontrastas ir tamsus laukas – gali būti pritaikyti plačios apertūros THz vaizdinimui silpnai sugeriantiems objektams subTHz ruože išskirti.

## 13.6 Autoriaus indėlis

Autorius dalyvavo homodino [P1], Fibonači bifokalinio [P3], Beselio zoninių plokštelių [P4] ir erdvinio filtravimo metodų [P5] eksperimentuose: stendų projektavime, difrakcinių elementų, skirtų optinių pluoštų valdymui, projektavime ir modeliavime; bandinių, skirtų THz vaizdų fiksavimui, projektavime ir gamyboje siekiant pademonstruoti naujoviškų metodų privalumus; THz vaizdų užrašyme ir tolesniame apdorojime bei gautų duomenų analizėje. Autorius taip pat dalyvavo THz dalyje tyrimo, aprašomo InGaAs „peteliškės“ tipo diodinių detektorių publikacijoje [P2], kur analizavo duomenis.

Jis taip pat patobulino bei sukūrė naujus programinius įrankius duomenų surinkimui ir apdorojimui. Autorius prisidėjo prie mokslinių straipsnių ir medžiagos konferencijoms ruošimo.

## 13.7 Rezultatų apžvalga

Koherentinis heterodininis THz vaizdų fiksavimas [66] leidžia atpažinti mažos sugerties medžiagas, bet šis metodas reikalauja dviejų THz šaltinių susietomis fazėmis, o tai sistemą daro sudėtinga ir sunkiai pritaikoma praktikoje. Reikalingas naujas THz vaizdų fiksavimo sprendimas, kuris galėtų būti konkurencingas praktiniuose taikymuose. Siekiant išvengti dviejų THz šaltinių būtinybės, tiesioginio pralaidumo vaizdų fiksavimo stendas buvo pakeistas THz pluoštą išskaidant į dvi šakas, kurios interferavo „peteliškės“ tipo detektoriuje [68]. Taip vaizdų fiksavimo sistema buvo pakeista iš tiesioginės į homodininę. Skirtingas skaičius biuro popieriaus lapų buvo įterptas į vieną iš optinių šakų, siekiant pakeisti optinio kelio ilgį nekeičiant optinių elementų padėties. Naudodami kambario temperatūros InGaAs „peteliškės“ tipo diodus ir 0,3 THz bei 0,6 THz šaltinius parodėme, jog homodininis režimas leido pasiekti dviem eilėmis aukštesnį dinaminį diapazoną lyginant su tiesioginiu režimu. Pademonstruoti homodininio THz vaizdų fiksavimo tinkamumui plonų mažai sugeriančių objektams indentifikuoti buvo pagamintas bandinys iš užspaudžiamo mažo tankio polietileno (LDPE) maišelio, popierinės nosinės, poodinės adatos ir nitrilinės pirštinės tarp 2

medvilninio audinio sluoksnių. Užfiksuotame homodininiame vaizde matėsi tiek LDPE maišelis, tiek popierinė nosinė.

InGaAs „peteliškės“ tipo diodai, skirti THz ruožui, yra puikiai tinkantys kompaktiškų THz vaizdų fiksavimo sistemoms [68, 69]. Siekiant optimizuoti diodų dizainus jautriai plačiajuoste THz detekcijai reikėjo ištirti InGaAs sluoksnių auginimo sąlygų įtaką ir defektų vaidmenį prietaisų veikimui. Atlikome detalų fotoatspindžio ir InGaAs peteliškės tipo diodų jautrio 0,3 THz ir 0,6 THz dažnio spinduliuotei matavimus. Iš fotoatspindžio matavimų pagrindu gautų Franco–Keldyšo osciliacijų (FKO) analizės galima spręsti apie vidinį elektrinį lauką bandiniuose. Nustatėme, kad molekulių pluoštelių slėgių InGa santykiu 2,06 epitaksiškai užaugintas detektorius turėjo 49 kV/cm vidinį elektrinį lauką, kuris atitinkamai turėjo 10 V/W siekiantį jautrį, kuris rodo, kad „peteliškės“ tipo gerai diodai tinka THz detektorių, veikiančių kambario temperatūroje, gamybai.

Siekiant sujungti kompaktinės difrakcinės optikos ir tomografinio vaizdų fiksavimo privalumus galima naudoti difrakcinius lęšius su Fibonači sekos elementais bei vieno dažnio THz šaltiniu kitaip nei anksčiau parodytas tomografinis vaizdų fiksavimas keičiant šaltinio dažnį [97]. Fibonačio, arba, bifokalinis, THz vaizdų fiksavimas eksperimentiškai pademonstruotas panaudojant difrakcinį lęšį nuolatinės veikos režimu. Mes parodome silicio Fibonačio lęšio dizainą, veikimą ir aukštos raiškos vaizdinimą ties 0,6 THz dažniu. Lęšis buvo pagamintas iš monokristalinio silicio padėklo naudojant lazerinį apdirbimo metodą, anksčiau taikytą pagaminti didelio efektyvumo daugiapakopės fazės Frenelio lęšiams [50]. Skirtingų objektų, sudėtų į specialiai paruoštą laikiklį, 0,6 THz dažnio THz vaizdai buvo užfiksuoti tuo pačiu metu skirtingose plokštumose. Naudojant skyros taikinį buvo įvertinta erdvinė skyra, kuri buvo bangos ilgio eilės. Daugiafokusinis Fibonačio lęšio taikymas vaizdų fiksavimui palygintas su įprastos silicio fazinės plokštelės veikimu. Erdvinių profilių ir fokusavimo gylio savybės išnagrinėtos keičiant šaltinio dažnį nuo 0,3 THz iki 0,6 THz.

Beselio terahercinis vaizdų fiksavimas buvo pritaikytas panaudojus du plonus silicio daugiapakopės fazės optinius elementus nuolatinės veikos režimu 0,6 THz dažniu. Pasiūlytas Beselio zoninės plokštelės dizainas – diskretinis 4 fazės kvantizavimo aksikonas – pagamintas lazeriu abliuojant aukštos varžos silicį, leido išplėsti židinio gylį iki 20 mm patiriant nedidelius optinius nuostolius ir išvengiant stambių parabolinių veidrodžių panaudojimo vaizdo fiksavimo stende. Kompaktiška THz vaizdų fiksavimo sistema leido išskirti storesnius nei 10 mm objektus, o pritaikyti dekonvoliucijos algoritmai pakėlė kontrastą ir pagerino raišką iki 0,6 bangos ilgio.

THz pluošto formavimas naudojant erdvinio filtravimo metodus buvo

pademonstruotas siekiant pritaikyti THz vaizdinimo sistemą veikimui su detektorių matricomis, kurios galėtų būti naudingos ateityje atsiradus prieinamiems didelės galios THz šaltiniams. Eksperimentus atlikome naudodami 0,3 THz dažnio spinduliuotę ir titano pagrindo mikrobolometrus kaip detektorius su dviem erdvinių filtrų tipais: filtras Nr. 1, pagamintas iš 4 lapų 2 mm diametro apskritimo formos popieriaus, buvo fazinis filtras, įvedęs  $\pi/2$  fazės vėlinimą tik centrinėje Furje spektro dalyje taip sukurdamas vaizdą fazės kontrasto metodu; antrasis, filtras Nr. 2, 2 mm diametro apskritimo formos aliuminio folija, veikė kaip amplitudinis filtras ir blokavo žemus erdvinius dažnius taip sukurdamas tamsaus lauko vaizdą, kuriame išryškėjo dalis objektų.

## 13.8 Diskusija ir išvados

1. Parodyta, kad homodininė fazės postūmio schema gali būti įgyvendinta nesudėtingu būdu keičiant biuro popieriaus lapų kiekį optiniame kelyje. Nustatyta, jog homodininis THz vaizdų fiksavimas gali tarnauti kaip patogus įrankis aptikti tekstilėje paslėptus įtartinus žemo kontrasto objektus.
2. Įvertintos skirtingos technologinės sąlygos InGaAs diodams, pagamintiems iš InGaAs sluoksnių užaugintų molekuline pluoštelių epitaksija (MBE) ant pusiau izoliuojančio InP padėklo. Parodyta, kad struktūros pasižymi stipriu vidiniu elektriniu lauku, siekiančiu 49 kV/cm, kuris buvo įvertintas iš fotoatspindžio spektrų.
3. Parodyta, kad įtampos svyravimų spektrinis tankis InGaAs dioduose kambario temperatūroje yra proporcingas  $1/f$ , o žemesnėje, 77–200 K, temperatūroje vyrauja Lorenciano tipo spektras dėl atsitiktinių telegrafo signalų, sukeltų atskirų pagavos defektų.
4. Nustatyta InGaAs sluoksnių auginimo skirtingais pluoštelių slėgių (BEP) In/Ga santykiais įtaka žemo dažnio triukšmo lygiui ir THz detektorių jautriui. Parodyta, jog InGaAs "peteliškės" tipo diodai užauginti su BEP In/Ga santykiu lygiu 2,06 yra tinkamiausi gamybai jautrių kambario temperatūroje veikiančių THz detektorių, kurių jautris siekė 10 V/W ir ekvivalenti triukšmo galia buvo žemesnė nei 1 nW/ $\sqrt{\text{Hz}}$  ties 0,6 THz dažniu.
5. Parodyta, kad kompaktiškas bifokalinis Fibonači terahercinis vaizdų fiksavimas gali būti įgyvendintas naudojant monochromatinius THz šviesos šaltinius ir difrakcinius silicio lęšius. Silicio zoninių plokštelių

fokusavimas buvo ištirtas tiek teoriškai, tiek eksperimentiškai išmatavus erdvinius profilius, atstumą tarp židinių ir židinio gylį ties 0,3 THz ir 0,6 THz dažniais. Gauti rezultatai buvo palyginti su daugiapakope zonavine Frenelio plokštele.

6. Buvo parodytas vienalaikis dviejų plokštumų, atskirtų per 7 mm atstumą, vaizdų fiksavimas su bangos ilgio skyra 0,6 THz dažnyje. Keleto židinių vaizdų fiksavimo rezultatas buvo palygintas su tokios pačios medžiagos ir diametro fazinės zonavinės plokštelės veikimu.
7. Plonos ir kompaktiškos Beselio zonavinės plokštelės, paremtos daugiafazine difrakcine optika, buvo suprojektuotos, pagamintos ir pademonstruotos THz vaizdų fiksavimo sistemoje pralaidumo geometrije.
8. Pasiūlytas naujoviškas eksperimentinis stendas, naudojantis dvi Beselio zonavines plokšteles pagerintam storų bandinių vaizdų fiksavimui ir mažesniems sistemos matmenims pasiekti. Diskretiniai aksionai, turintys 4 fazės kvantizavimo lygius, buvo pagaminti iš aukšos varžos silicio naudojant lazerinės abliacijos technologiją ir leido išplėsti fokusavimo gylį iki 20 mm su minimaliais optiniais nuostoliais bei išvengti stambiųjų parabolinių veidrodžių naudojimo THz vaizdų fiksavimo stende.
9. Kompaktiška THz vaizdų fiksavimo sistema suteikė galimybę tirti storesnius nei 10 mm objektus su geresniu kontrastu, silpna priklausomybe nuo bandinio storio ir pozicijos dėl ilgo židinio gylio, o dekonvoliucijos algoritmai leido ženkliai pagerinti vaizdo raišką.
10. Erdvinio filtravimo metodai – fazės kontrastas ir tamsusis laukas – gali būti taikomi plačios apertūros THz vaizdinimui, leidžiančiam išskirti mažai sugeriančius objektus subTHz ruože, naudojant jautrius kambario temperatūroje detektorius, pvz., iš titano pagamintus mikrobolometrus. Mažai sugeriančių objektų vaizdai buvo užfiksuoti naudojant nefokusuotą 0,3 THz šviesą su apskritimo formos popieriaus lapeliais kaip filtrais fazės kontrastui ir apskritimo formos aliuminio folija tamsaus lauko eksperimentams.

## 13.9 Padėka šeimai

Dėkoju mamai *Zitai*, tėčiui *Jonui*, broliui *Robertui*, brolienei *Daliai*, močiutei *Joanai* ir nuostabiausiai žmonai *Jurgai* už nuolatinį palaikymą.

## REFERENCES

- [1] M. S. Linet, K. P. Kim, D. L. Miller, R. A. Kleinerman, S. L. Simon, and A. B. De Gonzalez, "Historical review of occupational exposures and cancer risks in medical radiation workers," *Radiation Research*, vol. 174, no. 6 B, pp. 793–808, 2010.
- [2] E. J. Hall and D. J. Brenner, "Cancer risks from diagnostic radiology," *British Journal of Radiology*, vol. 81, no. 965, pp. 362–378, 2008.
- [3] M. Kowalski, N. Palka, M. Piszczek, and M. Szustakowski, "Hidden object detection system based on fusion of THz and VIS images," *Acta Physica Polonica A*, vol. 124, no. 3, pp. 490–493, 2013.
- [4] N. Palka and M. Szala, "Transmission and Reflection Terahertz Spectroscopy of Insensitive Melt-Cast High-Explosive Materials," *Journal of Infrared, Millimeter, and Terahertz Waves*, vol. 37, no. 10, pp. 977–992, 2016.
- [5] U. Puc, A. Abina, M. Rutar, A. Zidanšek, A. Jeglič, and G. Valušis, "Terahertz spectroscopic identification of explosive and drug simulants concealed by various hiding techniques," *Applied Optics*, vol. 54, no. 14, p. 4495, 2015.
- [6] F. Wahaia, I. Kasalynas, D. Seliuta, G. Molis, A. Urbanowicz, C. D. Carvalho Silva, F. Carneiro, G. Valusis, and P. L. Granja, "Study of paraffin-embedded colon cancer tissue using terahertz spectroscopy," *Journal of Molecular Structure*, vol. 1079, pp. 448–453, jan 2015.
- [7] Q. Sun, Y. He, K. Liu, S. Fan, E. P. J. Parrott, and E. Pickwell-MacPherson, "Recent advances in terahertz technology for biomedical applications," *Quantitative Imaging in Medicine and Surgery*, vol. 7, pp. 345–355, jun 2017.
- [8] I. Kašalynas, R. Venckevičius, L. Minkevičius, A. Sešek, F. Wahaia, V. Tamosiūnas, B. Voisiat, D. Seliuta, G. Valušis, A. Švigelj, and J. Trontelj, "Spectroscopic Terahertz Imaging at Room Temperature Employing Microbolometer Terahertz Sensors and Its Application to the Study of Carcinoma Tissues," *Sensors*, vol. 16, p. 432, mar 2016.

- [9] P. U. Jepsen, D. G. Cooke, and M. Koch, "Terahertz spectroscopy and imaging - Modern techniques and applications," *Laser and Photonics Reviews*, vol. 5, no. 1, pp. 124–166, 2011.
- [10] T. Nagatsuma, "Terahertz technologies: Present and future," *IEICE Electronics Express*, vol. 8, no. 14, pp. 1127–1142, 2011.
- [11] A. Abina, U. Puc, A. Jeglič, J. Prah, R. Venckevičius, I. Kašalynas, G. Valušis, and A. Zidanšek, "Qualitative and quantitative analysis of calcium-based microfillers using terahertz spectroscopy and imaging," *Talanta*, vol. 143, pp. 169–177, oct 2015.
- [12] S. R. Tripathi, Y. Sugiyama, K. Murate, K. Imayama, and K. Kawase, "Terahertz wave three-dimensional computed tomography based on injection-seeded terahertz wave parametric emitter and detector," *Optics Express*, vol. 24, no. 6, p. 6433, 2016.
- [13] N. Oshima, K. Hashimoto, S. Suzuki, and M. Asada, "Wireless data transmission of 34 Gbit/s at a 500-GHz range using resonant-tunnelling-diode terahertz oscillator," *Electronics Letters*, vol. 52, pp. 1897–1898, oct 2016.
- [14] X. Yu, T. Miyamoto, K. Obata, Y. Hosoda, J.-Y. Kim, M. Fujita, and T. Nagatsuma, "Direct Terahertz Communications with Wireless and Fiber Links," in *2019 44th International Conference on Infrared, Millimeter, and Terahertz Waves (IRMMW-THz)*, vol. 2019-Septe, pp. 1–2, IEEE, sep 2019.
- [15] Z. Zhou, Z. Cao, and Y. Pi, "Dynamic Gesture Recognition with a Terahertz Radar Based on Range Profile Sequences and Doppler Signatures," *Sensors*, vol. 18, p. 10, dec 2017.
- [16] S. Gui, J. Li, and Y. Pi, "Security Imaging for Multi-Target Screening Based on Adaptive Scene Segmentation With Terahertz Radar," *IEEE Sensors Journal*, vol. 19, pp. 2675–2684, apr 2019.
- [17] S. J. Oh, J. Choi, I. Maeng, J. Y. Park, K. Lee, Y.-M. Huh, J.-S. Suh, S. Haam, and J.-H. Son, "Molecular imaging with terahertz waves," *Optics Express*, vol. 19, p. 4009, feb 2011.
- [18] X. Yang, D. Wei, S. Yan, Y. Liu, S. Yu, M. Zhang, Z. Yang, X. Zhu, Q. Huang, H.-L. Cui, and W. Fu, "Rapid and label-free detection and assessment of bacteria by terahertz time-domain spectroscopy," *Journal of Biophotonics*, vol. 9, pp. 1050–1058, oct 2016.
- [19] M. Kowalski, "Hidden Object Detection and Recognition in Passive Terahertz and Mid-wavelength Infrared," *Journal of Infrared, Millimeter, and Terahertz Waves*, vol. 40, pp. 1074–1091, dec 2019.

- [20] L. Valzania, P. Zolliker, and E. Hack, "Coherent reconstruction of a textile and a hidden object with terahertz radiation," *Optica*, vol. 6, p. 518, apr 2019.
- [21] M. Dohi, W. Momose, H. Yoshino, Y. Hara, K. Yamashita, T. Hakomori, S. Sato, and K. Terada, "Application of terahertz pulse imaging as PAT tool for non-destructive evaluation of film-coated tablets under different manufacturing conditions," *Journal of Pharmaceutical and Biomedical Analysis*, vol. 119, pp. 104–113, feb 2016.
- [22] B. B. Hu and M. C. Nuss, "Imaging with terahertz waves," *Optics Letters*, vol. 20, p. 1716, aug 1995.
- [23] M. Tonouchi, "Cutting-edge terahertz technology," *Nature Photonics*, vol. 1, pp. 97–105, feb 2007.
- [24] D. M. Mittleman, "Twenty years of terahertz imaging," *Optics Express*, vol. 26, p. 9417, apr 2018.
- [25] G. Valušis, R. Venckevičius, L. Minkevicius, A. Reklaitis, V. Tamošiūnas, I. Kašalynas, B. Voisiat, D. Seliuta, G. Račiukaitis, and D. Jokubauskis, "Compact solutions for spectroscopic solid-state-based terahertz imaging systems," *Terahertz Emitters, Receivers, and Applications VIII*, no. August 2017, p. 27, 2017.
- [26] S. S. Dhillon, M. S. Vitiello, E. H. Linfield, A. G. Davies, M. C. Hoffmann, J. Booske, C. Paoloni, M. Gensch, P. Weightman, G. P. Williams, E. Castro-Camus, D. R. S. Cumming, F. Simoens, I. Escorcía-Carranza, J. Grant, S. Lucyszyn, M. Kuwata-Gonokami, K. Konishi, M. Koch, C. A. Schmuttenmaer, T. L. Cocker, R. Huber, A. G. Markelz, Z. D. Taylor, V. P. Wallace, J. Axel Zeitler, J. Sibik, T. M. Korter, B. Ellison, S. Rea, P. Goldsmith, K. B. Cooper, R. Appleby, D. Pardo, P. G. Huggard, V. Krozer, H. Shams, M. Fice, C. Renaud, A. Seeds, A. Stöhr, M. Naftaly, N. Ridler, R. Clarke, J. E. Cunningham, and M. B. Johnston, "The 2017 terahertz science and technology roadmap," *Journal of Physics D: Applied Physics*, vol. 50, no. 4, p. 043001, 2017.
- [27] A. Khalid, N. J. Pilgrim, G. M. Dunn, M. C. Holland, C. R. Stanley, I. G. Thayne, and D. R. S. Cumming, "A Planar Gunn Diode Operating Above 100 GHz," *IEEE Electron Device Letters*, vol. 28, pp. 849–851, oct 2007.
- [28] B. Pradarutti, R. Müller, W. Freese, G. Matthäus, S. Riehemann, G. Notni, S. Nolte, and A. Tünnermann, "Terahertz line detection by a microlens array coupled photoconductive antenna array," *Optics Express*, vol. 16, no. 22, p. 18443, 2008.



- [29] S.-P. Han, H. Ko, J.-W. Park, N. Kim, Y.-J. Yoon, J.-H. Shin, D. Y. Kim, D. H. Lee, and K. H. Park, "InGaAs Schottky barrier diode array detector for a real-time compact terahertz line scanner," *Optics Express*, vol. 21, no. 22, p. 25874, 2013.
- [30] T. V. Kononenko, B. A. Knyazev, D. N. Sovyk, V. S. Pavelyev, M. S. Komlenok, G. A. Komandin, and V. I. Konov, "Silicon kinoform cylindrical lens with low surface roughness for high-power terahertz radiation," *Optics & Laser Technology*, vol. 123, p. 105953, mar 2020.
- [31] G. C. Trichopoulos, H. L. Mosbacker, D. Burdette, and K. Sertel, "A broadband focal plane array camera for real-time thz imaging applications," *IEEE Transactions on Antennas and Propagation*, vol. 61, no. 4, pp. 1733–1740, 2013.
- [32] H. Oulachgar, J. E. Paultre, M. Terroux, F. Provençal, B. Fisette, H. Spisser, F. Berthiaume, A. Paquet, M. Doucet, M. Jacob, L. Marchese, F. Genereux, P. Grenier, C. Alain, and A. Bergeron, "Fabrication and Characterization of Frequency Selective Terahertz Focal Plane Array and Camera," *International Conference on Infrared, Millimeter, and Terahertz Waves, IRMMW-THz*, vol. 2019-September, pp. 5–6, 2019.
- [33] D. Dufour, L. Marchese, M. Terroux, H. Oulachgar, F. Généreux, M. Doucet, L. Mercier, B. Tremblay, C. Alain, P. Beaupré, N. Blanchard, M. Bolduc, C. Chevalier, D. D'Amato, Y. Desroches, F. Duchesne, L. Gagnon, S. Ilias, H. Jerominek, F. Lagacé, J. Lambert, F. Lamontagne, L. Le Noc, A. Martel, O. Pancrati, J.-E. Paultre, T. Pope, F. Provençal, P. Topart, C. Vachon, S. Verreault, and A. Bergeron, "Review of terahertz technology development at INO," *Journal of Infrared, Millimeter, and Terahertz Waves*, vol. 36, no. 10, pp. 922–946, 2015.
- [34] J. Zdanevičius, M. Bauer, S. Boppel, V. Palenskis, A. Lisauskas, V. Krozer, and H. G. Roskos, "Camera for High-Speed THz Imaging," *Journal of Infrared, Millimeter, and Terahertz Waves*, vol. 36, no. 10, pp. 986–997, 2015.
- [35] N. Oda, S. Kurashina, M. Miyoshi, K. Doi, T. Ishi, T. Sudou, T. Morimoto, H. Goto, and T. Sasaki, "Microbolometer Terahertz Focal Plane Array and Camera with Improved Sensitivity in the Sub-Terahertz Region," *Journal of Infrared, Millimeter, and Terahertz Waves*, vol. 36, no. 10, pp. 947–960, 2015.
- [36] T. Vasile, V. Damian, D. Coltuc, and M. Petrovici, "Single pixel sensing for THz laser beam profiler based on Hadamard Transform," *Optics and Laser Technology*, vol. 79, pp. 173–178, 2016.

- [37] S. A. N. Saqueb and K. Sertel, "Multisensor Compressive Sensing for High Frame-Rate Imaging System in the THz Band," *IEEE Transactions on Terahertz Science and Technology*, vol. 9, no. 5, pp. 520–523, 2019.
- [38] A. Heidari and D. Saeedkia, "A 2D camera design with a single-pixel detector," *34th International Conference on Infrared, Millimeter, and Terahertz Waves, IRMMW-THz 2009*, pp. 5–6, 2009.
- [39] R. I. Stantchev, X. Yu, T. Blu, and E. Pickwell-MacPherson, "Real-time terahertz imaging with a single-pixel detector," *Nature Communications*, vol. 11, no. 1, pp. 1–8, 2020.
- [40] J. Hesler, "Summary of Solid-State Sources," 2015. Summary of Solid-State Sources, <https://www.vadiodes.com/images/AppNotes/ApplicationNote-SummaryofSolid-StateSources.pdf>, 2015, accessed 2020-07-31.
- [41] C. Brückner, G. Notni, and A. Tünnermann, "Optimal arrangement of 90° off-axis parabolic mirrors in THz setups," *Optik*, vol. 121, pp. 113–119, jan 2010.
- [42] B. Scherger, M. Scheller, C. Jansen, M. Koch, and K. Wiesauer, "Terahertz lenses made by compression molding of micropowders," *Applied Optics*, vol. 50, p. 2256, may 2011.
- [43] N. Kocic, M. Wichmann, T. Hochrein, P. Heidemeyer, K. Kretschmer, I. Radovanovic, A. S. Mondol, M. Koch, and M. Bastian, "Lenses for terahertz applications: Development of new materials and production processes," *AIP Conference Proceedings*, vol. 1593, no. February 2015, pp. 416–419, 2014.
- [44] Y. H. Lo and R. Leonhardt, "Aspheric lenses for terahertz imaging," *Optics Express*, vol. 16, p. 15991, sep 2008.
- [45] H. Yuan, A. Lisauskas, M. Zhang, A. Rennings, D. Erni, and H. G. Roskos, "Dynamic-range Enhancement of Heterodyne THz Imaging by the Use of a Soft Paraffin-wax Substrate Lens on the Detector," in *2019 Photonics & Electromagnetics Research Symposium - Fall (PIERS - Fall)*, pp. 2607–2611, IEEE, dec 2019.
- [46] S. F. Busch, M. Weidenbach, M. Fey, F. Schäfer, T. Probst, and M. Koch, "Optical Properties of 3D Printable Plastics in the THz Regime and their Application for 3D Printed THz Optics," *Journal of Infrared, Millimeter, and Terahertz Waves*, vol. 35, pp. 993–997, dec 2014.

- [47] B. Zhang, W. Chen, Y. Wu, K. Ding, and R. Li, "Review of 3D Printed Millimeter-Wave and Terahertz Passive Devices," *International Journal of Antennas and Propagation*, vol. 2017, pp. 1–10, 2017.
- [48] A. Siemion, "Terahertz Diffractive Optics—Smart Control over Radiation," *Journal of Infrared, Millimeter, and Terahertz Waves*, vol. 40, no. 5, pp. 477–499, 2019.
- [49] L. Minkevičius, K. Madeikis, B. Voisiat, I. Kašalynas, R. Venckevičius, G. Račiukaitis, V. Tamošiūnas, and G. Valušis, "Focusing Performance of Terahertz Zone Plates with Integrated Cross-shape Apertures," *Journal of Infrared, Millimeter, and Terahertz Waves*, vol. 35, pp. 699–702, sep 2014.
- [50] L. Minkevičius, S. Indrišiūnas, R. Šniaukas, B. Voisiat, V. Janonis, V. Tamošiūnas, I. Kašalynas, G. Račiukaitis, and G. Valušis, "Terahertz multi-level phase Fresnel lenses fabricated by laser patterning of silicon," *Optics Letters*, vol. 42, p. 1875, may 2017.
- [51] W. D. Furlan, G. Saavedra, and J. A. Monsoriu, "White-light imaging with fractal zone plates," *Optics Letters*, vol. 32, no. 15, pp. 2109–2111, 2007.
- [52] R. Ivaškevičiūtė-Povilauskienė, L. Minkevičius, D. Jokubauskis, A. Urbanowicz, S. Indrišiūnas, and G. Valušis, "Flexible materials for terahertz optics: advantages of graphite-based structures," *Optical Materials Express*, vol. 9, p. 4438, nov 2019.
- [53] M. Perenzoni and D. J. Paul, eds., *Physics and Applications of Terahertz Radiation*, vol. 173 of *Springer Series in Optical Sciences*. Dordrecht: Springer Netherlands, 2014.
- [54] R. Han, Y. Zhang, Y. Kim, D. Y. Kim, H. Shichijo, E. Afshari, and K. K. O, "Active Terahertz Imaging Using Schottky Diodes in CMOS: Array and 860-GHz Pixel," *IEEE Journal of Solid-State Circuits*, vol. 48, pp. 2296–2308, oct 2013.
- [55] Y. Nemirovsky, A. Svetlitza, I. Brouk, and S. Stolyarova, "Nanometric CMOS-SOI-NEMS transistor for uncooled THz sensing," *IEEE Transactions on Electron Devices*, vol. 60, no. 5, pp. 1575–1583, 2013.
- [56] W. Knap, Y. Deng, S. Rumyantsev, and M. S. Shur, "Resonant detection of subterahertz and terahertz radiation by plasma waves in submicron field-effect transistors," *Applied Physics Letters*, vol. 81, pp. 4637–4639, dec 2002.

- [57] A. El Fatimy, F. Teppe, N. Dyakonova, W. Knap, D. Seliuta, G. Valušis, A. Shchepetov, Y. Roelens, S. Bollaert, A. Cappy, and S. Rumyantsev, "Resonant and voltage-tunable terahertz detection in InGaAs/InP nanometer transistors," *Applied Physics Letters*, vol. 89, no. 13, pp. 1–4, 2006.
- [58] W. Knap, M. Dyakonov, D. Coquillat, F. Teppe, N. Dyakonova, J. Łusakowski, K. Karpierz, M. Sakowicz, G. Valusis, D. Seliuta, I. Kasalynas, A. Fatimy, Y. M. Meziani, and T. Otsuji, "Field Effect Transistors for Terahertz Detection: Physics and First Imaging Applications," *Journal of Infrared, Millimeter, and Terahertz Waves*, pp. 1319–1337, aug 2009.
- [59] S. Boppel, A. Lisauskas, A. Max, V. Krozer, and H. G. Roskos, "CMOS detector arrays in a virtual 10-kilopixel camera for coherent terahertz real-time imaging," *Optics Letters*, vol. 37, no. 4, p. 536, 2012.
- [60] A. Lisauskas, S. Boppel, J. Matukas, V. Palenskis, L. Minkevičius, G. Valušis, P. Haring-Bolívar, and H. G. Roskos, "Terahertz responsivity and low-frequency noise in biased silicon field-effect transistors," *Applied Physics Letters*, vol. 102, p. 153505, apr 2013.
- [61] A. Sešek, I. Kašalynas, A. Žemva, and J. Trontelj, "Antenna-coupled Ti-microbolometers for High-sensitivity Terahertz Imaging," *Sensors and Actuators A: Physical*, vol. 268, pp. 133–140, dec 2017.
- [62] A. Sužiedelis, J. Gradauskas, S. Ašmontas, G. Valušis, and H. G. Roskos, "Giga- and terahertz frequency band detector based on an asymmetrically necked n-n+-GaAs planar structure," *Journal of Applied Physics*, vol. 93, pp. 3034–3038, mar 2003.
- [63] D. Seliuta, E. Širmulis, V. Tamošiūnas, S. Balakauskas, S. Ašmontas, A. Sužiedelis, J. Gradauskas, G. Valušis, A. Lisauskas, H. Roskos, and K. Köhler, "Detection of terahertz/sub-terahertz radiation by asymmetrically-shaped 2DEG layers," *Electronics Letters*, vol. 40, no. 10, p. 631, 2004.
- [64] D. Seliuta, I. Kašalynas, V. Tamošiūnas, S. Balakauskas, Z. Martūnas, S. Ašmontas, G. Valušis, A. Lisauskas, H. Roskos, and K. Köhler, "Silicon lens-coupled bow-tie InGaAs-based broadband terahertz sensor operating at room temperature," *Electronics Letters*, vol. 42, no. 14, p. 825, 2006.
- [65] I. Kašalynas, D. Seliuta, R. Simniškis, V. Tamošiūnas, K. Köhler, and G. Valušis, "Terahertz imaging with bow-tie InGaAs-based diode with broken symmetry," *Electronics Letters*, vol. 45, no. 16, p. 833, 2009.

- [66] L. Minkevičius, V. Tamošiūnas, I. Kašalynas, D. Seliuta, G. Valušis, A. Lisauskas, S. Boppel, H. G. Roskos, and K. Köhler, "Terahertz heterodyne imaging with InGaAs-based bow-tie diodes," *Applied Physics Letters*, vol. 99, no. 13, pp. 1–3, 2011.
- [67] L. Minkevičius, V. Tamošiūnas, M. Kojelis, E. Žąsinas, V. Bukauskas, A. Šetkus, R. Butkutė, I. Kašalynas, and G. Valušis, "Influence of Field Effects on the Performance of InGaAs-Based Terahertz Radiation Detectors," *Journal of Infrared, Millimeter, and Terahertz Waves*, vol. 38, pp. 689–707, jun 2017.
- [68] I. Kašalynas, R. Venckevičius, D. Seliuta, I. Grigelionis, and G. Valušis, "InGaAs-based bow-tie diode for spectroscopic terahertz imaging," *Journal of Applied Physics*, vol. 110, p. 114505, dec 2011.
- [69] I. Kašalynas, R. Venckevičius, and G. Valušis, "Continuous Wave Spectroscopic Terahertz Imaging With InGaAs Bow-Tie Diodes at Room Temperature," *IEEE Sensors Journal*, vol. 13, pp. 50–54, jan 2013.
- [70] J. Trontelj, G. Valušis, R. Venckevičius, I. Kašalynas, A. Sešek, and A. Švigelj, "A high performance room temperature THz sensor," *Terahertz Emitters, Receivers, and Applications V*, vol. 9199, p. 91990K, 2014.
- [71] A. Taflove and S. C. Hagness, *Computational Electrodynamics: The Finite-Difference Time-Domain Method*. Norwood, Massachusetts, United States: Artech House, 2nd ed., 2000.
- [72] D. Glaab, S. Boppel, A. Lisauskas, U. Pfeiffer, E. Öjefors, and H. G. Roskos, "Terahertz heterodyne detection with silicon field-effect transistors," *Applied Physics Letters*, vol. 96, p. 042106, jan 2010.
- [73] X. Wang, L. Hou, and Y. Zhang, "Continuous-wave terahertz interferometry with multiwavelength phase unwrapping," *Applied optics*, vol. 49, no. 27, pp. 5095–5102, 2010.
- [74] E. Ojefors, U. R. Pfeiffer, A. Lisauskas, and H. G. Roskos, "A 0.65 THz Focal-Plane Array in a Quarter-Micron CMOS Process Technology," *IEEE Journal of Solid-State Circuits*, vol. 44, pp. 1968–1976, jul 2009.
- [75] A. Lisauskas, D. Glaab, H. G. Roskos, E. Ojefors, and U. R. Pfeiffer, "Terahertz imaging with Si MOSFET focal-plane arrays," *Terahertz Technology and Applications II*, vol. 7215, p. 72150J, 2009.
- [76] A. Lisauskas, M. Bauer, S. Boppel, M. Mundt, B. Khamaisi, E. Socher, R. Venckevičius, L. Minkevičius, I. Kašalynas, D. Seliuta, G. Valušis, V. Krozer, and H. G. Roskos, "Exploration of Terahertz Imaging with

- Silicon MOSFETs," *Journal of Infrared, Millimeter, and Terahertz Waves*, vol. 35, pp. 63–80, jan 2014.
- [77] A. Lisauskas, U. Pfeiffer, E. Öjefors, P. H. Bolvar, D. Glaab, and H. G. Roskos, "Rational design of high-responsivity detectors of terahertz radiation based on distributed self-mixing in silicon field-effect transistors," *Journal of Applied Physics*, vol. 105, no. 11, pp. 1–7, 2009.
- [78] A. Lisauskas, W. von Spiegel, S. Boubanga-Tombet, A. El Fatimy, D. Coquillat, F. Teppe, N. Dyakonova, W. Knap, and H. Roskos, "Terahertz imaging with GaAs field-effect transistors," *Electronics Letters*, vol. 44, no. 6, p. 408, 2008.
- [79] B. K. Jones, *Electrical Noise as a Measure of Quality and Reliability in Electronic Devices*, vol. 87. Academic Press, 1993.
- [80] B. Jones, "Electrical noise as a reliability indicator in electronic devices and components," *IEE Proceedings - Circuits, Devices and Systems*, vol. 149, pp. 13–22, feb 2002.
- [81] S. Pralgauskaite, V. Palenskis, J. Matukas, B. Šaulys, V. Kornijčuk, and V. Verdingovas, "Analysis of mode-hopping effect in Fabry-Pérot multiple-quantum well laser diodes via low frequency noise investigation," *Solid-State Electronics*, vol. 79, pp. 104–110, 2013.
- [82] L. K. Vandamme, "Noise as a Diagnostic Tool for Quality and Reliability of Electronic Devices," *IEEE Transactions on Electron Devices*, vol. 41, no. 11, pp. 2176–2187, 1994.
- [83] L. K. Vandamme and F. N. Hooge, "What do we certainly know about  $1/f$  noise in MOSTs?," *IEEE Transactions on Electron Devices*, vol. 55, no. 11, pp. 3070–3085, 2008.
- [84] R. S. Duran, G. L. Larkins, C. M. Van Vliet, and H. Morkoç, "Generation-recombination noise in gallium nitride-based quantum well structures," *Journal of Applied Physics*, vol. 93, no. 9, pp. 5337–5345, 2003.
- [85] J. Dobbert, L. Tran, F. Hatami, W. T. Masselink, V. P. Kunets, and G. J. Salamo, "Low frequency noise in InSb/GaAs and InSb/Si channels," *Applied Physics Letters*, vol. 97, no. 10, pp. 2–4, 2010.
- [86] H. Rao and G. Bosman, "Device reliability study of high gate electric field effects in AlGaIn/GaN high electron mobility transistors using low frequency noise spectroscopy," *Journal of Applied Physics*, vol. 108, no. 5, pp. 5–9, 2010.

- [87] J. D. Chisum, E. N. Grossman, and Z. Popovi, "A general approach to low noise readout of terahertz imaging arrays," *Review of Scientific Instruments*, vol. 82, no. 6, pp. 1–8, 2011.
- [88] L. Minkevičius, M. Ragauskas, J. Matukas, V. Palenskis, S. Pralgauskaite, D. Seliuta, I. Kašalynas, and G. Valušis, "InGaAs bow-tie diodes for terahertz imaging: low frequency noise characterisation," in *Terahertz Emitters, Receivers, and Applications III* (M. Razeghi, A. N. Baranov, H. O. Everitt, J. M. Zavada, and T. Manzur, eds.), vol. 8496, p. 849612, oct 2012.
- [89] L. Minkevičius, *Terahertz imaging arrays for room temperature operation*. PhD thesis, Vilnius University, Center for Physical Sciences and Technology (FTMC), 2016.
- [90] B. Čechavičius, J. Kavaliauskas, G. Krivaitė, G. Valušis, D. Seliuta, M. P. Halsall, and P. Harrison, "Photo- and electro-reflectance spectroscopy of  $\delta$ -doped GaAs/AlAs multiple quantum well structures," *physica status solidi (a)*, vol. 204, pp. 412–421, feb 2007.
- [91] V. Jakštas, *Compact terahertz emitters and detectors based on AlGaIn/GaN heterostructures*. PhD thesis, Vilnius University, Center for Physical Sciences and Technology (FTMC), 2018.
- [92] A. El Fatimy, S. Boubanga Tombet, F. Teppe, W. Knap, D. Veksler, S. Rumyantsev, M. Shur, N. Pala, R. Gaska, Q. Fareed, X. Hu, D. Seliuta, G. Valušis, C. Gaquiere, D. Theron, and A. Cappy, "Terahertz detection by GaN/AlGaIn transistors," *Electronics Letters*, vol. 42, no. 23, p. 1342, 2006.
- [93] K. Ikamas, A. Lisauskas, M. Bauer, A. Ramer, S. Massabeau, D. Cibiraite, M. Burakevic, S. Chevtchenko, J. Mangeney, W. Heinrich, V. Krozery, and H. G. Roskosy, "Efficient detection of short-pulse THz radiation with field effect transistors," in *2017 International Conference on Noise and Fluctuations (ICNF)*, pp. 1–4, IEEE, jun 2017.
- [94] Q. Y. Lu, S. Slivken, N. Bandyopadhyay, Y. Bai, and M. Razeghi, "Widely tunable room temperature semiconductor terahertz source," *Applied Physics Letters*, vol. 105, p. 201102, nov 2014.
- [95] J. Zdanevicius, H.-W. Hubers, H. G. Roskos, D. Cibiraite, K. Ikamas, M. Bauer, J. Matukas, A. Lisauskas, H. Richter, T. Hagelschuer, and V. Krozer, "Field-Effect Transistor Based Detectors for Power Monitoring of THz Quantum Cascade Lasers," *IEEE Transactions on Terahertz Science and Technology*, vol. 8, pp. 613–621, nov 2018.

- [96] K. Ikamas, D. Cibiraite, A. Lisauskas, M. Bauer, V. Krozer, and H. G. Roskos, "Broadband Terahertz Power Detectors Based on 90-nm Silicon CMOS Transistors With Flat Responsivity Up to 2.2 THz," *IEEE Electron Device Letters*, vol. 39, pp. 1413–1416, sep 2018.
- [97] S. Wang, B. Ferguson, D. Abbott, and X. C. Zhang, "T-ray imaging and tomography," *Journal of Biological Physics*, vol. 29, no. 2-3, pp. 247–256, 2003.
- [98] A. Krotkus, K. Bertulis, R. Adomavičius, V. Pačebutas, and A. Geižutis, "Semiconductor materials for ultrafast optoelectronic applications," *Lithuanian Journal of Physics*, vol. 49, no. 4, pp. 359–372, 2009.
- [99] W. D. Furlan, V. Ferrando, J. A. Monsoriu, P. Zagrajek, E. Czerwińska, and M. Szustakowski, "3D printed diffractive terahertz lenses," *Optics Letters*, vol. 41, p. 1748, apr 2016.
- [100] J. A. Monsoriu, A. Calatayud, L. Remon, W. D. Furlan, G. Saavedra, and P. Andres, "Bifocal Fibonacci Diffractive Lenses," *IEEE Photonics Journal*, vol. 5, pp. 3400106–3400106, jun 2013.
- [101] E. Maciá, "Exploiting aperiodic designs in nanophotonic devices," *Reports on Progress in Physics*, vol. 75, p. 036502, mar 2012.
- [102] H. T. Dai, Y. J. Liu, and X. W. Sun, "The focusing property of the spiral Fibonacci zone plate," in *Optical Components and Materials IX* (S. Jiang, M. J. F. Digonnet, and J. C. Dries, eds.), vol. 8257, p. 82570T, feb 2012.
- [103] Y. Yu and W. Dou, "Generation of pseudo-Bessel beams at THz frequencies by use of binary axicons.," *Optics express*, vol. 17, no. 2, pp. 888–93, 2009.
- [104] X. Yu, M. Zhang, and S. Lei, "Multiphoton polymerization using femtosecond bessel beam for layerless three-dimensional printing," *Journal of Micro and Nano-Manufacturing*, vol. 6, no. 1, 2018.
- [105] L. Gao, L. Shao, B.-C. Chen, and E. Betzig, "3D live fluorescence imaging of cellular dynamics using Bessel beam plane illumination microscopy," *Nature Protocols*, vol. 9, no. 5, pp. 1083–1101, 2014.
- [106] T. A. Planchon, L. Gao, D. E. Milkie, M. W. Davidson, J. A. Galbraith, C. G. Galbraith, and E. Betzig, "Rapid three-dimensional isotropic imaging of living cells using Bessel beam plane illumination," *Nature Methods*, vol. 8, pp. 417–423, may 2011.
- [107] C. Snoeyink, "Imaging performance of Bessel beam microscopy," *Optics Letters*, vol. 38, no. 14, p. 2550, 2013.



- [108] F. Courvoisier, J. Zhang, M. K. Bhuyan, M. Jacquot, and J. M. Dudley, "Applications of femtosecond Bessel beams to laser ablation," *Applied Physics A: Materials Science and Processing*, vol. 112, no. 1, pp. 29–34, 2013.
- [109] M. Duocastella and C. Arnold, "Bessel and annular beams for materials processing," *Laser & Photonics Reviews*, vol. 6, pp. 607–621, sep 2012.
- [110] S. F. Busch, G. E. Town, M. Scheller, and M. Koch, "Focus free terahertz reflection imaging and tomography with Bessel beams," *Journal of Infrared, Millimeter, and Terahertz Waves*, vol. 36, pp. 318–326, mar 2015.
- [111] G. Ok, S. W. Choi, K. H. Park, and H. S. Chun, "Foreign object detection by sub-terahertz quasi-Bessel beam imaging," *Sensors (Basel, Switzerland)*, vol. 13, no. 1, pp. 71–85, 2012.
- [112] X. Wei, C. Liu, L. Niu, Z. Zhang, K. Wang, Z. Yang, and J. Liu, "Generation of arbitrary order Bessel beams via 3D printed axicons at the terahertz frequency range," *Applied Optics*, vol. 54, no. 36, p. 10641, 2015.
- [113] J. H. McLeod, "The Axicon: A New Type of Optical Element," *Journal of the Optical Society of America*, vol. 44, no. 8, p. 592, 1954.
- [114] F. O. Fahrbach and A. Rohrbach, "Propagation stability of self-reconstructing Bessel beams enables contrast-enhanced imaging in thick media," *Nature Communications*, vol. 3, 2012.
- [115] W. Liebl, J. Boeck, K. Aufinger, D. Manger, W. Hartner, B. Heinemann, and R. Lachner, "SiGe Applications in Automotive Radars," *ECS Transactions*, vol. 75, pp. 91–102, sep 2016.
- [116] A. Tomkins, E. Juntunen, A. Poon, H. Golestaneh, H. Shakoor, G. Temkine, G. Nabovati, N. Gilanpour, A. Chen, A. Sargsyan, N. Smith, A. Ali, K. Law, B. Lynch, C. Farnsworth, A. Lau, C. Hansen, N. Costa, A. Rashidian, M. Supinski, and K. Riley, "A 16-Element Phased-Array Transceiver in 130-nm SiGe BiCMOS for Fixed Wireless Access Covering the Full 57-71 GHz Band," in *2020 IEEE Radio and Wireless Symposium (RWS)*, vol. 2020-Janua, pp. 152–155, IEEE, jan 2020.
- [117] P. Chevalier, W. Liebl, H. Rucker, A. Gauthier, D. Manger, B. Heinemann, G. Avenier, and J. Bock, "SiGe BiCMOS Current Status and Future Trends in Europe," *2018 IEEE BiCMOS and Compound Semiconductor Integrated Circuits and Technology Symposium, BCICTS 2018*, pp. 64–71, 2018.
- [118] A. Ali, J. Yun, F. Giannini, H. J. Ng, D. Kissinger, and P. Colantonio, "168-195 GHz Power Amplifier with Output Power Larger Than 18 dBm in BiCMOS Technology," *IEEE Access*, vol. 8, pp. 79299–79309, 2020.

- [119] J. Al-Eryani, H. Knapp, J. Kammerer, K. Aufinger, H. Li, and L. Maurer, "Fully Integrated Single-Chip 305-375-GHz Transceiver With On-Chip Antennas in SiGe BiCMOS," *IEEE Transactions on Terahertz Science and Technology*, vol. 8, no. 3, pp. 329–339, 2018.
- [120] K. Song, J. Kim, D. Kim, J. Yoo, and J. S. Rieh, "A 300-GHz CMOS 7-by-7 Detector Array for Optics-less THz Imaging with Scan-less Target Object," *Journal of Infrared, Millimeter, and Terahertz Waves*, vol. 41, no. 2, pp. 202–214, 2020.
- [121] N. Blanchard, L. Marchese, A. Martel, M. Terroux, É. Savard, C. Chevalier, L. Mercier, L. Gagnon, J. Lambert, M. Bolduc, and A. Bergeron, "Catadioptric optics for high-resolution terahertz imager," *Terahertz Physics, Devices, and Systems VI: Advanced Applications in Industry and Defense*, vol. 8363, no. May 2012, pp. 83630B–83630B–7, 2012.
- [122] T. Pope, M. Doucet, F. Dupont, L. Marchese, B. Tremblay, G. Baldenberger, S. Verrault, and F. Lamontagne, "Uncooled detector, optics, and camera development for THz imaging," *Terahertz Physics, Devices, and Systems III: Advanced Applications in Industry and Defense*, vol. 7311, no. April 2009, p. 73110L, 2009.
- [123] Z. Liu, L. Tian, S. Liu, and L. Waller, "Real-time brightfield, darkfield, and phase contrast imaging in a light-emitting diode array microscope," *Journal of Biomedical Optics*, vol. 19, no. 10, p. 1, 2014.
- [124] C. E. Hall, "Dark-Field Electron Microscopy. I. Studies of Crystalline Substances in Dark-Field," *Journal of Applied Physics*, vol. 19, pp. 198–212, feb 1948.
- [125] M. J. Hargather and G. S. Settles, "Natural-background-oriented schlieren imaging," *Experiments in Fluids*, vol. 48, pp. 59–68, jan 2010.
- [126] F. Zernike and F. J. M. Stratton, "Diffraction Theory of the Knife-Edge Test and its Improved Form, The Phase-Contrast Method," *Monthly Notices of the Royal Astronomical Society*, vol. 94, pp. 377–384, mar 1934.
- [127] F. Zernike, "Diffraction theory of the knife-edge test and its improved form, the phase-contrast method," *Journal of Micro/Nanolithography, MEMS, and MOEMS*, vol. 1, p. 87, jul 2002.

## 14. REPRINTED PUBLICATIONS

1st publication

**Terahertz homodyne spectroscopic imaging of concealed low-absorbing objects**

**D. Jokubauskis**, L. Minkevičius, D. Seliuta, I. Kašalynas and G. Valušis  
*Optical Engineering* 58(02), p. 023104, 2019, DOI: 10.1117/1.OE.58.2.023104

This is an open access article distributed under the Creative Commons Attribution License (CC-BY).

The article may be accessed online at <https://doi.org/10.1117/1.OE.58.2.023104>

# Terahertz homodyne spectroscopic imaging of concealed low-absorbing objects

Domas Jokubauskis,\* Linas Minkevičius, Dalius Seliuta, Irmantas Kašalynas, and Gintaras Valušis  
Center for Physical Sciences and Technology, Optoelectronics Department, Vilnius, Lithuania

**Abstract.** Terahertz (THz) homodyne and direct spectroscopic images of low-absorbing materials packaged between up to six layers of a cotton fabric are recorded at 0.3 and 0.6 THz at room temperature. More than two orders of magnitude higher dynamic range is revealed due to the detection in a homodyne scheme, which is realized using paper sheets as a phase-shifting mechanism. It is demonstrated that the homodyne approach can serve as a convenient imaging tool to identify and resolve objects manifesting low absorbance of THz radiation, such as paper tissue, nitrile, and low-density polyethylene concealed in a textile environment. © 2019 Society of Photo-Optical Instrumentation Engineers (SPIE) [DOI: 10.1117/1.OE.58.2.023104]

**Keywords:** terahertz imaging; homodyne detection; terahertz spectroscopy; low-absorbing objects.

Paper 181280 received Sep. 5, 2018; accepted for publication Jan. 23, 2019; published online Feb. 9, 2019.

## 1 Introduction

Terahertz frequency radiation (THz) has low-absorption in nonconducting materials, such as clothing fabrics or packaging supplies, which allows to serve as a versatile tool to display contents of packaged and concealed objects in various environments.<sup>1,2</sup> However, when the concealed objects themselves exhibit low absorption in THz frequencies, a direct THz imaging approach becomes unsuitable due to a small signal-to-noise ratio. To tackle this problem, a coherent heterodyne THz imaging<sup>3,4</sup> approach can be employed to reduce the noise floor up to four orders of magnitude, thus allowing to resolve low-absorbing materials. Nevertheless, the heterodyne approach requires at least two signal sources synchronized via a phase-locking loop, which currently makes this technique complicated and not very practical in screening applications. A solution is hence needed that would make THz imaging systems competitive in practical implementations.

In this article, a THz homodyne and direct imaging of low-absorbing materials packaged between up to six layers of cotton fabric at 0.3 and 0.6 THz are demonstrated and compared. The homodyne phase-shifting scheme was realized here in a simple way by varying the number of office paper sheets in the optical path. It is shown that homodyne THz imaging can serve as a convenient imaging tool to screen low-contrast suspicious inclusions in textiles.

## 2 Samples and Their Characterization

Two types of samples were selected for the experiments. The first group included reference objects—a steel blade, serving as a reflecting reference, and a 0.6-mm diameter hypodermic needle for the spatial resolution reference. The second group consisted of low-absorbing materials—a sealable low-density polyethylene (LDPE) (two layers of LDPE film) bag, a tissue paper, and a nitrile glove (two layers of nitrile

film), which were enveloped in two or six layers of cotton fabric. All the low-absorbing samples and cotton layers were characterized individually beforehand in the THz range via absorption measurements using frequency domain THz spectrometer Toptica TeraScan 780 (Toptica Photonics Ltd.). Moreover, a refraction index dispersion analysis of a standard office paper sheet (areal density 80 g/m<sup>2</sup>, thickness of 0.1 mm) was performed, which was used here to vary the phase of the THz radiation in one of the arms of the optical set up. These results are plotted in Fig. 1. One can see that a two-layer cotton fabric exhibits the highest absorption of all the tested materials, except for the frequency range below 0.2 THz where the absorption of a nitrile glove is the highest. We also note that cotton and nitrile glove spectral dependences are very similar. Terahertz frequencies of 0.3 and 0.6 THz (highlighted as vertical lines) were employed enabling the use of our electronic sources for THz imaging. Spectra around 0.6 THz (dotted line) display a significant difference (>35%) in absorbance between the cotton, LDPE bag and paper tissue, and a smaller difference (around 15%) between the cotton and the nitrile. The same trend is observed at 0.3 THz (dashed line), which suggests that a simple direct THz imaging setup can be used without resorting to more advanced techniques. However, in order to reliably distinguish the absorption between a cotton fabric and nitrile glove (<10% difference), different means are needed. A THz homodyne scheme is implemented and described in the following that allows for an unambiguous distinction between the materials.

## 3 Experimental Setup and Measurement Technique

Figure 2 presents the THz homodyne imaging implementation scheme.<sup>5</sup> Terahertz radiation was generated by an electronic source based on a frequency-synthesizer whose 12.5-GHz frequency signal was multiplied via a multiplier chain (Virginia Diodes Inc.) by a factor of 24 or 48 to operate at frequencies 0.3 and 0.6 THz, respectively. The THz beam delivered from the source is collimated with an off-axis

\*Address all correspondence to Domas Jokubauskis, E-mail: domas.jokubauskis@ftmc.lt

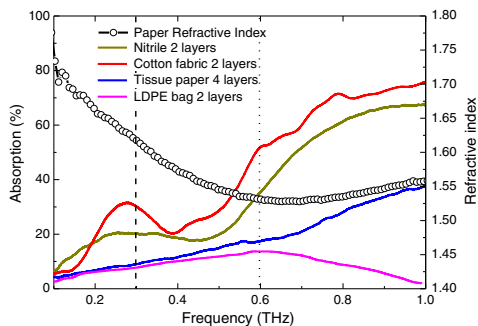


**Fig. 1** Absorption spectra of the studied objects: nitrile glove, cotton fabric, tissue paper, and LDPE bag (left scale). Right scale displays refractive index of the office paper used to shift the phase of the THz radiation in a homodyne scheme. Spectra were measured using frequency domain terahertz spectrometer.

parabolic mirror PM1, then split with a high-resistivity silicon beam splitter (thickness 370  $\mu\text{m}$ ) S1 into two arms: the upper and the lower one with a ratio of 60:40. The phase of the more intensive (upper) beam was varied by a paper stack, P, and delivered using a flat mirror, M1, to another off-axis parabolic mirror, PM2, with a focal length 10 cm to focus the radiation onto the sample. The transmitted radiation is focused with a high-density polyethylene (HDPE) lens, L1 (focal length 5 cm), and through a beam splitter, S2, diverted to the detector for the image formation. The remaining (lower arm) less intense radiation part is directed via a splitter S1, flat mirror M2, an off-axis parabolic mirror PM3, and a beam splitter S2 (splitting ratio 60:40), which was employed to generate a homodyne signal. In the direct-detection mode, only the upper arm was used for imaging, while the lower one was blocked. Intensity of

the THz beam was detected at room temperature using a broadband InGaAs bow-tie diode<sup>6</sup> that is well-suited for the THz direct<sup>7</sup> as well as the multispectral THz imaging aims.<sup>8,9</sup>

The THz source was electronically modulated at 1-kHz frequency. Detected signals were amplified and registered using a lock-in amplifier. Samples were placed on an electronically controlled X – Y stage to implement the raster scanning. Data are recorded and processed via custom-made computer software.<sup>8,9</sup>

The imaging setup was calibrated to determine dynamical range of the homodyne system. The experiment was carried out in both direct and homodyne modes at 0.3 THz frequency by stacking office paper sheets in the upper arm, as shown in Fig. 2 (left panel). The results are depicted in Fig. 2 (right panel). The homodyne detected signal reveals more than two orders of magnitude higher dynamic range in comparison to the direct one at 0.3-THz range, and a factor of 25 improvements at 0.6 THz. Better contrast can thus be expected in the homodyne mode for recording THz images of low-absorbing materials.

#### 4 Homodyne Terahertz Imaging Results

Photos of the packaged objects and their THz images recorded in the direct and homodyne modes are presented in Fig. 3. Direct imaging at 0.6 THz (left panel) clearly reveals packaged highly reflective objects—a steel blade and a needle. The nitrile glove is also resolved here due to its relatively higher absorption (Fig. 1). It is worth noting that the number of packaging cotton fabric layers exhibits no pronounced influence on the quality of the image.

The contrast noticeably changes at 0.3-THz frequency, in particular, the low-absorbing objects—the LDPE bag and the tissue paper, are invisible in the direct detection mode [Fig. 3(d)]. The piece of a nitrile glove still can be identified because of its relatively higher absorption, while only contours of the hypodermic needle can be resolved due to the longer illuminating wavelength. Therefore, a direct THz

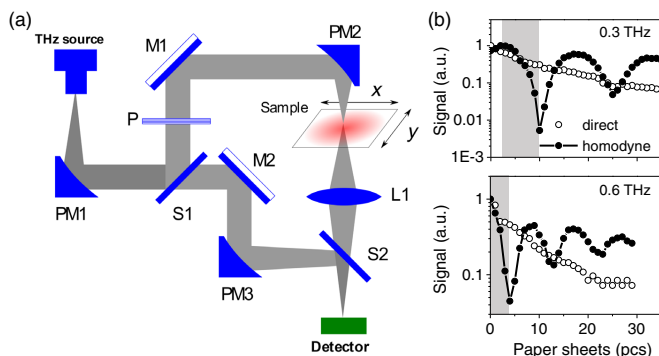


**Fig. 2** (a) Setup for THz imaging in transmission geometry using direct and homodyne modes. Letters S denotes beam splitters, L, lenses; P, paper sheet placement; PM, off-axis parabolic mirrors; and M, flat mirrors. (b) Estimates of the system dynamic range at 0.3- and 0.6-THz frequencies. Normalized detected signal recorded in both, direct and homodyne, schemes is shown as a function of paper sheets pieces, which was used to vary the phase of the radiation. Shaded area indicates the regime of optimal homodyne operation. Note the increase of dynamic range in the homodyne mode.

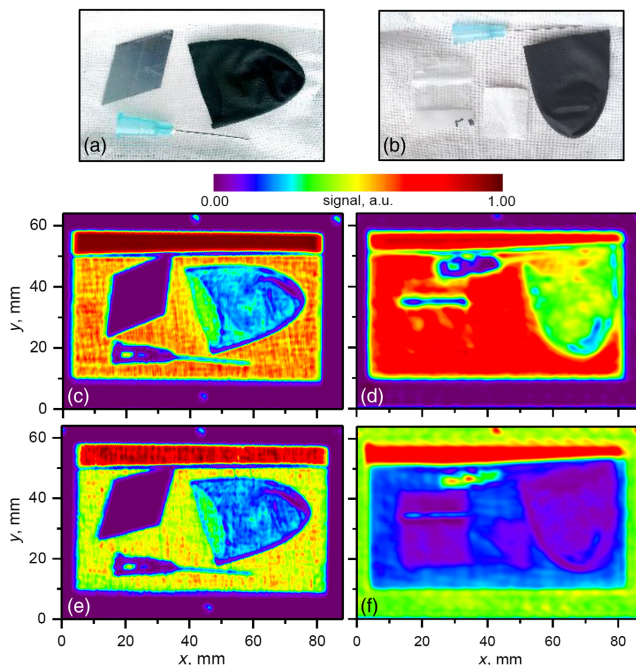


**Fig. 3** Left panel: Photo (a) and direct images at 0.6 THz of steel blade, hypodermic needle, and a piece of nitrile glove enveloped in two and six layers cotton fabric (c) and (e), respectively. Note good contrast despite different cotton fabric layers. Signal-to-noise-ratio (SNR) is 1900 and 700, respectively. Right panel: Photo of the sample (b) and its direct (d) and homodyne (f) image at 0.3 THz. The sample consisted of a sealable LDPE bag, tissue paper, nitrile glove, and hypodermic needle enveloped in two layers of cotton fabric. SNR is 100 and 200, respectively. THz imaging parameters:  $XY$  pixel size— $0.3 \times 0.3$  mm<sup>2</sup>, image size— $299 \times 212$  pixels, integration time—10 ms. About 10 paper sheets were used to manage phase in the homodyne imaging.

imaging is not the optimal technique in this case, and so our homodyne detection scheme was applied. Phase-imaging can offer a higher image contrast for weak-absorption or transparent materials if one compared it with intensity-related imaging; however, the recording setup requires interferometer arrangement to measure the phase-distribution in the sample.<sup>10</sup> As described earlier, office paper sheets are used to vary the needed phase-shift. Taking into account the thickness of one paper sheet and the refractive index of paper ( $\sim 1.62$  at 0.3 THz, Fig. 1), one can estimate that  $2\pi$  phase-shift can be accumulated using 16 pieces of paper.

As can be seen in Fig. 3(f) (right panel), THz homodyne imaging allows to clearly resolve low-absorbing thin materials, such as the LDPE bag and a tissue paper hidden in two layers of cotton fabric. To extend the measurement scale for thicker samples exceeding the illuminating wavelength (1 mm in our case), one needs to overcome the restrictions induced by  $2\pi$  phase-ambiguity. Phase-unwrapping method with a noise-suppression algorithm<sup>11</sup> can be an effective way for data processing allowing for the extension of the operation range to other THz frequencies.

To illustrate the suitability of the homodyne THz imaging for identifying thin, low-absorbing objects, a sample containing different amounts of paper sheets, a piece of sticky tape, LDPE bag, and letters “THZ” written using conventional pencil (graphite) on the sheet of a paper were constructed. The metal washer served as a reference for highly reflecting materials.

Imaging results at 0.6 THz are displayed in Fig. 4. It is seen that homodyne detection, by varying the phase, enables a high contrast and better resolution of low-absorbing materials, and even allows to distinguish pencil-written letters. While images recorded at 0.3 THz (Fig. 5) do not allow for the determination of the letters, the increased contrast, nevertheless, permits clear detection of the low-absorbing objects.

## 5 Conclusion

Homodyne and direct imaging of materials with low-absorption features in the THz range were investigated and compared. The homodyne scheme using paper sheets as the phase-tuning component allowed us to increase the detection dynamic range by more than two orders of

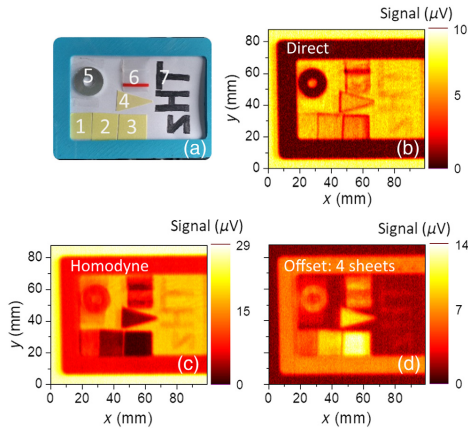


**Fig. 4** (a) Panel—photo of the sample composed of different constituents: numbers 1 to 3 indicate the amount of the paper sheets; 4 is sticky tape; 5 stands for metal washer as the reference; 6 denotes LDPE bag; 7 shows letters “THZ” written using conventional pencil (graphite). Images (b–d) were recorded at 0.6 THz in transmission geometry. Panel (b) presents direct imaging; panels (c, d)—images recorded in homodyne schemes using 0 and 4 sheets of paper for the phase-shifting. Pixel size— $0.3 \times 0.3 \text{ mm}^2$ , image size— $330 \times 293$  pixels, integration time—10 ms.

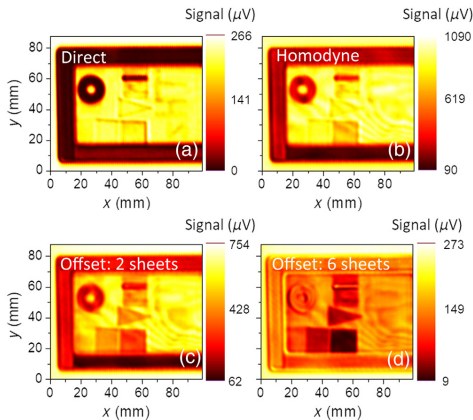


**Fig. 5** Sample as in Fig. 4(a). Images (a–d) were recorded at 0.3 THz in transmission geometry. Panel (a) presents direct imaging; panels (b–d)—images recorded in homodyne schemes using 0, 2, and 6 sheets of paper for the phase-shifting.

magnitude. It was demonstrated that the homodyne THz imaging system at 0.3 and 0.6 THz in transmission geometry enables to detect low-absorbing objects enveloped in up to six layers of cotton fabric. It is illustrated that the homodyne spectroscopic THz imaging can serve as a convenient tool to resolve the concealed objects fabricated from materials manifesting low-THz absorption coefficient.

**Acknowledgments**

Authors kindly thank Rimvydas Venckevičius and Tadas Paulauskas for the kind assistance in the experiments and enlightening discussions. This work was partially supported by the Research Council of Lithuania (Lietuvos Mokslo Taryba, LAT 04/2016). The authors have no relevant financial interests and no other potential conflicts of interest to disclose.

**References**

1. P. U. Jepsen, D. G. Cooke, and M. Koch, “Terahertz spectroscopy and imaging—modern techniques and applications,” *Laser Photonics Rev.* **5**(1), 124–166 (2011).
2. U. Puc et al., “Terahertz spectroscopic identification of explosive and drug simulants concealed by various hiding techniques,” *Appl. Opt.* **54**(14), 4495–4502 (2015).
3. D. Glaab et al., “Terahertz heterodyne detection with silicon field-effect transistors,” *Appl. Phys. Lett.* **96**(4), 042106 (2010).
4. L. Minkevičius et al., “Terahertz heterodyne imaging with InGaAs-based bow-tie diodes,” *Appl. Phys. Lett.* **99**(13), 131101 (2011).
5. I. Kašalynas et al., “Method and device for the spectroscopic imaging of the object,” The State Patent Bureau of the Republic of Lithuania 6297 (2016).
6. D. Seliuta et al., “Silicon lens-coupled bow-tie InGaAs-based broadband terahertz sensor operating at room temperature,” *Electron. Lett.* **42**(14), 825–827 (2006).
7. I. Kašalynas et al., “Terahertz imaging with bow-tie InGaAs-based diode with broken symmetry,” *Electron. Lett.* **45**(16), 833–835 (2009).
8. I. Kašalynas et al., “InGaAs-based bow-tie diode for spectroscopic terahertz imaging,” *J. Appl. Phys.* **110**(11), 114505 (2011).
9. I. Kašalynas et al., “Continuous wave spectroscopic terahertz imaging with InGaAs bow-tie diodes at room temperature,” *IEEE Sens. J.* **13**(1), 50–54 (2013).
10. Y. Wang et al., “Continuous-wave terahertz phase imaging using a far-infrared laser interferometer,” *Appl. Opt.* **50**(35), 6452–6460 (2011).
11. X. Wang, L. Hou, and Y. Zhang, “Continuous-wave terahertz interferometry with multiwavelength phase unwrapping,” *Appl. Opt.* **49**(27), 5095–5102 (2010).

**Domas Jokubauskis** received his BS and MS degrees from the Faculty of Physics, Vilnius University, in 2010 and 2012, respectively. Currently, he is pursuing his PhD in the Department of Optoelectronics, Center for Physical Sciences and Technology. His research interests include THz imaging and digital image processing.

**Linās Minkevičius** graduated from Vilnius University in 2011, magna cum laude diploma and received his doctor’s degree in physics in 2016. Now he is working as a senior researcher in Center for Physical Science and Technology. Field of interest: THz imaging systems, diffractive optics, and detectors for THz range. He has a significant practical experience related with fabrication and processing technologies of GaAs, Si, and hetero-structure semiconductors.

Biographies of the other authors are not available.



2nd publication

**InGaAs Diodes for Terahertz Sensing—Effect of Molecular Beam Epitaxy  
Growth Conditions**




V. Palenskis, L. Minkevičius, J. Matukas, **D. Jokubauskis**, S. Pralgauskaitė, D.  
Seliuta, B. Čechavičius, R. Butkutė and G. Valušis  
*Sensors* **18**(11), p. 3760, 2018.  
DOI: 10.3390/s18113760

This is an open access article distributed under the Creative Commons Attribution  
License (CC-BY).

The article may be accessed online at <https://doi.org/10.3390/s18113760>

Article

# InGaAs Diodes for Terahertz Sensing—Effect of Molecular Beam Epitaxy Growth Conditions

Vilius Palenskis <sup>1</sup>, Linas Minkevičius <sup>2</sup>, Jonas Matukas <sup>1</sup>, Domas Jokubauskis <sup>2,\*</sup> , Sandra Pralgauskaitė <sup>1</sup>, Dalius Seliuta <sup>2</sup>, Bronislovas Čechavičius <sup>2</sup> , Renata Butkutė <sup>2</sup>  and Gintaras Valušis <sup>2</sup>

<sup>1</sup> Institute of Applied Electrodynamics and Telecommunications, Physics Faculty, Vilnius University, Sauletekio ave. 3, 10257 Vilnius, Lithuania; vilius.palenskis@ff.vu.lt (V.P.); jonas.matukas@ff.vu.lt (J.M.); sandra.pralgauskaite@ff.vu.lt (S.P.)

<sup>2</sup> Department of Optoelectronics, Center for Physical Sciences and Technology, Savanoriu ave. 231, 02300 Vilnius, Lithuania; linas.minkevicius@ftmc.lt (L.M.); dalius.seliuta@ftmc.lt (D.S.); bronislovas.cechavicius@ftmc.lt (B.Č.); renata.butkute@ftmc.lt (R.B.); gintaras.valusis@ftmc.lt (G.V.)

\* Correspondence: domas.jokubauskis@ftmc.lt; Tel.: +370-5-2312418

Received: 3 October 2018; Accepted: 30 October 2018; Published: 3 November 2018



**Abstract:** InGaAs-based bow-tie diodes for the terahertz (THz) range are found to be well suited for development of compact THz imaging systems. To further optimize design for sensitive and broadband THz detection, one of the major challenges remains: to understand the noise origin, influence of growth conditions and role of defects for device operation. We present a detailed study of photoreflectance, low-frequency noise characteristics and THz sensitivity of InGaAs bow-tie diodes. The diodes are fabricated from InGaAs wafers grown by molecular beam epitaxy (MBE) on semi-insulating InP substrate under different technological conditions. Photoreflectance spectra indicated the presence of strong built-in electric fields reaching up to 49 kV/cm. It was demonstrated that the spectral density of voltage fluctuations at room temperature was found to be proportional to  $1/f$ , while at lower temperatures, 77–200 K, Lorentzian-type spectra dominate due to random telegraph signals caused by individual capture defects. Furthermore, varying bias voltage, we considered optimal conditions for device room temperature operation in the THz range with respect to signal-to-noise ratio. The THz detectors grown with beam equivalent pressure In/Ga ratio equal to 2.04 exhibit the minimal level of the low-frequency noise, while InGaAs layers grown with beam equivalent pressure In/Ga ratio equal to 2.06 are found to be well suited for fabrication of room temperature bow-tie THz detectors enabling sensitivity of 13 V/W and noise equivalent power (NEP) of 200 pW/√Hz at 0.6 THz due to strong built-in electric field effects.

**Keywords:** terahertz sensing; terahertz imaging; InGaAs diodes; molecular beam epitaxy; low-frequency noise; spectral density

## 1. Introduction

The InGaAs/InP material system is one of the key compounds for ultrafast optoelectronics applications [1]. It can also serve as a core element for other optoelectronics applications including infrared photosensors [2] and magnetic field sensors [3]. A particular importance of this material compound arises from the rapidly growing interests in its suitability for efficient THz emission excited by femtosecond laser pulses [4,5], THz photomixers [6–8], possible use in nanometric field effect transistors for electrically driven plasma-wave-related THz emission [9], and THz sensing [10].

The InGaAs/InP material system is employed in the development of planar bow-tie-shaped InGaAs diodes [11] which were found well-suited for direct [12], heterodyne [13] and spectroscopic

imaging applications up to 2.52 THz [14,15]. The diode operates both due to nonuniform carrier heating and resistive mixing caused by applied external THz electric field inducing DC voltage over the terminals of the diode [16].

The diode exhibits low noise because its operation does not require application of the bias voltage. The choice of the InGaAs material is motivated due to its high electron mobility,  $13,300 \text{ cm}^2/\text{V}\cdot\text{s}$  at room temperature [11]; the detector sensitivity at room temperature is of about  $6 \text{ V}/\text{W}$ , whilst the relevant value in GaAs-based detectors is about  $0.3 \text{ V}/\text{W}$  [17,18]. The noise-equivalent power (NEP) of InGaAs diodes in direct and heterodyne modes is estimated to be about  $4 \text{ nW}/\sqrt{\text{Hz}}$  and  $0.23 \text{ pW}/\text{Hz}$ , respectively, for a local-oscillator power of  $11 \text{ }\mu\text{W}$  [13].

Despite the fact that InGaAs bow-tie diode displays the advantages of broadband room temperature operation, rather uncomplicated fabrication process and good reliability, its NEP values need to be improved in comparison, for instance, to those of field effect transistors fabricated using CMOS technology (gate length is  $150 \text{ nm}$ ), where NEP amounts to  $43 \text{ pW}/\sqrt{\text{Hz}}$  [19]. Therefore, to improve design of InGaAs-based bow-tie THz detectors, one needs to get deeper insight into origin of defects or recombination centers that may have impact on InGaAs layer and InGaAs/InAs/InP material interface properties.

Investigation of noise characteristics is well known as a highly sensitive method to reveal physical processes in various structures and devices as well as to enable the reliability prediction [20–22]. On the other hand, the noise level of a detector is the restricting factor of the imaging system sensitivity [23]. Preliminary investigation has shown that the spectral density of current fluctuations in bow-tie diodes changes with frequency approximately as  $1/f$  and allows us to predict that the origin of noise is a superposition of the capture and emission of charge carriers in defects of the structure [24].

In this article, we discuss effects of different technological conditions for the InGaAs devices fabricated from InGaAs layers grown by molecular beam epitaxy (MBE) on semi-insulating InP substrate. It was shown that structures exhibit presence of strong built-in electric fields reaching up to  $49 \text{ kV}/\text{cm}$ , which were derived from the photoreflectance spectra. It was demonstrated that the spectral density of voltage fluctuations at room temperature is found to be proportional to  $1/f$ , while at lower temperatures,  $77\text{--}200 \text{ K}$ , Lorentzian-type spectra dominate due to random telegraph signals caused by individual capture defects. The presented results demonstrate how InGaAs layers grown at different beam equivalent pressure (BEP) In/Ga ratios affect the low-frequency noise level and the sensitivity of the THz detectors. We underline that THz detectors grown with BEP In/Ga ratio equal to 2.06 are found to be most sensitive at room temperature.

## 2. Grown Structures and Experimental Techniques

The InGaAs layers for detectors were grown using the SVT-A MBE reactor on semi-insulating InP:Fe substrates oriented in the (100) crystallographic plane. Before the growth procedure, the surface of InP:Fe substrate was cleaned from native oxide by annealing at temperature of  $500 \text{ }^\circ\text{C}$  for 10 min. In order to prevent the loss of phosphorus on the surface of the substrate, the deoxidation was performed in flux at a pressure of about  $5 \times 10^{-6} \text{ Torr}$  in-situ observing the reflection high-energy electron diffraction (RHEED) pattern. After the native oxide removal, 1–2 monolayer (ML)-thick InAs was deposited. The thickness of the InAs layer was designed in such a way that it forms a structurally strained interlayer between the substrate and InGaAs. Then, the InGaAs layer was grown in a temperature range from  $500 \text{ }^\circ\text{C}$  to  $515 \text{ }^\circ\text{C}$  varying growth rate from  $300 \text{ nm}/\text{h}$  to  $600 \text{ nm}/\text{h}$ . Growth rate was determined from RHEED intensity oscillations recorded for the specular beam. To optimize the growth conditions, the In/Ga BEP ratio varying from 2.04 to 2.08 was investigated.

The patterning of a  $1.18\text{-}\mu\text{m}$ -height mesa structure was carried out by optical lithography and wet etching [13]. The electrical contacts for detectors were deposited by thermal evaporation of 20-nm-thick Ti and 180-nm-thick Au. Contact layers after deposition were ex-situ annealed at  $400 \text{ }^\circ\text{C}$  temperature for 10 s in nitrogen ambience using a rapid thermal annealing (RTA) oven.

The crystalline structure of In and Ga content in different InGaAs samples has been investigated by measuring high-resolution X-ray diffraction (HRXRD)  $\omega$ - $2\theta$  scans of the (400) reflex using  $\text{CuK}\alpha_1$  radiation. The results of XRD rocking curve measurements are presented in Figure 1. From these data, the lattice constant has been evaluated. The lattice constant varied from 5.8639 Å to 5.8687 Å for InGaAs layers grown using In/Ga ratios from 2.04 to 2.08, respectively, and then the In and Ga content was obtained. It was found that for InGaAs layers well matched to the InP:Fe substrate growth, the BEP ratio of In/Ga of about 2.08 is optimum. The growth mechanism, completion of atomic layers and the surface roughness have been investigated by atomic force microscopy (AFM). The surface images of InGaAs epitaxial layers are shown in Figure 2. AFM revealed that surface roughness of investigated InGaAs layers varied from 0.166 nm (B204) to 0.322 nm (B203). It was demonstrated that lattice matched to the InP substrate epitaxial InGaAs layer exhibits much smoother surface due to the layer-by-layer growth mode.

The photoluminescence (PL) measurements were carried out using the DPSS laser (532 nm) for an excitation with the intensity reaching  $\sim 600 \text{ W/cm}^2$  and the 0.4-m monochromator. The PL was detected using a liquid nitrogen-cooled InGaAs point photodetector, whose signal was recorded using a lock-in amplifier when the laser radiation intensity had been modulated by a mechanical chopper set to 190 Hz modulation frequency.

The photoreflectance (PR) measurements were performed using a DPSS laser (532 nm) with modulation pump source chopped at 190 Hz. The pump beam intensity was kept below  $5 \text{ mW cm}^{-2}$ .

Noise characteristics at forward and backward bias were measured within the frequency range from 10 Hz to 20 kHz varying lattice temperature from 77 K to 300 K. The experimental setup [24] is described in detail in Supplementary Materials.

Terahertz sensitivity was evaluated measuring responsivity of the InGaAs bow-tie detectors at frequency of 0.3 THz and 0.6 THz employing an electronic multiplier chain (Virginia Diodes, Inc. Charlottesville, VA, USA) as THz radiation source.

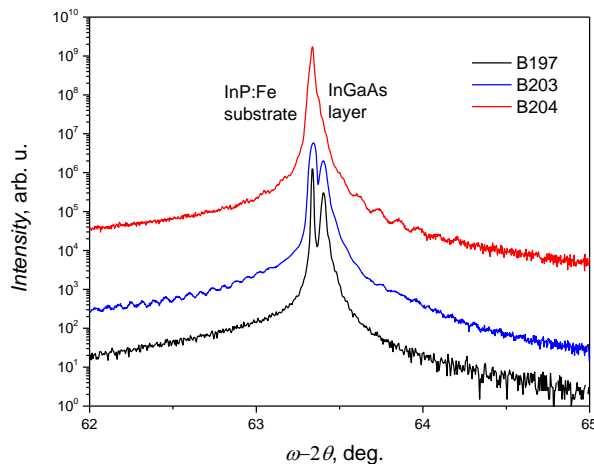


**Figure 1.** The rocking curves of (400) reflex of X-ray diffraction measured for detectors grown with different BEP In/Ga ratios: 2.04 (sample B197), 2.06 (sample B203), and 2.08 (sample B204).

The AFM images (Figure 2) show the surface morphology obtained on GaInAs epitaxial layers, grown using different BEP In/Ga ratios (2.04—B197, 2.06—B203, and 2.08—B204). Scanned surface area is  $1.5 \times 0.7 \mu\text{m}^2$ . The color scale of 4 nm resolution demonstrates surface roughness measured from peak (min) to peak (max). The roughness values measured on the surfaces of B197, B203 and B204 samples are presented in Table 1. The surface morphology of all investigated samples is very smooth and the roughness does not exceed 1 ML. Also, it is clearly seen from the obtained images for B197 and

B203 samples (they are grown at the same temperature of about 500 °C but using different In/Ga ratios) that the atomic traces on the B203 image are wider and exhibit higher quality than B197. On the other hand, the contrast of colors on the B204 sample image is the lowest and shows the highest crystallinity.

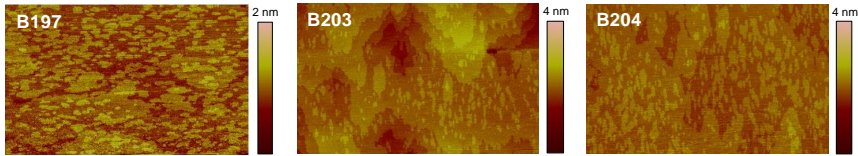


**Figure 2.** The surface morphology images of InGaAs epitaxial layers, grown using different BEP In/Ga ratios (2.04—B197, 2.06—B203, and 2.08—B204), obtained by atomic force microscopy. Scanned area is  $1.5 \times 0.7 \text{ m}^2$ .

**Table 1.** Technological conditions and parameters of characterization of investigated bow-tie detectors: BEP—beam equivalent pressure;  $\Delta 2\theta$ —misalignment between the (400) reflexes of InP substrate and InGaAs epilayer; content of In in percent;  $d$ —thickness of InGaAs, nm;  $rms$ —surface roughness, nm;  $R$ —resistance,  $\Omega$ ;  $E$ —emission energy, eV.

Samples	B197	B203	B204
BEP ratio In/Ga	2.04	2.06	2.08
$\Delta 2\theta$ , deg.	−0.07	−0.064	0
In, %	47.0	52.5	53.2
InGaAs layer thickness, $d$ , nm	540	540	540
$rms$ , nm	0.167	0.322	0.166
$R$ , $\Omega$	470–500	850–900	770–780
$E$ , eV	0.739	0.736	0.735

Figure 3 presents PL spectra measured at room temperature on three 540-nm-thick InGaAs layers grown in varying BEP ratios of In and Ga elements. It is seen that PL peak position is slightly shifted to the lower energies with increase of BEP ratio (In/Ga) from 2.04 to 2.08 (this ratio corresponds to the GaInAs composition lattice-matched to InP substrate). Although the full width at half maximum (FWHM) is less than 50 meV for all three layers, the B204 sample grown at substrate temperature of about 510 °C demonstrates the higher crystalline quality and the narrowest FWHM value ( $\sim 40 \text{ meV}$ ).

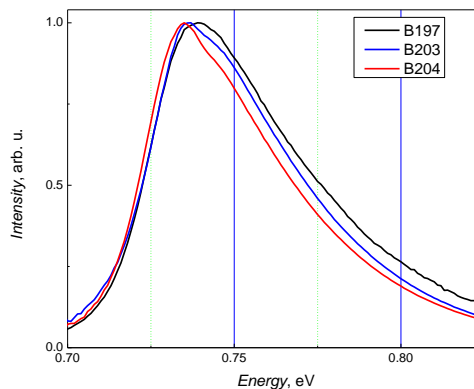


**Figure 3.** Room temperature photoluminescence spectra of three GaInAs samples: sample B197 (black line), B203 (blue line) and B204 (red line) grown using different BEP In/Ga ratios ranging from 2.04, 2.06 and 2.08, respectively, for B197, B203 and B204 at two substrate temperatures of about 500 °C (sample B197 and B203) and 510 °C (sample B204).

Room temperature PR spectra for the epitaxial InGaAs layers are shown in Figure 4. The spectra are dominated by characteristic oscillations. These PR features are associated with Franz–Keldysh oscillations (FKOs) indicating the existence of the internal electric field in the samples. By analysing FKOs above the band edge, it is possible to estimate the strength of the electric field. In the analysis of the electric field strength, the extremes of the FKOs are given by [25]

$$m\pi = \frac{4}{3} \left( \frac{E_m - E_g}{\hbar\theta} \right)^{3/2} + \varphi, \quad (1)$$

where  $m$  is the index of the  $m$ -th extremum,  $E_m$  is the photon energy of the  $m$ -th extremum,  $E_g$  is the band gap of InGaAs,  $\varphi$  is a phase factor. Electro-optic energy  $\hbar\theta$  is given by  $(\hbar\theta)^3 = e^2 F^2 \hbar^2 / 2\mu$ , and depends on electric field  $F$ , and charge carrier reduced mass  $\mu$ . Figure 4b depicts the quantity  $(4/3\pi)(E_m - E_g)^{3/2}$  plotted versus Franz–Keldysh oscillations index  $m$ . As it is seen, the function is linear (solid lines show linear fit to Equation (1)), and from the slope it allows one to evaluate the electro-optic energy, and, hence, to determine the built-in electric field strength in the structure [26]. Evaluation indicates that the strongest electric field—reaching 49 kV/cm—contains the structure B203. Technological characteristics of the investigated samples are summarized in Table 1.

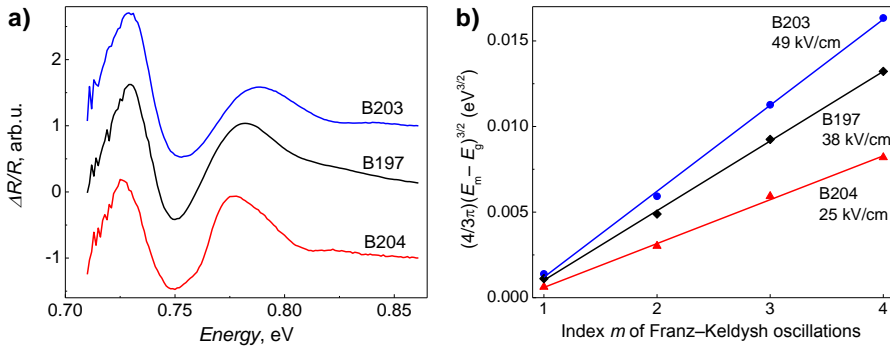


**Figure 4.** Photorefectance spectra of InGaAs layers (a), each spectrum shifted vertically by 1 for clarity; and plots of the quantity  $(4/3\pi)(E_m - E_g)^{3/2}$  versus index  $m$  of Franz–Keldysh oscillations for epitaxial layers (b).

### 3. Low-Frequency Noise Measurement Results and Discussion

#### 3.1. Investigation of the Resistivity of the Detectors

Typical current–voltage characteristics of the investigated bow-tie THz detectors at room temperature are represented in Figure 5, and the dependence of resistance on temperature at low biases is shown in Figure 6. As it is seen from Figure 5, detector’s B197 resistance is smaller than the other detectors at room temperature. Besides, the asymmetry of  $I$ – $U$  characteristics for diode B203 and B204 is higher than those for B197 (Figure 5b). It is worth noting that at temperatures  $T > 200$  K, the resistances slowly decrease with increase in temperature (Figure 6a), while at  $T < 200$  K the resistances increase steeper with the decrease in temperature, especially characteristic for the detector B197. Such resistance changes with temperature can be described in terms of the activation energy (Figure 6b). The decrease of the activation energy  $\Delta E$  with temperature observed for the sample B204 can be explained by the electron hopping mechanism in the impurity band in the energy gap of the semiconductor.

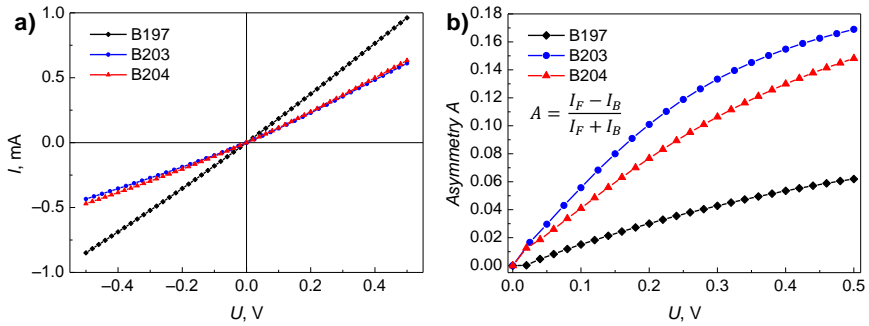


**Figure 5.** The current–voltage characteristics of InGaAs bow-tie detectors at room temperature (298 K) (a) and evaluated asymmetry (b), where  $I_F$  and  $I_B$  are forward and backward current values, respectively, at selected voltages.

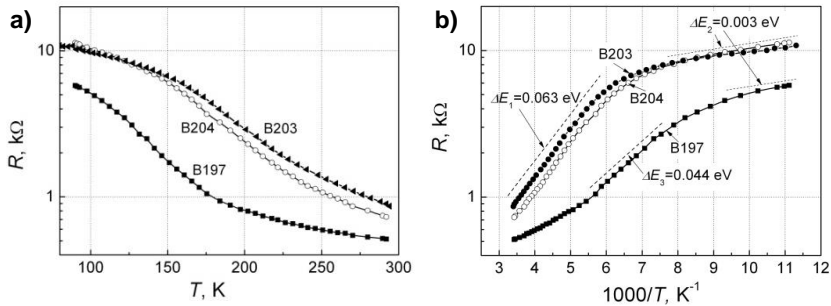


**Figure 6.** Temperature dependences of the resistance of the investigated bow-tie detectors B197, B203 and B204 in the linear part of  $I$ – $V$  characteristics (a). The activated temperature dependences of the resistances of bow-tie detectors as a function of  $1000/T$  (b).

According to the Mott model, the charge carriers are transported via thermally activated tunneling of electrons between the localized states which are randomly distributed in energy and position [27,28]. Then, the electrical conductivity can be described as

$$\sigma \sim \exp\left(-\left(\frac{T_0}{T}\right)^{-\frac{1}{4}}\right), \quad (2)$$

where

$$T_0 = \frac{\lambda\alpha^3}{(N(E_F)k)}, \quad (3)$$

$\lambda$  labels the dimensionless constant,  $\alpha^{-1}$  is the localization length of the wave function for localized states,  $N(E_F)$  denotes the localized state density at the Fermi level, and  $k$  is the Boltzmann's constant.  $T_0$  is the quantity with temperature units, which determines the rate of conductivity change with temperature.

### 3.2. Investigation of the Low-Frequency Noise of the Detectors

Typical low-frequency noise spectra of the investigated InGaAs bow-tie detector B204 at different forward bias at room temperature (298 K) are presented in Figure 7 (the noise spectra for other samples as well as backward current direction at room temperature are almost the same as for the forward current direction, and therefore are not given here). The  $1/f$ -type-voltage noise spectra show that

the observed fluctuations are caused by the superposition of the charge carrier capture and emission processes in defects in the InGaAs layer and its interfaces [29–31].

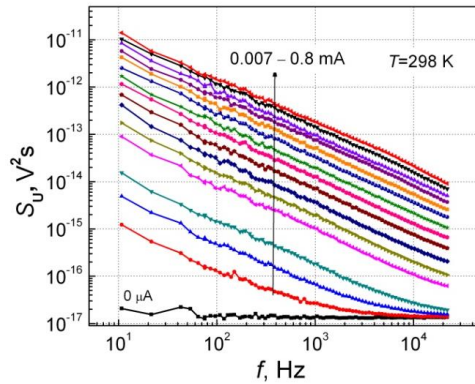


**Figure 7.** Voltage fluctuation spectra at different forward currents at room temperature for sample B204. The dependences for other samples are very similar.

A detailed description of the generation of noise with spectrum  $1/f$ -type is presented in [29,30]. The low-frequency noise level caused by the charge carrier capture in localized states of defects in homogeneous semiconductors can be described as [31]

$$S_U(f)/U^2 = S_R(f)/R^2 = [0.16K(1 + \beta)^2]/(N^2f), \tag{4}$$

where  $S_R(f)$  is power spectral density of the resistance fluctuation  $\Delta R(t)$ ;  $K \geq 1$  is the average number of relaxators (localized capture centers) in the sample with arbitrarily distributed relaxation times in every double octave of relaxation times;  $N$  is the total number of free carriers in the sample; and  $\beta$  is the parameter that describes the contribution of the mobility of the charge carriers' fluctuation to the total resistance fluctuation due to the free charge carrier capture process.

The dependences of the spectral density of voltage fluctuations on forward and backward bias current are shown in Figure 8. From the comparison of Figures 5 and 8, it is seen that in the linear current–voltage characteristics range ( $U < 0.2$  V), the spectral density of voltage fluctuations can be expressed by detector's resistance,  $R$ , and fluctuation spectral density  $S_R(f)$  [18]:

$$S_U(f) = U^2 \frac{S_R(f)}{R^2} = I^2 S_R(f). \tag{5}$$

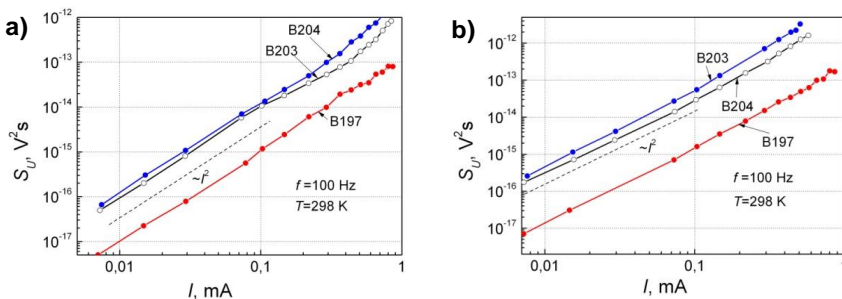


**Figure 8.** Spectral density voltage fluctuation dependence on bias current for forward (a) and backward current directions (b) at room temperature and frequency  $f = 100$  Hz.



The  $1/f$  noise level in the backward current direction is slightly higher than that in the forward one, and this correlates with the fact that the differential resistance in the backward current direction is larger than that in the forward direction. The low-frequency noise level at room temperature for the detector B197 is about an order of magnitude lower than that for other samples, because the differential resistance at room temperature for this detector is also about two-times smaller (Figure 6). This result is related to the smaller In/Ga BEP ratio during growth of sample B197 and its small surface roughness (rms). From the point of view of the low-frequency noise level, the optimal BEP In/Ga ratio is 2.04. According to Equation (4), the parameter  $K$  describing the localized defect density for this sample is about an order of magnitude smaller than that for other diodes.

The low-frequency noise level dependences on temperature at different frequencies for the investigated detectors are presented in Figure 9. The noise peaks appear at particular temperatures due to the random telegraph signals (RTS) observed, when the Fermi energy level coincides with the energy of the defect capture center. The low-frequency noise is consistent with the model of individual fluctuators (capture centers) affecting the resistance locally over a small area, independent of the full area of the device [32]. The power spectrum of the resistance fluctuations due to the defect  $k$  can be written as [32]:

$$S_{Rk}(f) = \frac{4\langle\Delta R_k^2\rangle}{(\langle\tau_e\rangle + \langle\tau_c\rangle) \left[ \left(\frac{1}{\tau_{eff}}\right)^2 + (2\pi f)^2 \right]}, \quad (6)$$

where

$$\frac{1}{\tau_{eff}} = \frac{1}{\langle\tau_e\rangle} + \frac{1}{\langle\tau_c\rangle}; \quad (7)$$

$\langle\tau_e\rangle$  is the average time until the electron is emitted from the  $k$  defect energy level, and  $\langle\tau_c\rangle$  is the average time until the electron is captured by the defect level.

The local resistance fluctuations cause the voltage fluctuations (Figure 9), when the DC current flows through the device, and the spectral density of voltage fluctuations due to all active traps  $N_{tr}$  in the device can be described as

$$S_U = 4I^2 \sum_{k=1}^{N_{tr}} \langle\Delta R_k^2\rangle \frac{\tau_{eff}}{\langle\tau_e\rangle + \langle\tau_c\rangle} \cdot \frac{\tau_{eff}}{1 + (2\pi\tau_{eff})^2}, \quad (8)$$

where the summation is performed over all traps ( $k = 1, 2, \dots, N_{tr}$ ) contained in the InGaAs layers and their interfaces. The relative resistance  $R$  changes  $\Delta R_k/R \sim 1/A$ , where  $A$  is the InAs surface area, and for a constant trap density  $N_{tr} \sim A$ . If the total number of traps  $N_{tr}$  is sufficiently large to ensure the wide distribution of the time constant, and if  $\langle\Delta R_k^2\rangle$  value for every  $k$  defect is about the same order, then one can obtain the  $1/f$ -type noise spectrum.

In the case of dot centers, which have the same energy level, one would expect irregular RTS signals, and the noise spectra with peaks, as it is shown in Figure 9. These noise spectra can be fitted with a few Lorentzian-type spectra (Equation (8)) with a small background of  $1/f$  noise component. The Equation (8) reaches the maximal value when the Fermi level coincides with the defect localization energy in the bandgap. In this case,  $\langle\tau_{ke}\rangle = \langle\tau_{kc}\rangle$ . From these peaks, one can evaluate the effective relaxation times (Equation (7)), and their changes with temperature because every peak fulfils the condition:  $2\pi f_{0k}\tau_{k\,eff} = 1$ .

In order to highlight the effective relaxation time changes, it is convenient to represent the obtained experimental results at different fixed frequencies, as shown in Figure 9. As it is seen from Figure 9a, the noise peak position for the detector B197 is practically independent of temperature. This happens at a specific temperature when the Fermi energy level is located in a continuum of defect energies, which causes a very wide distribution of relaxation times. In the case of the sample B197 (Figure 9a) at temperatures of 127 K, 160 K, 213 K, 234 K and 265 K, the relaxation time distribution ranges exceed

the interval from 15  $\mu$ s to 5 ms. As it is seen, other samples, B203 and B204 (Figure 9b,c), express stronger dependences on temperature in comparison to B197.

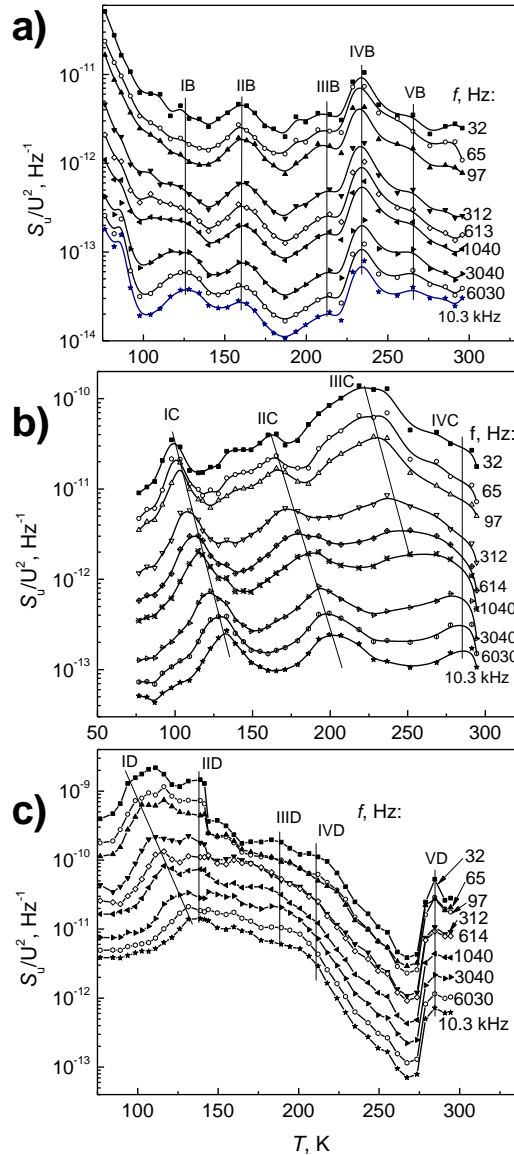


**Figure 9.** The normalized noise level dependences on temperature at different frequencies (a) for detector B197; (b) for B203; (c) for B204. The lines are included as a guide for the eye and illustrate changes of the noise peak groups.

The evaluated relaxation times for every group of peaks of the investigated detectors are shown in Figure 10.

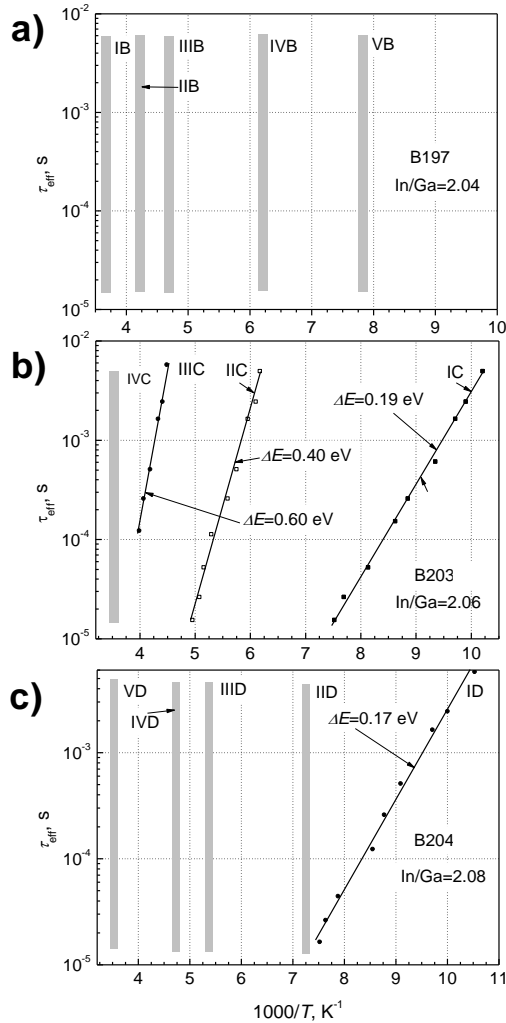


**Figure 10.** The relaxation time dependences on temperature for the investigated InGaAs bow-tie detectors with different In/Ga ratios: (a) for B197; (b) for B203; (c) for B204. Vertical columns represent the interval of the distribution of relaxation times at definite temperatures, calculated from the Figure 9. The evaluated activation energies are indicated near the relevant curves.

#### 4. Terahertz Sensitivity Measurement Results and Discussion

The bow-tie diodes were fabricated using lithography and wet etching technologies following the design of the bow-tie sensors described in [13]. The responsivity measurements of the InGaAs bow-tie detectors have been performed by 30 mW power radiation at frequency of 0.3 THz and 0.8 mW at 0.6 THz at modulation frequency of 1 kHz. The device position in the THz beam was set by raster scanning of the incident beam (Figure 11b) at the focal plane. The load resistance was set to 2.4 k $\Omega$  at 0.3 THz and 4.3 k $\Omega$  at 0.6 THz, respectively. The DC current was changed from  $-0.3$  mA to 0.3 mA, where positive voltage was connected to the metalized taper part of the antenna. The results of the experimental investigation are presented in Figure 11.

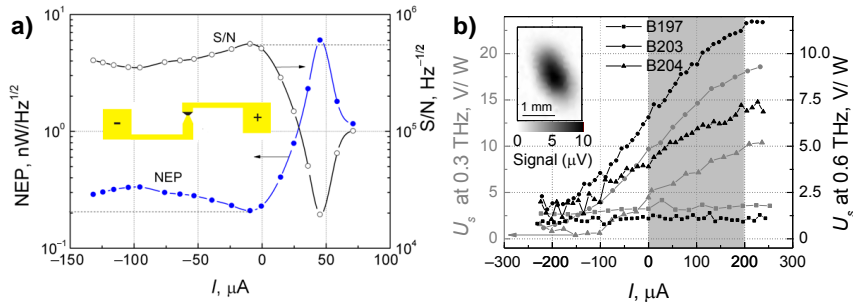


**Figure 11.** The noise equivalent power (NEP) at 0.6 THz (a) and voltage sensitivity (b) of the InGaAs diode detector with different In/Ga ratios at 0.3 THz and 0.6 THz frequency with modulation frequency of 1 kHz. Inset in the panel (a) shows the schematic design of the InGaAs bow-tie diode. Inset in the panel (b) indicates the raster scan of the 0.6 THz beam profile at the focal plane obtained with detector B203. Shadowed area in panel (b) indicates optimal working regime of the detector.

The NEP of the B203 sample as a function of current (panel (a) of Figure 11) shows weak dependence at negative bias, and the minimal value of around  $200 \text{ pW}/\sqrt{\text{Hz}}$  is reached when the current approaches zero value. With the increase of forward bias the NEP value reaches the maximal value of  $6 \text{ nW}/\sqrt{\text{Hz}}$  at  $5 \mu\text{A}$ . It is worth noting that the minimal NEP value obtained here—around  $200 \text{ pW}/\sqrt{\text{Hz}}$ —is much smaller than that reported earlier— $4 \text{ nW}/\sqrt{\text{Hz}}$  [13]—due to the more optimal growth conditions.

Figure 11b depicts the sensitivity as a function of current for all types of the studied samples at frequencies of 0.3 THz and 0.6 THz. As is seen, sensitivity of InGaAs bow-tie diodes fabricated from the wafers B203 and B204 increases while raising the current and reaches  $17.5 \text{ V/W}$  and  $10 \text{ V/W}$  at 0.3 THz and  $12.5 \text{ V/W}$  and  $7 \text{ V/W}$  at 0.6 THz, respectively, at the bias current of  $0.2 \text{ mA}$ . Higher voltage sensitivity of the detector B203 is caused by the larger asymmetry in the  $I$ - $V$  curves and stronger built-in electric fields in comparison to other studied samples. Raster scan of THz beam profile at 0.6 THz (inset in panel (b) of Figure 11) illustrates the suitability of the diode for THz imaging aims.

Hence, operation parameters of the InGaAs-based bow-tie diodes can be optimized by varying conditions of the MBE growth. If the In/Ga BEP ratio is kept equal to 2.04, it allows one to reduce the low-frequency noise into the lowest level among the studied structures. The increase of the In/Ga BEP ratio to 2.06 enables one to increase the internal electric fields in the structure up to  $49 \text{ kV/cm}$ , making such wafers well suited for fabrication of sensitive— $13 \text{ V/W}$  and NEP of  $200 \text{ pW}/\sqrt{\text{Hz}}$  at 0.6 THz—room temperature bow-tie THz detectors and their further implementation in compact THz imaging systems [33]. The In/Ga BEP ratio set to 2.08 permits one to achieve the highest crystallinity; however, the internal electric fields—up to  $25 \text{ kV/cm}$ —seem to be not strong enough to provide maximal sensitivity values in the investigated diodes.

## 5. Conclusions

Noise characteristics of InGaAs bow-tie diodes are investigated over the temperatures from 77 K to 300 K. The voltage fluctuation spectral density varies proportionally to  $1/f$  at room temperature, and Lorentzian-type noise spectra appear at lower temperatures. The origin of the fluctuations in the investigated bow-tie diodes is related to the defects caused by charge carrier capture centers involved in generation and recombination processes with characteristic times from a few microseconds to tens of milliseconds. The estimated activation energies of these centers are found to be in the range from 0.15 eV to 0.36 eV. It is supposed that they are associated with the presence of the interface defects close to the InAs layer located between the InGaAs layer and InP substrate. The THz detectors grown with beam equivalent pressure In/Ga ratio equal to 2.04 exhibit the minimal level of the low-frequency noise, while InGaAs layers grown with beam equivalent pressure In/Ga ratio equal to 2.06 are found

to be well suited for fabrication of room temperature bow-tie THz detectors enabling sensitivity of 13 V/W and NEP of 200 pW/ $\sqrt{\text{Hz}}$  at 0.6 THz due to strong built-in electric field effects.

**Supplementary Materials:** The following are available online at <http://www.mdpi.com/1424-8220/18/11/3760/s1>. Figure S1: The noise measurement circuit: S is the investigated bow-tie detector;  $R_L$  denotes the load resistor;  $R_{\text{ref}}$  is the reference resistor; LNA stands for the low-noise amplifier; ADC labels the analog-to-digital converter (National Instruments<sup>TM</sup> PCI 6115 board); PC is the personal computer; Osc. shows the oscilloscope; Cr. indicates the cryostat (DN 7704); and V denotes the voltmeter.

**Author Contributions:** Conceptualization, G.V., L.M. and R.B.; Methodology, V.P., R.B., J.M., and G.V.; Growth by MBE and structural investigation, R.B.; Photoluminescence investigation, B.Č.; Low-frequency noise investigation V.P., S.P. and J.M.; THz investigation, L.M., D.J. and D.S.; Writing-Original Draft Preparation, V.P. and G.V.; Writing-Review & Editing, V.P., S.P., J.M., L.M., D.S. and G.V.; Visualization, D.J. and L.M.; Supervision, G.V.

**Funding:** This research was funded by Lietuvos Mokslo Taryba (LAT 04/2016)—project KITKAS.

**Acknowledgments:** We kindly acknowledge Remigijus Juškėnas for possibility to perform structural analysis of grown wafers and Vincas Tamošiūnas for useful discussions.

**Conflicts of Interest:** The authors declare no conflict of interest.

## References

1. Carmody, C.; Tan, H.H.; Jagadish, C.; Gaarder, A.; Marcinkevičius, S. Ion-implanted InGaAs for ultrafast optoelectronic applications. *Appl. Phys. Lett.* **2003**, *82*, 3913–3915. [[CrossRef](#)]
2. Dziuba, Z.; Przesławski, T.; Dybko, K.; Górska, M.; Marczewski, J.; Regiński, K. Negative magnetoresistance and impurity band conduction in an  $\text{In}_{0.53}\text{Ga}_{0.47}\text{As}/\text{InP}$  heterostructure. *J. Appl. Phys.* **1999**, *85*, 6619–6624. [[CrossRef](#)]
3. Przesławski, T.; Wolkenberg, A.; Regiński, K.; Kaniewski, J. Sensitive  $\text{In}_{0.53}\text{Ga}_{0.47}\text{As}/\text{InP}$  (SI) magnetic field sensors. *Phys. Status Solidi* **2004**, *1*, 242–246. [[CrossRef](#)]
4. Molis, G.; Krotkus, A.; Vaičaitis, V. Intervalley separation in the conduction band of InGaAs measured by terahertz excitation spectroscopy. *Appl. Phys. Lett.* **2009**, *94*, 091104. [[CrossRef](#)]
5. Krotkus, A. Semiconductors for terahertz photonics. *J. Phys. D Appl. Phys.* **2010**, *43*, 273001. [[CrossRef](#)]
6. Mangeney, J.; Merigault, A.; Zerounian, N.; Crozat, P.; Blary, K.; Lampin, J.F. Continuous wave terahertz generation up to 2 THz by photomixing on ion-irradiated InGaAs at 1.55  $\mu\text{m}$  wavelengths. *Appl. Phys. Lett.* **2007**, *91*, 241102. [[CrossRef](#)]
7. Baker, C.; Gregory, I.S.; Evans, M.J.; Tribe, W.R.; Linfield, E.H.; Missous, M. All-optoelectronic terahertz system using low-temperature-grown InGaAs photomixers. *Opt. Express* **2005**, *13*, 9639–9644. [[CrossRef](#)] [[PubMed](#)]
8. Kim, N.; Han, S.-P.; Ko, H.; Leem, Y.A.; Ryu, H.-C.; Lee, C.W.; Lee, D.; Jeon, M.Y.; Noh, S.K.; Park, K.H. Tunable continuous-wave terahertz generation/detection with compact 1.55  $\mu\text{m}$  detuned dual-mode laser diode and InGaAs based photomixer. *Opt. Express* **2011**, *19*, 15397–15403. [[CrossRef](#)] [[PubMed](#)]
9. Lusakowski, J.; Knap, W.; Dyakonova, N.; Varani, L.; Mateos, J.; Gonzalez, T.; Roelens, Y.; Bollaert, S.; Cappy, A.; Karpierz, K. Voltage tuneable terahertz emission from a ballistic nanometer InGaAs/InAlAs transistor. *J. Appl. Phys.* **2005**, *97*, 064307. [[CrossRef](#)]
10. El Fatimy, A.; Teppe, F.; Dyakonova, N.; Knap, W.; Seliuta, D.; Valušis, G.; Shchepetov, A.; Roelens, Y.; Bollaert, S.; Cappy, A.; et al. Resonant and voltage-tunable terahertz detection in InGaAs/InP nanometer transistors. *Appl. Phys. Lett.* **2007**, *89*, 131926. [[CrossRef](#)]
11. Seliuta, D.; Kašalynas, I.; Tamošiūnas, V.; Balakauskas, S.; Martūnas, Z.; Ašmontas, S.; Valušis, G.; Lisauskas, A.; Roskos, H.G.; Köhler, K. Silicon lens-coupled bow-tie InGaAs-based broadband terahertz sensor operating at room temperature. *Electron. Lett.* **2006**, *42*, 825–827. [[CrossRef](#)]
12. Kašalynas, I.; Seliuta, D.; Simniškis, R.; Tamošiūnas, V.; Köhler, K.; Valušis, G. Terahertz imaging with bow-tie InGaAs-based diode with broken symmetry. *Electron. Lett.* **2009**, *45*, 833–835. [[CrossRef](#)]
13. Minkevičius, L.; Tamošiūnas, V.; Kašalynas, I.; Seliuta, D.; Valušis, G.; Lisauskas, A.; Boppel, S.; Roskos, H.G.; Köhler, K. Terahertz heterodyne imaging with InGaAs-based bow-tie diodes. *Appl. Phys. Lett.* **2011**, *99*, 131101. [[CrossRef](#)]
14. Kašalynas, I.; Venckevičius, R.; Seliuta, D.; Grigelionis, I.; Valušis, G. InGaAs-based bow-tie diode for spectroscopic terahertz imaging. *J. Appl. Phys.* **2011**, *110*, 114505. [[CrossRef](#)]

15. Kašalynas, I.; Venckevičius, R.; Valušis, G. Continuous wave spectroscopic terahertz imaging with InGaAs bow-tie diodes at room temperature. *IEEE Sens. J.* **2013**, *13*, 50–54. [[CrossRef](#)]
16. Minkevičius, L.; Tamošiūnas, V.; Kojelis, M.; Žašinas, E.; Bukauskas, V.; Šetkus, A.; Butkutė, R.; Kašalynas, I.; Valušis, G. Influence of Field Effects on the Performance of InGaAs-Based Terahertz Radiation Detectors. *J. Infrared Millim. Terahertz Waves* **2017**, *38*, 689–707. [[CrossRef](#)]
17. Sužiedėlis, A.; Ašmontas, S.; Gradauskas, J.; Valušis, G.; Roskos, H.G. Giga- and terahertz frequency band detector based on an asymmetrically-necked n-n<sup>+</sup>-GaAs planar structure. *J. Appl. Phys.* **2003**, *93*, 3034–3038. [[CrossRef](#)]
18. Seliuta, D.; Širmulis, E.; Tamošiūnas, V.; Balakauskas, S.; Ašmontas, S.; Sužiedėlis, A.; Gradauskas, J.; Valušis, G.; Lisauskas, A.; Roskos, H.G.; et al. Detection of terahertz/sub-terahertz radiation by asymmetrically-shaped 2DEG layers. *Electron Lett.* **2004**, *40*, 631–632. [[CrossRef](#)]
19. Boppel, S.; Lisauskas, A.; Krozer, V.; Roskos, H.G. Performance and performance variations of sub-1 THz detectors fabricated with 0.15 μm CMOS foundry process. *Electron. Lett.* **2011**, *47*, 661–662. [[CrossRef](#)]
20. Jones, B.K. Electrical noise as a reliability indicator in electronic devices and components. *IEE Proc. Circuits Dev. Syst.* **2002**, *149*, 13–22. [[CrossRef](#)]
21. Pralgauskaitė, S.; Palenskis, V.; Matukas, J.; Šaulys, B.; Kornijčuk, V.; Verdingovas, V. Analysis of mode-hopping effect in Fabry-Pérot multiple-quantum well laser diodes via low frequency noise investigation. *Solid State Electron.* **2013**, *79*, 104–110. [[CrossRef](#)]
22. Dobbert, J.; Tran, L.; Hatami, F.; Masselink, W.T.; Kunets, V.T.; Kunets, V.P.; Salamo, G.J. Low frequency noise in InSb/GaAs and InSb/Si channels. *Appl. Phys. Lett.* **2010**, *97*, 102101. [[CrossRef](#)]
23. Chisum, J.D.; Grossman, E.N.; Popović, Z. A general approach to low noise readout of terahertz imaging arrays. *Rev. Sci. Instrum.* **2011**, *82*, 065106. [[CrossRef](#)] [[PubMed](#)]
24. Minkevičius, L.; Ragauskas, M.; Matukas, J.; Palenskis, V.; Pralgauskaitė, S.; Seliuta, D.; Kašalynas, I.; Valušis, G. InGaAs Bow-tie Diodes for Terahertz Imaging: Low Frequency Noise Characterization. In Proceedings of the SPIE Terahertz Emitters, Receivers, and Applications III, San Diego, CA, USA, 12–13 August 2012; Razeghi, M., Baranov, A.N., Everitt, H.O., Zavada, J.M., Manzur, T., Eds.; Volume 8496, p. 849612. [[CrossRef](#)]
25. Shen, H.; Dutta, M. Franz-Keldysh oscillations in modulation spectroscopy. *J. Appl. Phys.* **1995**, *78*, 2151–2176. [[CrossRef](#)]
26. Čechavičius, B.; Kavaliauskas, J.; Krivaitė, G.; Seliuta, D.; Valušis, G.; Halsall, M.P.; Steer, M.J.; Harrison, P. Photoreflectance and surface photovoltage spectroscopy of beryllium-doped GaAs/AlAs multiple quantum wells. *J. Appl. Phys.* **2005**, *98*, 023508. [[CrossRef](#)]
27. Mott, N.F.; Davis, E.A. *Electronic Processes in Non-Crystalline Materials*, 2nd ed.; Oxford University Press: New York, NY, USA, 2012; ISBN 978-0-19-964533-6.
28. Ambegaokar, V.; Halperin, B.I.; Langer, J.S. Hopping Conductivity in Disordered Systems. *Phys. Rev. B* **1971**, *4*, 2612–2620. [[CrossRef](#)]
29. Palenskis, V.; Maknys, K. Nature of low frequency noise in homogeneous semiconductors. *Sci. Rep.* **2015**, *5*, 18305. [[CrossRef](#)] [[PubMed](#)]
30. Palenskis, V. The charge carrier capture-emission process—The main source of the low-frequency noise in homogeneous semiconductors. *Lith. J. Phys.* **2016**, *56*, 200–206. [[CrossRef](#)]
31. Palenskis, V.; Glemza, J.; Vysniauskas, J.; Matukas, J. Carrier density and mobility fluctuations due to carrier retrapping process in homogeneous semiconductors. In Proceedings of the 24th International Conference on Noise and Fluctuations (ICNF), Vilnius, Lithuania, 20–23 June 2017.
32. Kirton, M.J.; Uren, M.J. Noise in solid-state microstructures: A new perspective in individual defects, interface states and low-frequency (1/f) noise. *Adv. Phys.* **1989**, *38*, 367–468. [[CrossRef](#)]
33. Venckevičius, R.; Minkevičius, L.; Reklaitis, A.; Tamošiūnas, V.; Kašalynas, I.; Jokubauskis, D.; Seliuta, D.; Voisiat, B.; Račiukaitis, G.; Valušis, G. Compact solutions for spectroscopic solid-state based terahertz imaging systems. In Proceedings of the SPIE Terahertz Emitters, Receivers, and Applications VIII, San Diego, CA, USA, 6–10 August 2017; Razeghi, M., Baranov, A.N., Pavlidis, D., Zavada, J.M., Eds.; Volume 10383, p. 1038305. [[CrossRef](#)]



3rd publication

**Fibonacci terahertz imaging by silicon diffractive optics**

**D. Jokubauskis**, L. Minkevičius, M. Karaliūnas, S. Indrišiūnas, I. Kašalynas, G. Račiukaitis and G. Valušis

*Optics Letters* **43**(12), p. 2795, 2018.

DOI: 10.1364/OL.43.002795

Manuscript version of the paper reprinted with permission of The Optical Society (OSA).

The article may be accessed online at <https://dx.doi.org/10.1364/OL.43.002795> with manuscript version accessible at <https://arxiv.org/abs/2010.03333>.

# Fibonacci terahertz imaging by silicon diffractive optics

D. JOKUBAUSKIS\*, L. MINKEVIČIUS, M. KARALIŪNAS, S. INDRIŠIŪNAS, I. KAŠALYNAS, G. RAČIUKAITIS, G. VALUŠIS

Center for Physical Sciences and Technology, Saulėtekio Ave. 3, LT-10257 Vilnius, Lithuania

\*Corresponding author: [domas.jokubauskis@ftmc.lt](mailto:domas.jokubauskis@ftmc.lt)

Received 17 April 2018; revised 8 May, 2018; accepted 11 Month 2018; posted 15 May 2018 (Doc. ID 328405); published 5 June 2018

**Fibonacci or bifocal terahertz (THz) imaging is demonstrated experimentally employing silicon diffractive zone plate (SDZP) in a continuous wave mode. Images simultaneously recorded in two different planes are exhibited at 0.6 THz frequency with the spatial resolution of wavelength. Multi-focus imaging operation of the Fibonacci lens is compared with a performance of the conventional silicon phase zone plate. Spatial profiles and focal depth features are discussed varying the frequency from 0.3 THz to 0.6 THz. Good agreement between experimental results and simulation data is revealed.**

**OCIS codes:** (050.1380) Binary optics, (050.1965) Diffractive lenses, (050.5080) Phase shift, (050.6875) Three-dimensional fabrication, (080.3630) Lenses, (080.3620) Lens system design, (110.6795) Terahertz imaging.

<https://doi.org/10.1364/OL.43.002795>

Terahertz (THz) imaging and spectroscopy displays an attractive feature to expose new possibilities and wide-ranging potential in many versatile applications. Already known implementations covering security [1,2], package inspection [3], biomedicine diagnostics [4,5] and food control [6] recently have been extended by promising studies in investigating 2D materials [7,8], surface control [9] and paintings examination [10,11]. From practical point of view, design of a THz imaging system should be compact, free of optical alignment, reliable and providing an ability of relatively rapid scans. Moreover, significant preference could be not only to record a structure of the sample, but, via determination of spectroscopic features, identify the object and, if possible, to reconstruct its three-dimensional image. Interesting and elegant approach to combine advantages of compact diffractive optics with benefits of tomographic imaging was given in [12,13]. Employing terahertz time-domain spectroscopy (THz-TDS) and unique feature of Fresnel lens which focal length is linearly proportional to the frequency, tomographic images of a target using multiple frequencies were recorded [14]. In other words, operating in a pulsed mode and utilising a Fresnel lens at different frequencies of the imaging beam allows objects reconstruction at various positions along the beam propagation path onto the same imaging plane.

In this paper, we convert the aforementioned concept into the continuous wave and discrete frequency operation mode via engagement of Fibonacci diffractive lenses [15]. In contrast to recently presented 3D printed diffractive terahertz lenses [16],

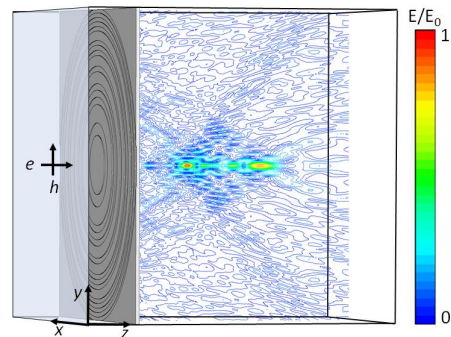


**Fig. 1.** The normalized electric field ratio  $E/E_0$  distribution in  $x$  and  $z$  directions before and after the Fibonacci diffractive zone plate at 0.6 THz frequency. Data are obtained using 3D Finite-difference time-domain (FDTD) simulations at the depicted coordinate axes, electric and magnetic field orientations.  $Z$  axis shows the THz beam propagation direction. Note that the distribution of the electric field exhibits extended focusing performance at a several points along the beam propagation path.

we demonstrate design, operation and high-resolution imaging of silicon-based Fibonacci lens for 0.6 THz frequency. It was fabricated on a monocrystalline silicon wafer using laser patterning earlier employed to produce multilevel phase Fresnel lenses of high efficiency [17]. The focusing performance was investigated theoretically and experimentally by measuring spatial profiles, the distance between the foci and focal depth at 0.3 THz and 0.6 THz. The ability to perform simultaneous imaging with the wavelength resolution of two planes separated by 7 mm distance was experimentally revealed. The multifocal imaging results were compared with the performance of the phase zone plate designed of the same diameter and material.

The Fibonacci lens design relies on Fibonacci sequence principle when the next number of the sequence is obtained adding up the two preceding ones. Based on the Fibonacci numbers, a binary aperiodic Fibonacci structure can be composed indicating that each element of the sequence is found as the concatenation of the two previous elements. As a result, non-uniform mapping of this structure provides the radial profile of the Fibonacci lens [15].



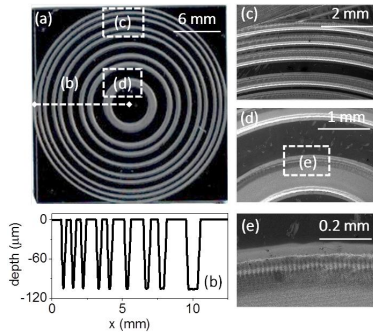


**Fig. 2.** (a) SEM images of the 0.6 THz Fibonacci (bifocal) silicon diffractive zone plate with the focal distances of  $f = 7$  mm and 13 mm; (b) the cross-section profile of ablated grooves in silicon surface; (c) and (d) zoomed area of outer and center rings, respectively; (e) displays the junction between the ablated and polished silicon surface.

In our approach, silicon, which served as a highly efficient material for multilevel phase Fresnel lenses [17], was chosen for the Fibonacci (bifocal) lens production. Initially, theoretical modelling of the electric field distribution in a space after the bifocal diffractive silicon zone plate was performed by using three-dimensional finite-difference time-domain (3D FDTD) method. The spatial resolution was set-up from 0.01 mm to 0.115 mm. To simplify the simulation, symmetry conditions of the structure were applied, and the absorbing boundary conditions were set in all the directions. The normalised electric field was recorded in the whole simulation volume. Illustrative simulation results for the volume of  $22 \times 22 \times 15$  mm<sup>3</sup> in  $x$ ,  $y$ ,  $z$  directions are presented in Fig. 1. A source of a multi-frequency plane wave, transparent to the reflected wave, was specified in the front of the zone plate plane (grey semi-transparent rectangle in Fig. 1). The predicted focusing performance of the Fibonacci lens is demonstrated in Fig. 1. As one can see the distribution of the electric field exhibits extended focusing

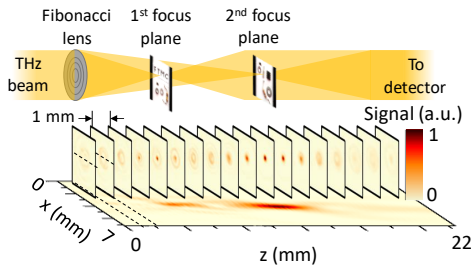


**Fig. 3.** Experimental demonstration of 0.6 THz radiation beam profiles focusing evolution along the beam propagation path. The cross-sections represent the beam alternation in focal plane direction. The distance between cross-sections - 1 mm. 2D images consist of  $66 \times 67$  pixels. Pixel size  $0.1 \times 0.1$  mm<sup>2</sup>. The dashed line represents the cross-section position in  $xz$  plane. Upper panel depicts part of the experimental set-up to record Fibonacci imaging.

performance at several points along the beam propagation with maximal intensity in the two separate focal spots of the lens. Note that the peak of the first amplitude in the  $z$ -direction is higher than the second one. Hence, such a lens can be a reasonable instrument to enable a bifocal regime of operation and provide, therefore, an option to record simultaneously images of objects placed at the different foci.

One can underline that the focusing picture is colored by a pattern of standing waves observed in reflection due to the incident and reflected plane wave interference.

According to the simulation results, the design of the silicon Fibonacci lens was developed. The focusing element was fabricated using laser ablation technology based on industrial-scale laser-direct-write (LDW) system based on a 1064 nm wavelength, a 13 ps pulse, 1 MHz repetition rate, and a 60  $\mu$ J peak energy laser (Atlantic 60 from Ekspla Ltd.) in conditions described precisely in [17]. Sample with outside diameter of 24 mm and two foci separated by a defined distance of 7 mm was fabricated on monocrystalline silicon (orientation (110), with resistance 0.01-1 M $\Omega$ cm and refractive index 3.46). The SEM images of the lens are shown in Fig. 2. The step-profile scanned across the center of the sample and enlarged zones of the ablated rings are displayed in Fig. 2(b-e). It is seen that the ablated grooves near the center and near the edge of the diffractive element are ablated to the depth of 100  $\mu$ m.

The focusing performance of the bifocal silicon diffractive zone plate was investigated by measuring Gaussian beam intensity distribution in the focal plane and along the optical axis at the 0.3 THz and 0.6 THz frequencies. Experimental demonstration of the focusing was evidenced using the experimental setup described in [17]. The radiation was collimated by 12 cm focal length high-density polyethylene (HDPE) lens and registered with resonant THz antenna-coupled micro-bolometer detector [4]. The intensity of THz radiation distribution along the beam propagation direction and cross-sections at  $z$ -direction with a step of 1 mm was measured. The results of the focusing performance are presented in Fig. 3. It is

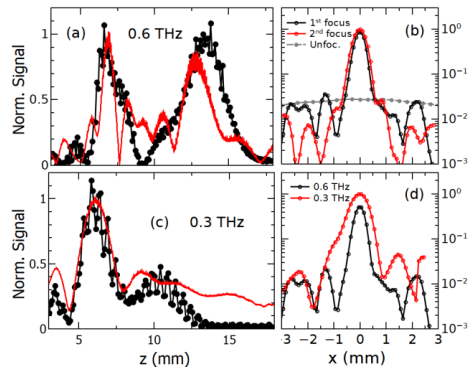


**Fig. 4.** Normalized THz radiation power distribution along  $z$ -axis (a) and along  $x$ -axis at the 1st and 2nd focus (b) measured for 0.6 THz frequency radiation. The unfocused relatively scaled 0.6 THz radiation profile is depicted for comparison. The THz power distribution for 0.3 THz is depicted along  $z$ -axis (c) and  $x$ -axis (d) where it is compared with the distribution along  $x$ -axis for 0.6 THz measured at the 1st focus. Red solid lines in panels (a) and (c) are the results of simulation using 3D FDTD method.

seen that two clearly distinguished focal spots are observed at different distances, 6 mm and 13 mm, from the Fibonacci focusing element. These foci are located at certain axial positions determined by the Fibonacci numbers [15]. It is worth noting that noticeable Airy disks are pronounced between the first and second focal spots.

Aiming to prove that indeed the observed foci are related to the Fibonacci lens performance, the cross-section of the measured profiles and simulated focusing operation was compared (Fig. 4.) The distribution of THz radiation power for 0.6 THz along the z-axis is depicted in panels (a), (b) and (d). For more illustrative comparison, additionally, the data obtained at 0.3 THz (panel (c)) are presented as well. It is evident that two well-resolved foci can be identified at 6.7 and 13.4 mm away from the Fibonacci lens surface when illuminating the lens with the 0.6 THz frequency radiation. One can note that experimental data fit well with the simulated results. Moreover, the first maximum along the z-axis is narrower than the second one which is also in accordance with the simulated data obtained by FDTD. The beam profile in the x-direction exhibits similar features: the first focus is also narrower than the second one with the corresponding full-width half-maximum (FWHM) values of 0.46 and 0.55 mm, respectively. Note that the FWHM of the unfocused Gaussian beam before the Fibonacci lens reaches 8.55 mm, and the signal amplitude is nearly two orders of magnitude lower as it can be nicely seen in Fig 4 (b).

To get a more expressive picture via comparison, the radiation frequency was detuned to 0.3 THz, then both focusing operation and profile features were evaluated and compared with that at 0.6 THz. It is seen from Fig. 4(c) that experimental results precisely follows the simulation data: the second focus becomes smooth and demonstrates a trend to disappear, while the 1<sup>st</sup> one experiences no significant change. If one looks from the profile point of view, in the x-axis direction, the signal amplitude at 0.3 THz is in a factor of 2 higher than that at 0.6 THz at the first focus as it is compared in Fig. 4 (d). The FWHM along the x-axis for 0.3 THz radiation is 0.76 mm, while for 0.6 THz it amounts to 0.46 mm.

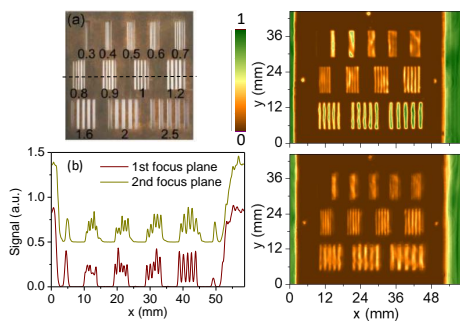


**Fig. 5.** Photo (a) of the resolution target with indications of the period in mm scale. Dashed line indicates measuring place to determine cross section; (b) - cross section of the THz beam profile along the x-axis at  $y=22$  mm, data lines shifted by a factor of 0.5 for convenience of illustration. THz images of resolution target at 0.6 THz: (c) panel presents image at 6.6 mm away from the Fibonacci lens (the first focus plane) while (d) shows - at 13.3 mm (the second focus plane).

As the bifocal operation is clearly resolved, one needs to evaluate its spatial resolution and demonstrate the THz Fibonacci imaging. Spatial resolution was investigated using specially constructed resolution target consisting of periodic metallic stripes (photo depicted in Fig. 5 (a)) with different distances in between. As one can see, the smallest period of stripes which was clearly resolved in both foci is 0.8 mm, i. e. it amounts to 1.6 factor of wavelength,  $1.6 \times \lambda$ . Therefore, reasonable spatial resolution can be expected and excellent quality in recording THz images in both focal planes simultaneously.

For the Fibonacci imaging aims a special sample was constructed. It is based on a plastic frame of 7 mm thickness to fit the distance between both foci as is illustrated in (Fig. 4 (a)). The frame was then covered with a sticky tape from both sides enabling thus, on the one hand, transparency for THz light and ability to record images in transmission geometry, on the other hand, to realise two planes for attachment of the objects under test. To get broader illustration different objects were chosen (Fig. 6 (a)). The sample's 1<sup>st</sup> plane was composed of "FTMC" - Lithuanian abbreviation of the Center for Physical Sciences and Technology - written in pencil on the office paper, resistor with 0.5 mm width leads, SMD 1206 resistor, 4.6 mm width washer, 4 mm width nut, 6.7 mm width washer. The sample's 2<sup>nd</sup> plane consists of SMD 1206 resistor, 4.6 mm width washer, 0.5 mm width pin, 1.27 mm pin pitch SOIC package, resistor with 0.5 mm width leads, 6.7 mm width washer. Terahertz imaging results obtained using various diffractive optics elements are shown in

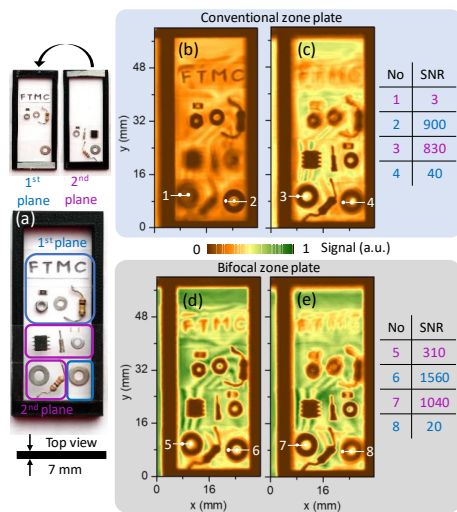


**Fig. 6.** THz images at two planes, separated by 7 mm spacer obtained simultaneous recording at 0.6 THz. Photos of the sample (a). THz images at 0.6 THz obtained using conventional zone plate: image focused on the 1<sup>st</sup> plane (b) and focused on the 2<sup>nd</sup> plane (c). Images obtained using bifocal zone plate: optimal image taken by moving the sample along z-axis to achieve the best contrast in both sample planes (d) and image taken at the highest contrast in the 2<sup>nd</sup> plane contrast (e). Positions of signal amplitudes used for SNR calculations are represented as white lines with dots.

Fig. 6, panels (b-e). Each image was acquired in 500 s time and consists of 400 x 250 pixels with 0.3 mm pitch.

Initially, the conventional diffractive silicon phase zone plate, SDZP, [17] with the focal distance of 10 mm was investigated, and relevant images were recorded. THz images at 0.6 THz are displayed in panels (b) and (c) of Fig. 6. Results show that using SDZP the THz images of good quality (signal-to-noise ratio, S/N, is more than 800) can be recorded aligning imaging to relevant foci. It is clearly seen from Fig. 6(b), when the focus is tuned to the first plane, it enables to image objects in the first plane, even pencil written letters "FTMC" – are evidently resolved. However, the image quality of the objects placed in the second plane is not tolerable – images are blurred, S/N ratio is in the range of 40. Similar picture was obtained with the tuning to the second plane – in that case objects placed in the second plane can be plainly distinguished (S/N ratio is in the order of 900), but the THz image quality in the first plane is strongly decreased, especially it can be seen that the letters "FTMC" are hardly to be resolved. (Fig. 6(c)). Therefore, the conventional phase zone plate is not suitable for simultaneous THz imaging in both planes.

In contrast, in bifocal zone plate case, the image was recorded collecting the THz light from both foci in a single scan. Results are depicted in Fig. 6 (d). Since both planes are in focus now, all the objects placed in both planes as well as pencil written letters "FTMC" are clearly resolved. S/N ratio in the first and the second foci is respectively in the order of 1500 and 300.

It is interesting to compare operation of both diffractive components – conventional SDZP and the Fibonacci lens. To set the same recording conditions, the imaging system was tuned for THz radiation collection just from the 2nd focus of bifocal zone plate in order to compare the resolution with the conventional SDZP. The obtained image is shown in Fig. 6 (e). If compare it with the image given in Fig. 6 (c), one can see that second sample plane spatial resolution is comparable to conventional zone plate image, while the image resolution in the first plane is strongly decreased. It let to conclude that two plane THz imaging can be performed using Fibonacci (bifocal zone) plate reaching simultaneously wavelength resolution in both foci.

To conclude, the silicon-based Fibonacci (bifocal) diffractive zone plate for 0.6 THz frequency has been developed, and its employment for bifocal THz imaging with the wavelength resolution was demonstrated. It not only enriched a family bifocal focusing elements like bifocal zoom lenses using plasmonic metasurfaces [18], fractal zone planes with reduced aberration in visible range [19], plates based on generalized *m*-bonacci sequence [20], but also extended routes to manipulate with THz beam [21] in continuous wave mode using diffractive optics components providing thus an additional tool for further development of compact and alignment-free THz imaging systems.

**Funding.** This work was supported by the Research Council of Lithuania (LAT 04/2016).

© 2018 Optical Society of America. One print or electronic copy may be made for personal use only. Systematic reproduction and distribution, duplication of any material in this paper for a fee or for commercial purposes, or modifications of the content of this paper are prohibited.

## References

1. M. Kato, S. R. Tripathi, K. Murate, K. Imayama, and K. Kawase, *Opt. Express* **24**, 6425 (2016).
2. U. Puc, A. Abina, M. Rutar, A. Zidanšek, A. Jeglič, and G. Valušis, *Appl. Opt.* **54**, 4495 (2015).
3. L. Minkevičius, V. Tamošiūnas, I. Kašalynas, D. Seliuta, G. Valušis, A. Lisauskas, S. Boppel, H. G. Roskos, and K. Köhler, *Appl. Phys. Lett.* **99**, 97–100 (2011).
4. I. Kašalynas, R. Venckevičius, L. Minkevičius, A. Sešek, F. Wahaia, V. Tamošiūnas, B. Voisiat, D. Seliuta, G. Valušis, A. Švigelj, and J. Trontelj, *Sensors* **16**, 432 (2016).
5. B. C. Q. Truong, A. J. Fitzgerald, S. Fan, and V. P. Wallace, *Biomed. Opt. Express* **9**, 1334 (2018).
6. A. A. Gowen, C. O'Sullivan, and C. P. O'Donnell, *Trends Food Sci. Technol.* **25**, 40–46 (2012).
7. J. D. Buron, F. Pizzocchero, P. U. Jepsen, D. H. Petersen, J. M. Caridad, B. S. Jessen, T. J. Booth, and P. Bøggild, *Sci. Rep.* **5**, 1–7 (2015).
8. P. R. Whelan, K. Iwaszczuk, R. Wang, S. Hofmann, P. Bøggild, and P. U. Jepsen, *Opt. Express* **25**, 2725 (2017).
9. K. Ueno, S. Nozawa, and H. Misawa, *Opt. Express* **23**, 28584 (2015).
10. C. L. K. Dandolo, J.-P. Guillet, X. Ma, F. Fauquet, M. Roux, and P. Mounaix, *Opt. Express* **26**, 5358 (2018).
11. C. L. Koch Dandolo, M. Picollo, C. Cucci, M. Ginanni, E. Prandi, M. Scudieri, and P. U. Jepsen, *J. Infrared, Millimeter, Terahertz Waves* **38**, 413–424 (2017).
12. X. C. Zhang, *Philos Trans. Ser A Math Phys Eng Sci* **362**, 283–289 (2004).
13. S. Wang, B. Ferguson, D. Abbott, and X. C. Zhang, *J. Biol. Phys.* **29**, 247–256 (2003).
14. S. Wang and X.-C. Zhang, *J. Phys. D: Appl. Phys.* **37**, R1–R36 (2004).
15. J. A. Monsoriu, A. Calatayud, L. Remon, W. D. Furlan, G. Saavedra, and P. Andres, *IEEE Photonics J.* **5**, 3400106–3400106 (2013).
16. W. D. Furlan, V. Ferrando, J. A. Monsoriu, P. Zagrajek, E. Czerwińska, and M. Szustakowski, *Opt. Lett.* **41**, 1748 (2016).
17. L. Minkevičius, S. Indrišiūnas, R. Šniaukas, B. Voisiat, V. Janonis, V. Tamošiūnas, I. Kašalynas, G. Račiukaitis, and G. Valušis, *Opt. Lett.* **42**, 1875 (2017).
18. X. Yin, T. Steinle, L. Huang, T. Taubner, M. Wuttig, T. Zentgraf, and H. Giessen, *Light Sci. Appl.* **6**, e17016 (2017).
19. W. D. Furlan, G. Saavedra, and J. A. Monsoriu, *Opt. Lett.* **32**, 2109–2111 (2007).
20. F. Machado, V. Ferrando, W. D. Furlan, and J. A. Monsoriu, *Opt. Express* **25**, 8267 (2017).
21. L. Minkevičius, K. Madeikis, B. Voisiat, I. Kašalynas, R. Venckevičius, G. Račiukaitis, V. Tamošiūnas, and G. Valušis, *J. Infrared, Millimeter, Terahertz Waves* **35**, 699–702 (2014).

4th publication

**Bessel terahertz imaging with enhanced contrast realized by silicon multi-phase diffractive optics**

L. Minkevičius, **D. Jokubauskis**, I. Kašalynas, S. Orlov, A. Urbas and G. Valušis

*Optics Express* **27**(25), pp. 36358-36367, 2019.

DOI: 10.1364/OE.27.036358

This is an open access article distributed under the Creative Commons Attribution License (CC-BY).

The article may be accessed online at <https://doi.org/10.1364/OE.27.036358>

# Bessel terahertz imaging with enhanced contrast realized by silicon multi-phase diffractive optics

LINAS MINKEVIČIUS,<sup>1,2</sup> DOMAS JOKUBAUSKIS,<sup>1,3</sup>  IRMANTAS KAŠALYNAS,<sup>1</sup> SERGEJ ORLOV,<sup>1</sup> ANTANAS URBAS,<sup>1</sup> AND GINTARAS VALUŠIS<sup>1</sup>

<sup>1</sup>Center for Physical Sciences and Technology, Saulėtekio Ave. 3, LT-10257 Vilnius, Lithuania

<sup>2</sup>linas.minkevicius@ftmc.lt

<sup>3</sup>domas.jokubauskis@ftmc.lt

**Abstract:** Bessel terahertz (THz) imaging employing a pair of thin silicon multi-phase diffractive optical elements is demonstrated in continuous wave mode at 0.6 THz. A proposed Bessel zone plate (BZP) design – discrete axicon containing 4 phase quantization levels – based on high-resistivity silicon and produced by laser ablation technology allowed to extend the focal depth up to 20 mm with minimal optical losses and refuse employment of bulky parabolic mirrors in the imaging setup. Compact THz imaging system in transmission geometry reveals a possibility to inspect objects of more than 10 mm thickness with enhanced contrast and increased resolution up to 0.6 of the wavelength by applying deconvolution algorithms.

© 2019 Optical Society of America under the terms of the [OSA Open Access Publishing Agreement](#)

## 1. Introduction

Employment of terahertz (THz) radiation to inspect thick objects is one of the most considerable difficulties in THz imaging technology. As a rule, THz beam propagation in bulky media suffers phase perturbation and troublesome attenuation inducing thus deterioration in the image contrast. This outcome is a strong obstacle in implementation of versatile hand-held unattended package inspection systems [1], development of single pixel imaging methods [2] or spectroscopic imaging systems [3,4]. To circumvent the issue one needs to apply special optical means aiming to organize a self-reconstructing beam profile. Moreover, these advantages should be built-in in the setup preserving simultaneously features of convenient usage of terahertz imaging systems: they should be compact, preferably, free of optical alignment and cumbersome optical components, reliable, and providing an ability of relatively rapid scans. The first hurdle can be well-evaded reshaping conventional Gaussian beam profile into the Bessel beam [5,6], while reduced size of the THz imaging system can be kept using compact THz emission sources, e. g. quantum cascade lasers [7–9], or electronic emitters [10], compact sensitive detectors such as nanometric field effect transistors [11–13], microbolometers [14–16], diode structures-based sensors [17–20], but, in particular, via replacing bulky optical passive elements, for instance, parabolic mirrors by relevant diffractive optical components [21,22]. As it was shown recently, laser ablation technology was found to be a powerful tool to fabricate effective Fresnel zone plates of different diameters [22,23], to produce anti-reflective and phase shifting structures [24] and apply them successfully for Fibonacci (bifocal) THz imaging [25]. The latter approach with two planes simultaneous image recording not only enables an increase in registration speed – imaging systems containing such kind of zone plates are capable to reach wavelength limited resolution even in case when the focal length is less than a few cm. However, it needs to be underlined that the image quality is strikingly sensitive of the sample position in respect to diffractive optical element. This circumstance, especially, in exploring thick objects in real environment, turns

into an ultimate challenge as image becomes blurred resulting in complication in resolving and identification of the recorded data.

In this work, we introduce a novel route to overcome aforementioned issues – thin and compact Bessel zone plates (BZP) based on silicon multi-phase diffractive optics – are designed, produced and demonstrated in the THz transmission imaging system. In contrast to already known approaches in fluorescence [26] and light-sheet microscopy [27], where a single diffractive element is employed in combination with conventional lenses, we propose to use in the experimental setup a second BZP for enhanced imaging purposes in terms of increased compactness. The discrete axicons containing 4 phase quantization levels were fabricated from a high-resistivity silicon by employing laser ablation technology allowed to extend the focal depth up to 20 mm with minimal optical losses and refuse employment of bulky parabolic mirrors in the imaging set up. Compact THz imaging system reveals possibility to inspect objects of more than 10 mm thickness with enhanced contrast, weak dependence on the sample thickness and position due to long focal depth as well as increase its resolution up to high level by applying deconvolution algorithms [28].

## 2. Design and fabrication

The choice of discrete axicons relies on their advantages being more compact and exhibiting much less optical losses in the material if compared with classical cone axicons [29]. Moreover, their manufacturing is much easier because the accuracy of the cone requires special attention, especially, in the central zone with the tip of the cone. As an important detail in the design served our previous finding that at least 4 phase quantization levels are required for rational trade-off between the effective focusing performance and the fabrication complexity [22]. Silicon discrete BZP design was simulated using three-dimensional finite-difference time-domain (3D FDTD) method.

Silicon wafer of 0.52 mm thickness with specific resistance 10–1000 kΩ·cm and refractive index of 3.44 served as the core material for the manufacturing of the BZP. Their design with phase quantization level of  $P = 4$  were processed employing laser direct ablation technology. The set up was composed of Pharos-SP laser (*Light Conversion Ltd*, wavelength 1028 nm, pulse duration = 350 fs, energy = 50 μJ, repetition rate = 100 kHz), IntelliSCAN-14 scanner by *ScanLab* and F-Theta f100 lens by *SillOptics* with scanning speed = 1000 mm/s.

Design and fabricated BZP of 20 mm diameter are depicted in Fig. 1. Panel Fig. 1(a) displays the BZP peculiarities of four phase quantization design and its cross-section of the central part with indicated dimensions, while panel Fig. 1(b) shows photo of the fabricated discrete axicon was obtained by *Hirox KH-7700* microscope. Enlarged subzones of the ablated rings with detailed geometrical parameters are displayed in Fig. 1(c). Measured subzones depths of produced structures are  $h_1 = 47 \mu\text{m}$ ,  $h_2 = 106 \mu\text{m}$ ,  $h_3 = 154 \mu\text{m}$ , and these results are in a good agreement with calculated ones. The center hole in the BZP was used for the optical alignment.

Point of departure for the beam profile modelling was the proposition that a unit amplitude plane illuminates a thin circular hologram with complex transmission function

$$t(\rho) = \exp(-ik_\rho \rho) \quad (1)$$

where  $k_\rho = k \sin \theta$ ,  $k$  is the wave number,  $\theta$  is the halfcone angle of the Bessel beam and  $\rho$  is the radial coordinate in the  $(x, y)$  plane. A practical realization of the smooth phase function described by the Eq. (1) is rather complicated. For the sake of the simplicity we implement a quantified phase coded hologram with a complex step-like profile, so the complex transmission function  $N$  levels can be written as

$$t(\rho) = \exp\left(-ik_\rho \left[ N \frac{\rho \sin \theta}{\lambda} - N \left\lfloor \frac{\rho \sin \theta}{\lambda} \right\rfloor \right] \frac{1}{N} \right). \quad (2)$$

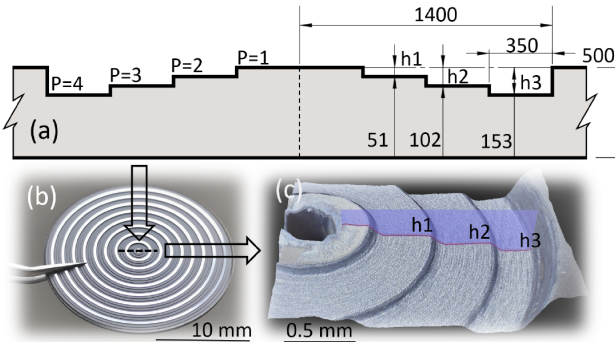


**Fig. 1.** (a) Bessel zone plate design and its cross-section of the central part with marked dimensions in microns of four phase quantization levels. (b) The photo of thin silicon-based Bessel diffractive element for the 0.6 THz. (c) 3D reconstruction of the zoomed area in the center part displays ablated and polished silicon surface,  $h$  indicates the places where groove depth was measured using *Hirox* digital microscope.

The spatial frequency of the hologram is determined by the relation

$$k\rho_0 \sin \theta = 2\pi, \quad (3)$$

and the difference  $dh$  in the heights of the steps  $h_1, h_2, h_3$ , see Fig. 1, is defined as  $k(n-1)dh = 2\pi/N$ , here  $n$  is the refractive index of the material used for production of the hologram, and  $N$  is the quantization number. In our case, the axicon angle can be estimated from Eq. (3), here  $k = 2\pi/\lambda$ ,  $\rho_0 = 1.4$  mm, giving  $\theta = 0.36$  rad. The length of the Bessel zone can be estimated from the geometry of the setup [30] and is given by the formula  $L = 2D\cotan(\theta)$ . For plane wave illumination,  $D$  is the radius of BZP,  $D = 9.8$  mm and  $\theta$  is axicon angle. This gives us the maximal theoretical Bessel zone length of 52 mm. However, in our case, see Fig. 2(e) the FWHM of the incident Gaussian beam is approximately 7.5 mm, thus reducing the length Bessel zone to approximately 20 mm. Propagation of the electric field after a discrete axicon mask was estimated numerically using the Eq. (5) (Appendix A).

### 3. Results and discussion

Silicon discrete BZP focusing properties were also modelled using 3D FDTD method. The simulation was performed with spatial resolution from  $10 \mu\text{m}$  up to  $100 \mu\text{m}$ . To simplify calculations, symmetry conditions of the structure were used, and the absorbing boundary conditions were set in all directions. Plane wave of 0.6 THz frequency served as an excitation source. The electric field was recorded in the whole simulation volume.

The simulated Bessel beam 2D cross-section at the center of BZP via normalized electric field reconstruction at 0.6 THz frequency is shown in Fig. 2(a). As it is seen, one can expect transformation of the plane electric field profile into a needle-like shape along the beam propagation.

To confirm the prediction, performance of the BZP was investigated by measuring Gaussian beam intensity distribution in the focal plane and along the optical axis at 0.6 THz frequency using modified experimental setup [22]. The THz radiation was registered by resonant THz antenna-coupled microbolometer detectors [14]. Results of the focusing performance are presented in panels Figs. 2(b) and 2(c). One can see clearly resolved focal spot of a needle shape starting from  $z = 4$  mm and ending at  $z = 21$  mm away from the BZP sample as expected. For comparison,

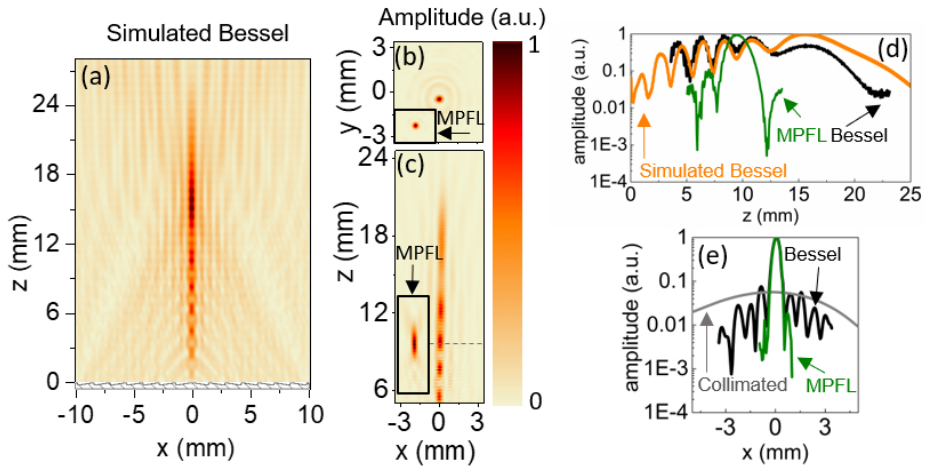


**Fig. 2.** (a) Normalized THz radiation power distribution simulation using 3D FDTD method in  $xz$  plane. (b) and (c) – Measured distribution of the THz radiation in  $xy$  plane and in  $xz$  plane, respectively, at 0.6 THz frequency focused by the Bessel zone plate. Insets in (b) and (c) show performances of the multi-phase Fresnel zone plates with 4 phase quantization levels (MPFL) for comparison in the same scale. (d) and (e) – Experimentally evaluated distribution (black line) of THz signal amplitude along  $z$  axis and  $x$  axis, respectively, compared with the results of the simulations using 3D FDTD method (orange lines) and MPFL focusing (green lines). Collimated radiation profile at 0.6 THz is also depicted for comparison.

insets in Figs. 2(b) and 2(c) denote focusing performance of multilevel phase Fresnel zone plates lens (MPFL) with 4 phase quantization levels and 1 cm focal length [22] in the same scale.

More detailed focusing features can be extracted analyzing THz signal amplitude distributions along  $z$  axis and  $x$  axis. Experimental results compared with the relevant simulation data are presented in Fig. 2(d). It is seen that the Bessel peak amplitude value is located at  $z = 9$  mm with the 20 mm depth of focus evaluated at  $1/e^2$  of the maximal amplitude value. For comparison, the MPFL with the same focal distance at 10 mm, reveals at least 6 times shorter focal depth reaching only 3 mm. It is worth noting that the simulated and the measured focused beam profile along the optical path are in a good agreement and displays only negligible deviation between each other as it can be observed in the peak around  $z = 15$  mm. The focused beam profiles with BZP and MPFL as well as collimated beam profile cross-section in  $x$  direction are given in Fig. 2(e). Our experimental realization of the Bessel beam is inline with standard finite energy approximation – Bessel-Gaussian beam. In this model the envelope has a Gaussian profile, therefore it is helpful to use semi-logarithmic scale to estimate the width of Gaussian envelope. And indeed, we see, that the width of a Gaussian envelope is approximately 3 mm. The estimated full width half maximum (FWHM) for both diffractive elements are  $\sim 0.43$  mm. One can note that the unfocused incident Gaussian beam before the Bessel zone plate exhibits  $\text{FWHM} = 7.2$  mm, while the signal amplitude is nearly 15 dB lower.

While planning our experiment, we have carefully chosen parameters so, that the Gaussian envelope of Bessel-like beam had sufficient width to enable diffractionless behavior of the beam [31]. We found that our estimations are also in line with recent results [32].

Experimental results on the Bessel focusing performance are presented in Fig. 3. Panel (a) presents imaging resolution and its dependence on the target position relevant to the BZP lens



from  $z = -6$  mm to  $z = 6$  mm by 1 mm steps. It was estimated using specially constructed resolution target consisting of periodic metallic stripes with different distances in between as shown in Fig. 3(b). It is worth underlying that the Gaussian beam was focused on the sample and transmitted radiation was collected in a novel way – without parabolic mirrors employing two BZP lenses instead, – and it is the main difference from the set up described elsewhere [22]. As one can see in Fig. 3(c), apertures of 2.5 mm to 0.6 mm periods in all images can be clearly resolved. Moreover magnified image of 0.6 mm period aperture indicates that spatial resolution of 0.3 mm can be reached applying deconvolution procedures. One can note that it amounts to  $0.6 \lambda$ .

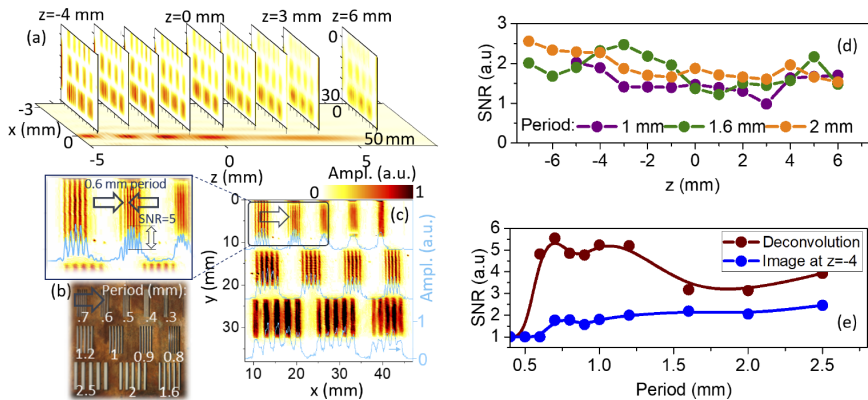


**Fig. 3.** (a) Experimental demonstration of the Bessel focusing performance using resolution target imaging at 0.6 THz radiation along the beam propagation path. The cross sections of resolution target position along optical path represent the resolution alternation in the focal plane direction. The distance between cross sections was set to 1 mm. 2D images consist of  $390 \times 116$  pixels. Pixel size:  $150 \mu\text{m} \times 300 \mu\text{m}$ . (b) Photo of the resolution target with indications of the apertures period in mm scale. (c) Enhanced contrast image of resolution target at 0.6 THz after the deconvolution procedure, where blue line represents the cross-section of each period of stripes (data lines shifted down for convenience of illustration). (d) Dependence of signal to noise ratios on  $z$  coordinate evaluated for apertures of 1 mm, 2 mm and 2.5 mm period. (e) Dependence of imaging resolution on aperture period, where the target position in  $z$  direction is fixed at  $z = -4$  mm. Enhanced image resolution after deconvolution procedure is shown additionally for comparison.

Raw images recorded with BZPs displays blurred characteristic due to the conical structure of the Bessel beam and its side lobes, which is seen in Fig. 2(e). This distinctive feature of the circular transversal structure of the Bessel beam apparently distorts the recorded images. This can be understood taken into account the fact that the intensity in the first ring of the Bessel beam is equal to that of the central spike. Due to the propagation invariance of the Bessel beam, the shape of this blur is relatively independent of the position in the field-of-view. Nevertheless, the whole recorded stack of images can be approximated as a convolution of the object function with a spatial intensity distribution of the Bessel beam. This understanding enables to use standard deconvolution techniques allowing thus to recover the transversal resolution of the Bessel beam imaging. It is evidenced in Fig. 3(c), where the reconstructed image of all raw images in  $z$  direction is depicted. The blue line represents cross sections of the target apertures. As it is seen, the smallest period of stripes, which was clearly resolved is 0.6 mm. As the wavelength at 0.6 THz is 0.5 mm, therefore, the wavelength limited spatial resolution and good quality can be expected in recording THz images independently of the sample distance from the BZP. Dependence of

signal noise ratio (SNR) evolution on the target position along  $z$  axis for target aperture periods of 1 mm, 1.6 mm and 2 mm are depicted in Fig. 3(d). It should be noted that SNR for 2 mm aperture exceeds 2 times and is weakly dependent of the target position in  $z$  direction. The same trend is kept for other apertures, too, however, the SNR value is reduced and varies around 1.5. Furthermore, sample position does not provide significant effect for the different aperture periods. It illustrates the Bessel beam advantage to be insensitive for inaccurate sample positioning with respect to BZPs location. By applying deconvolution technique contrast enhancement up to 5 times is reached for aperture periods starting from the wavelength scale up to 1.25 mm. It is apparent in Fig. 3(e), where enhancing SNR is visible for larger features. Combination of deconvolution algorithms and the Bessel beam enables high resolution imaging, as it could be seen from Fig. 3(e), where 0.3 mm aperture is resolved with  $\text{SNR}=5$  without the necessity of the accurate position of the object under test. We note that the structured illumination (Bessel and other non-diffracting beams) was successfully applied for imaging purposes in fluorescence [26] and light sheet microscopy [27], where resolution less than wavelength was achieved. Details on the deconvolution algorithms and filters are available in Supplementary material.

To illustrate the quality of the Bessel THz imaging, a specially designed stack of targets for thick media imaging measuring 30 mm $\times$ 60 mm $\times$ 3 mm was 3D printed with PLA filament using *Ultimaker 2* printer. Figure 4(a) demonstrates principle of the imaging procedure, where the object, with thickness varied from 3 mm to 12 mm, was placed between two silicon BZP, i. e. no parabolic mirrors were employed in image recording. For comparison, the same imaging procedure was also performed using conventional MPFL with  $f = 10$  mm and  $P = 4$  characterized in Figs. 2(b) and 2(c). Imaging results of the different sample thicknesses using Bessel zone plate and MPFL are given in Figs. 4(b) and 4(c). Varying the content of the stack from 1 to 4 identical targets, the Bessel imaging advantage is revealed via obtained horizontal profiles up to stack thickness of 12 mm in Figs. 4(d) and 4(e). As we can see in Figs. 4(d) and 4(e), in the case of 3 mm aperture and thickness of 1 sample  $\text{SNR} = 8$  is achieved with MPFL while  $\text{SNR} = 4$  was obtained with BZP is worse due to self-healing effect [6] and much longer depth of field of Bessel beam. The advantage of BZP appears when the stack is composed of 2 or more samples: SNR achieved with BZP increases from 2 to 4 times better values than MPFL.

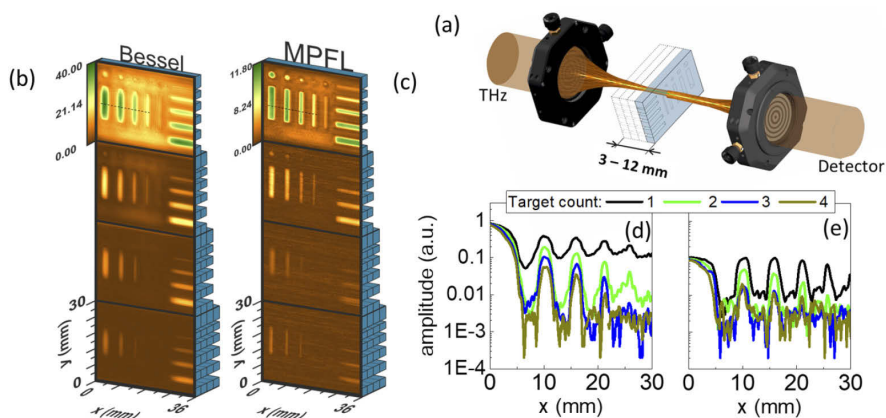


**Fig. 4.** (a) Part of Bessel imaging setup displaying object under test placed between two silicon BZP. (b) and (c) – Stacks of 1 to 4 identical targets were imaged using Bessel zone plates and conventional MPFL, respectively, aiming to evaluate THz imaging performance of thick objects. (d) Beam profiles at  $y=17$  mm (position is marked as dashed black line in (b) and (c)) of obtained images using BZL. (e) MPFL beam are shown for comparison.

#### 4. Conclusions

To summarize, Bessel terahertz imaging of more than 10 mm thickness objects via silicon multi-phase diffractive optics is designed and demonstrated in continuous wave mode at 0.6 THz. Discrete axicon containing 4 phase quantization levels based on high-resistivity silicon allowed to extend the focal depth up to 20 mm with minimal optical losses and record images with up to 5-fold enhanced contrast and increased resolution up to  $0.6 \lambda$  by applying deconvolution algorithms. Experimental data agree well with the modelled results obtained using three-dimensional finite-difference time-domain method.

#### Appendix A: Description of the deconvolution algorithm

A standard minimum mean square error (Wiener) filter to process the 3D-stack of recorded data (more information can be found in [28]) was employed. Bearing in mind the fact that the convolution can be understood as a multiplication performed in Fourier (reciprocal) space, each spatial frequency of the object was multiplied independently with the point spread function of the imaging system  $H(x, k_z)$ . The deconvolution can be performed in the Fourier space by correcting the spatial components of the recorded image stack  $I(x, y, k_z)$  by multiplying it with Wiener filter  $H_W(x, k_z)$  – the filter, given by the equation [28]:

$$H_W(x, k_z) = \frac{H^*(x, k_z)}{|H(x, k_z)|^2 + SNR^{-2}(k_z)} \quad (4)$$

minimizes the expected mean square error for a signal-to-noise of the model,  $SNR(k_z)$ .

The main drawback of such approach is the limited knowledge on the optical transfer function, which requires some additional experimental measurements in our setup. In order to overcome this issue we have compared results obtained using an experimentally measured intensity profile of the Bessel beam with results obtained using the equation, see Ref. [33]:

$$u(x, y, z) = \frac{1}{\lambda i} \int_{-\infty}^{\infty} \int_{-\infty}^{\infty} g(x_0, y_0) \frac{e^{ikr}}{r} dx_0 dy_0 \quad (5)$$

where  $r = \sqrt{z^2 + (x - x_0)^2 + (y - y_0)^2}$ , coordinates  $(x, y, z)$  being the coordinates of the free space and  $(x_0, y_0)$  being coordinates of the plane of the axicon mask. Wave number  $k = 2\pi/\lambda$ ,  $\lambda$  is the wavelength and  $g(x_0, y_0)$  is the transmission function of the mask.

It enabled us to estimate the signal-to-noise function SNR. One can note that due to limited knowledge of the actual spatial distribution of the Bessel beam some inaccuracy and artifacts can be expected.

Implementation of the deconvolution algorithm mainly follows procedures described in [27,28] with implementation containing two parts. The first one is calculation of the deconvolution of the filter, see Eq. (4) and its application to the 3D stack of images, while the second part is dedicated to the deconvolution of the object image.

#### Appendix B: Calculation of the deconvolution filter

The point spread function (PSF) of the discrete axicons used in the setup was experimentally determined. The digitally scanned 3D intensity distribution of the Bessel beam  $u(x, y, z)$  corresponds to the PSF function of the focusing system, see Fig. 5. Integration of the intensity along the  $y$ -axis allows to arrive at the function  $F(x, z) = \int_{-\infty}^{\infty} u(x, y, z) dy$ . From this function the optical transfer function  $H(x, k_z)$  was calculated by performing one dimensional Fourier transform  $H(x, k_z) = F_z\{u(x, y, z)\}$ .

As a next step, a model for a signal-to-noise ratio was introduced, and a power law distribution  $SNR(k_z) = ak_{cutoff}/k_z$ , where  $a$  is some experimentally determined constant

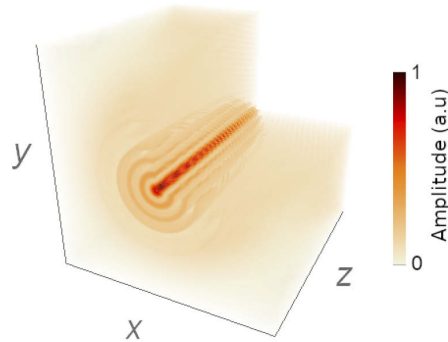


**Fig. 5.** Bessel beam illustration

needed to adjust the signal-to-noise ratio of the recorded 3D image stacks and  $k_{cutoff}$  denotes maximum spatial frequency which can be optically transmitted through the focusing system. It can be readily approximated from the numerical aperture of the used axicons and from the wavelength of the Bessel beam.

### Appendix C: Deconvolution of the object image

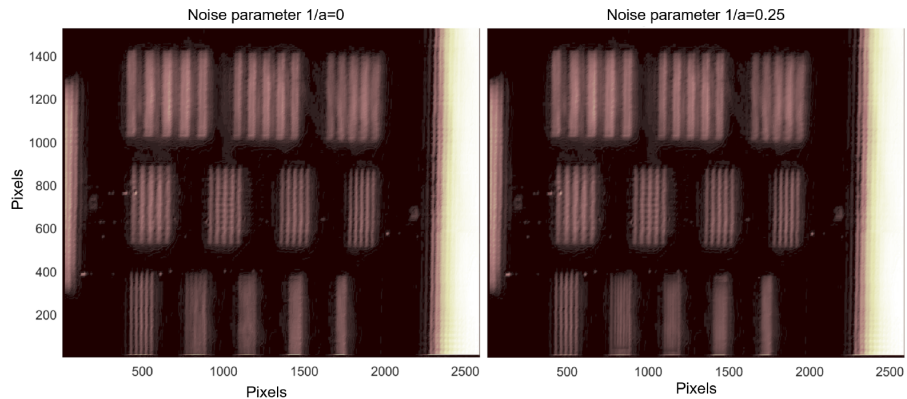


**Fig. 6.** Results of Bessel THz imaging after deconvolution using different noise parameters  $1/a$ .

Deconvolution algorithm calculation itself takes a few minutes, however we additionally do estimate effects due to a) signal-to-noise-ratio, b) slight misplacements of the sample during the z-scan and c) imperfections in experimental determination of Bessel beam profile. Additionally, these estimates are performed iteratively and may take up to 10 minutes. Here, we would like to point out that those estimations are given without any optimizations to the code.

Possible deconvolution artefacts were minimized by implementing cubic interpolation of the images in order to compensate probable lateral shift due to the axial translation. This also enabled to increase the spatial resolution.

Numerical simulation was performed using  $I(x, y, k_z) = F_z\{i(x, y, z)\}$ , where  $i(x, y, z)$  is cubically interpolated 3D stack of images. Deconvolved image  $i_{dec}(x, y, z)$  of the object was calculated

as inverse Fourier transform after applying the Wiener filter to  $I(x, y, k_z)$ . Examples of the deconvoluted images using different noise parameters of the object are presented in Fig. 6.

## Funding

European Regional Development Fund (01.2.2-LMT-K-718-01-0047); Lietuvos Mokslo Taryba (DOTSUT-247).

## Acknowledgments

The authors acknowledge Vladislavas Čižas for his precious assistance during the preparation of figures.

## Disclosures

The authors declare no conflicts of interest.

## References

1. X. Yang, T. Wu, L. Zhang, D. Yang, N. Wang, B. Song, and X. Gao, "CNN with spatio-temporal information for fast suspicious object detection and recognition in THz security images," *Signal Process.* **160**, 202–214 (2019).
2. M. J. Sun and J. M. Zhang, "Single-pixel imaging and its application in three-dimensional reconstruction: A brief review," *Sensors* **19**(3), 732 (2019).
3. D. Jokubauskis, L. Minkevičius, D. Seliuta, I. Kašalynas, and G. Valušis, "Terahertz homodyne spectroscopic imaging of concealed low-absorbing objects," *Opt. Eng.* **58**(02), 1 (2019).
4. G. Valušis, R. Venckevičius, L. Minkevičius, A. Reklaitis, V. Tamošiūnas, I. Kašalynas, B. Voisiat, D. Seliuta, G. Račiukaitis, and D. Jokubauskis, "Compact solutions for spectroscopic solid-state-based terahertz imaging systems," *Proc. SPIE* **10383**, 103830S (2017).
5. M. S. Kulya, V. A. Semenova, V. G. Bespalov, and N. V. Petrov, "On terahertz pulsed broadband Gauss-Bessel beam free-space propagation," *Sci. Rep.* **8**(1), 1390 (2018).
6. F. O. Fahrbach and A. Rohrbach, "Propagation stability of self-reconstructing Bessel beams enables contrast-enhanced imaging in thick media," *Nat. Commun.* **3**(1), 632–638 (2012).
7. L. Bosco, M. Franckić, G. Scalfari, M. Beck, A. Wacker, and J. Faist, "Thermoelectrically cooled THz quantum cascade laser operating up to 210 K," *Appl. Phys. Lett.* **115**(1), 010601 (2019).
8. A. Albo, Y. V. Flores, Q. Hu, and J. L. Reno, "Split-well direct-phonon terahertz quantum cascade lasers," *Appl. Phys. Lett.* **114**(19), 191102 (2019).
9. B. Röben, X. Lü, K. Biermann, L. Schrotke, and H. T. Grahn, "Terahertz quantum-cascade lasers for high-resolution spectroscopy of sharp absorption lines," *J. Appl. Phys.* **125**(15), 151613 (2019).
10. P. Hillger, J. Grzyb, R. Jain, and U. R. Pfeiffer, "Terahertz Imaging and Sensing Applications With Silicon-Based Technologies," *IEEE Trans. Terahertz Sci. Technol.* **9**(1), 1–19 (2019).
11. F. Schuster, D. Coquillat, H. Videlier, M. Sakowicz, F. Teppe, L. Dussopt, B. Giffard, T. Skotnicki, and W. Knap, "Broadband terahertz imaging with highly sensitive silicon CMOS detectors," *Opt. Express* **19**(8), 7827–7832 (2011).
12. M. Bauer, A. Ramer, S. A. Chevtchenko, K. Osipov, D. Cibiraitė, S. Pralgauskaitė, K. Ikamas, A. Laisauskas, W. Heinrich, V. Krozer, and H. G. Roskos, "A High-sensitivity AlGaIn/GaN HEMT Terahertz Detector With Integrated Broadband Bow-tie Antenna," *IEEE Trans. Terahertz Sci. Technol.* **9**(4), 430–444 (2019).
13. K. Ikamas, D. Cibiraitė, A. Laisauskas, M. Bauer, V. Krozer, and H. G. Roskos, "Broadband Terahertz Power Detectors Based on 90-nm Silicon CMOS Transistors with Flat Responsivity Up to 2.2 THz," *IEEE Electron Device Lett.* **39**(9), 1413–1416 (2018).
14. I. Kašalynas, R. Venckevičius, L. Minkevičius, A. Sešek, F. Wahaia, V. Tamošiūnas, B. Voisiat, D. Seliuta, G. Valušis, A. Švigelj, and J. Trontelj, "Spectroscopic Terahertz Imaging at Room Temperature Employing Microbolometer Terahertz Sensors and Its Application to the Study of Carcinoma Tissues," *Sensors* **16**(4), 432 (2016).
15. F. Simoens and J. Meilhan, "Terahertz real-time imaging uncooled array based on antenna- and cavity-coupled bolometers," *Philos. Trans. R. Soc., A* **372**(2012), 20130111 (2014).
16. N. Oda, "Uncooled bolometer-type Terahertz focal plane array and camera for real-time imaging," *C. R. Phys.* **11**(7–8), 496–509 (2010).
17. J. Torres, P. Nouvel, A. Penot, L. Varani, P. Sangaré, B. Grimbert, M. Faucher, G. Ducournau, C. Gaquière, I. I. niguez-de-la Torre, J. Mateos, and T. Gonzalez, "Nonlinear nanochannels for room temperature terahertz heterodyne detection," *Semicond. Sci. Technol.* **28**(12), 125024 (2013).
18. I. Kašalynas, R. Venckevičius, and G. Valušis, "Continuous Wave Spectroscopic Terahertz Imaging With InGaAs Bow-Tie Diodes at Room Temperature," *IEEE Sens. J.* **13**(1), 50–54 (2013).
19. L. Minkevičius, V. Tamošiūnas, I. Kašalynas, D. Seliuta, G. Valušis, A. Laisauskas, S. Boppel, H. G. Roskos, and K. Köhler, "Terahertz heterodyne imaging with InGaAs-based bow-tie diodes," *Appl. Phys. Lett.* **99**(13), 131101 (2011).

20. A. Semenov, O. Cojocari, H. W. Hübers, F. Song, A. Klushin, and A. S. Müller, "Application of zero-bias quasi-optical schottky-diode detectors for monitoring short-pulse and weak terahertz radiation," *IEEE Electron Device Lett.* **31**(7), 674–676 (2010).
21. A. Siemion, "Terahertz Diffractive Optics—Smart Control over Radiation," *J. Infrared, Millimeter, Terahertz Waves* **40**(5), 477–499 (2019).
22. L. Minkevičius, S. Indrišiūnas, R. Šniaukas, B. Voisiat, V. Janonis, V. Tamošiūnas, I. Kašalynas, G. Račiukaitis, and G. Valušis, "Terahertz multilevel phase Fresnel lenses fabricated by laser patterning of silicon," *Opt. Lett.* **42**(10), 1875–1878 (2017).
23. L. Minkevičius, S. Indrišiūnas, R. Šniaukas, G. Račiukaitis, V. Janonis, V. Tamošiūnas, I. Kašalynas, and G. Valušis, "Compact diffractive optics for THz imaging," *Lith. J. Phys.* **58**(1), 99–107 (2018).
24. M. Tamošiūnaitė, S. Indrišiūnas, V. Tamošiūnas, L. Minkevičius, A. Urbanowicz, G. Račiukaitis, I. Kašalynas, and G. Valušis, "Focusing of Terahertz Radiation With Laser-Ablated Antireflective Structures," *IEEE Trans. Terahertz Sci. Technol.* **8**(5), 541–548 (2018).
25. D. Jokubauskis, L. Minkevičius, M. Karaliūnas, S. Indrišiūnas, I. Kašalynas, G. Račiukaitis, and G. Valušis, "Fibonacci terahertz imaging by silicon diffractive optics," *Opt. Lett.* **43**(12), 2795–2798 (2018).
26. M. G. L. Gustafsson, "Surpassing the lateral resolution limit by a factor of two using structured illumination microscopy," *J. Microsc.* **198**(2), 82–87 (2000).
27. T. Vettenburg, H. I. Dalgarno, J. Nylk, C. Coll-Lladó, D. E. Ferrier, T. Čížmár, F. J. Gunn-Moore, and K. Dholakia, "Light-sheet microscopy using an Airy beam," *Nat. Methods* **11**(5), 541–544 (2014).
28. R. C. Gonzalez and R. E. Woods, "Minimum Mean Square Error (Wiener) Filtering," in *Digital Image Processing* (Prentice Hall, 2007), chap. 5.8, pp. 374–379.
29. Y. Yu and W. Dou, "Generation of pseudo-Bessel beams at THz frequencies by use of binary axicons," *Opt. Express* **17**(2), 888–893 (2009).
30. A. Vasara, J. Turunen, and A. T. Friberg, "Realization of general nondiffracting beams with computer-generated holograms," *J. Opt. Soc. Am. A* **6**(11), 1748 (1989).
31. J. C. Gutiérrez-Vega and M. A. Bandres, "Helmholtz–Gauss waves," *J. Opt. Soc. Am. A* **22**(2), 289 (2005).
32. D. Madhi, M. Orniotti, and A. Aiello, "Cylindrically polarized Bessel–Gauss beams," *J. Opt.* **17**(2), 025603 (2015).
33. K. Iizuka, "Fresnel-Kirchhoff's Approximate Formula," in *Engineering Optics*, (Springer, 2008), chap. 3.3, pp. 60–62, 3rd ed.

5th publication

**Titanium-Based Microbolometers: Control of Spatial Profile of Terahertz  
Emission in Weak Power Sources**





L. Minkevičius, L. Qi, A. Siemion, **D. Jokubauskis**, A. Sešek, A. Švigelj, J. Trontelj,  
D. Seliuta, I. Kašalynas and G. Valušis  
*Applied Sciences* **10**(10), p. 3400, 2020.  
DOI: 10.3390/app10103400

This is an open access article distributed under the Creative Commons Attribution  
License (CC-BY).

The article may be accessed online at <https://doi.org/10.3390/app10103400>

Article

# Titanium-Based Microbolometers: Control of Spatial Profile of Terahertz Emission in Weak Power Sources

Linās Minkevičius<sup>1,\*</sup>, Liang Qi<sup>1</sup>, Agnieszka Siemion<sup>2</sup>, Domas Jokubauskis<sup>1</sup>,  
Aleksander Sešek<sup>3</sup>, Andrej Švigelj<sup>3</sup>, Janez Trontelj<sup>3</sup>, Dalius Seliuta<sup>1</sup>, Irmantas Kašalynas<sup>1</sup>  
and Gintaras Valušis<sup>1</sup>

<sup>1</sup> Department of Optoelectronics, Center for Physical Sciences and Technology, Saulėtekio Ave. 3, 10257 Vilnius, Lithuania; liang.qi@ftmc.lt (L.Q.); domas.jokubauskis@ftmc.lt (D.J.); dalius.seliuta@ftmc.lt (D.S.); irmantas.kasalynas@ftmc.lt (I.K.); gintaras.valusis@ftmc.lt (G.V.)

<sup>2</sup> Faculty of Physics, Warsaw University of Technology, 75 Koszykowa, 00662 Warsaw, Poland; agnieszka.siemion@pw.edu.pl

<sup>3</sup> Laboratory for Microelectronics, Faculty of Electrical Engineering, University of Ljubljana, Tržaška 25, 1000 Ljubljana, Slovenia; aleksander.sesek@fe.uni-lj.si (A.S.); andrej.svigelj@fe.uni-lj.si (A.Š.); janez.trontelj1@guest.arnes.si (J.T.)

\* Correspondence: linas.minkevicius@ftmc.lt; Tel.: +370-5-243-1200

Received: 17 April 2020; Accepted: 11 May 2020; Published: 14 May 2020



**Featured Application:** Convenient and easy-to-use detectors for accurate adjustment and control of spatial mode profiles without additional focusing components for various weak power THz sources operating either in time-domain or continuous wave regimes.

**Abstract:** Terahertz (THz) imaging and spectroscopy set-ups require fine optical alignment or precise control of spatial mode profile. We demonstrate universal, convenient and easy-to-use imaging—resonant and broadband antenna coupled ultrasensitive titanium-based—dedicated to accurately adjust and control spatial mode profiles without additional focusing optical components of weak power THz sources. Versatile operation of the devices is shown using different kinds of THz—electronic multiplier sources, optical THz mixer-based frequency domain and femtosecond optoelectronic THz time-domain spectrometers as well as optically pumped molecular THz laser. Features of the microbolometers within 0.15–0.6 THz range are exposed and discussed, their ability to detect spatial mode profiles beyond the antennas resonances, up to 2.52 THz, are explored. Polarization-sensitive mode control possibilities are examined in details. The suitability of the resonant antenna-coupled microbolometers to resolve low-absorbing objects at 0.3 THz is revealed via direct, dark field and phase contrast imaging techniques as well.

**Keywords:** microbolometer; terahertz sensing; terahertz imaging systems; dark field method; phase contrast method

## 1. Introduction

Terahertz (THz) imaging and spectroscopy revealed itself as promising technologies for a large variety of applications [1]. Because of non-ionizing nature of THz radiation, imaging in this range can be found as a beneficial tool for medicine and biomedical stuff inspection [2–4]. As THz frequencies display the ability to propagate in dielectric medium without strong attenuation, THz imaging and spectroscopy can also serve as valuable instruments for security needs [5–7], post packages inspection [8–10] or industrial materials control and their identification [11–14]. However, direct implementation of THz technology still meets severe difficulties related mainly to reliability of active components (emitters and detectors) and issues of precise alignment of the optical system due to the



presence, as a rule, of passive bulky optical elements like mirrors, lenses or beam splitters. Thus, effective and convenient operation under real environmental conditions still needs to overcome alignment and compact optics problems [15]. On the other hand, it is of decisive demand to provide adequate and favourable control of the spatial mode profile of illumination. In particular, it has strong impact in THz spectroscopy for quality of recorded THz spectra in increasing its bandwidth, lowering the noise floor, as well as by reducing uncertainties in observational data [16–18]. It displays also important role in THz imaging, especially, in examining bulky objects when extraordinary means are needed to be applied in THz beam engineering aiming to provide appropriate image quality [19,20].

Spatial mode profiles of discrete THz spectrum radiation from backward wave oscillators and quantum cascade lasers were already studied by employing thin film vanadium oxide (VOx) based bolometers [21]. Moreover, image of the beam emitted by an optoelectronic THz time-domain spectrometer was recorded using a camera integrating an array of THz optimized antenna-coupled amorphous silicon-based microbolometers [22]. Indeed, it is of distinct interest as THz time-domain spectrometers become widespread, they require precise alignment to get well collimated THz beams, hence, it is beneficial to engage easy-to-use imaging detector to accurately adjust these optical systems. The sensitivity of the presented microbolometers allowed to register images of spatial mode profiles as well as video images despite the fact that their average power was in the range of a few  $\mu\text{W}$  [22].

The developed and described here antenna-coupled titanium-based microbolometer (Ti-mB) [23] was initially applied in compact THz imaging systems for security aims [24,25]. Its high sensitivity was successfully exploited also in medical applications via direct THz imaging of carcinoma affected tissues [26].

In a given work, by coupling of the titanium microbolometers with relevant resonant antennas, we modified these sensitive detectors into universal, convenient and easy-to-use imaging instruments well-suited to accurately adjust weak power THz sources without additional focusing components. They can be employed in imaging systems operating either in time-domain or in continuous wave modes for precise alignment and control of their spatial mode profiles. Versatile operation of the devices is displayed engaging different kinds of THz emitters – electronic multiplier sources (THz ELS), optical THz mixer-based frequency domain (THz FDS) and femtosecond optoelectronic THz time domain (THz TDS) spectrometers as well as optically pumped molecular THz laser (THz OPML). Features of the microbolometers coupled with resonant antennas in subTHz range, within the 0.15–0.6 THz range, are exposed and discussed here. The ability to monitor spatial mode profile even far above the antennas resonances, up to 2.52 THz, is explored. Moreover, the possibilities of polarization-sensitive mode control are examined in details, and the recorded mode control results are compared with that obtained using commercially available pyroelectric sensors. In addition, the suitability of the resonant antenna coupled Ti-mB to resolve low-absorbing objects at 0.3 THz is revealed via direct, dark field and phase contrast imaging techniques.

## 2. Bolometers' Design and Experimental Set-Ups

The design of antenna-coupled Ti-mB and its cross section are presented in Figure 1. As it can be seen, the device is constructed using air-bridged approach. The dual dipole THz antenna is coupled to the bolometer and serves as a filter that aims to efficiently collect the incident THz radiation and convert its energy to temperature change. The Ti-mB and THz antenna were processed on a few microns thin SiN membrane to enhance the sensitivity and the response time via reduction of thermal losses of the instrument. The metalized bottom plate under the antenna-bolometer acts as reflecting mirror, additionally amplifying the received signal on the dipole. More detailed description on the design and the technology used to manufacture such devices can be found in Refs. [23,24].

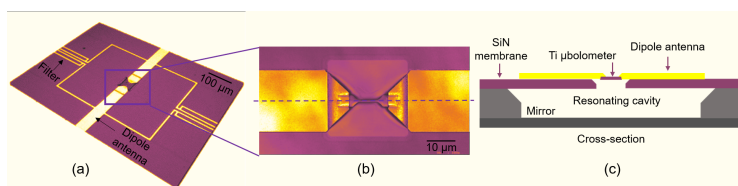


**Figure 1.** The photo of the designed terahertz titanium-based microbolometer with antenna and filters (a). The enlarged view of the bridge active part of the microbolometer: the antenna area is approximately  $500 \mu\text{m} \times 500 \mu\text{m}$ , the geometry of visible titanium bridge amounts to  $12 \mu\text{m}$  length and  $2 \mu\text{m}$  width (b). The cross-section of microbolometric detector. Note that the selectivity was enhanced by adjustment of the dipole antenna geometry and the resonant-cavity design: back side reflection mirror was positioned at the quarter wavelength distance (c). Adapted from Refs. [23,24].

Experimental set-ups for terahertz beam profiles imaging and their control are shown in Figure 2. All experiments were performed using raster scanning technique with one pixel detector from linear array of 4 or 32 pixels to obtain beam profile images in  $xy$  plane. The measuring time per pixel in most experiments was in between 10 ms and 20 ms. The technical details on used equipment and measurement techniques are presented in Section 4.

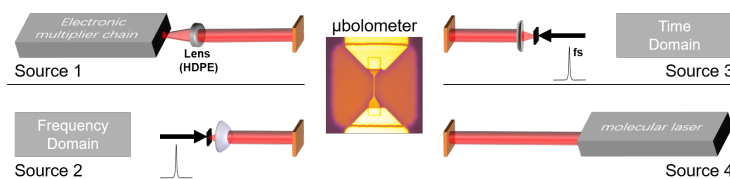


**Figure 2.** Experimental set-up for imaging of terahertz beam profiles using different THz emitters. Source 1—electronic multiplier chain emitting radiation of 0.15 THz, 0.3 THz and 0.6 THz frequencies in continuous wave mode. Source 2—low temperature grown gallium arsenide (LTG GaAs) photo-mixer coupled with silicon lens in frequency domain spectrometer delivering radiation from 0.1–2 THz. Source 3—photoconductive antenna on LTG GaAs from time domain spectrometer generating broadband radiation up to 2.5 THz. Source 4—optically pumped continuous wave molecular THz laser emitting the discrete spectrum at 0.76 THz, 1.63 THz and 2.52 THz. Center panel displays photo of Ti-based microbolometer.

### 3. Measurement Results and Discussion

Conventional the diagnostic tool to investigate the THz beam's spatial profile is typical beam imaging, where radiation intensity is scanned in the plane perpendicular to the direction of propagation. To measure the beam profile, focusing optics is usually used to concentrate THz radiation aiming to increase the detected signal. However, any additional focusing element in beam path can distort the beam profile and in many cases cause unwanted interferences. In the THz range, it is of particular importance to use off-axis parabolic mirrors, but then small misalignment can strongly affect the beam profile. As an alternative, one can use plastic lenses; however, they display feature to change focus distance depending on the frequency of incident radiation and they are not so attractive in broadband THz TDS systems, where frequency range, as a rule, extends by two orders of magnitude. To measure the beam profile correctly, one needs to scan unfocused beam that requires high responsivity THz sensor to have sufficient signal-to-noise ratio (SNR). The use of a coherent detector in such a case is limited because the Si lens coupled detector yields limited imaging resolution. Usually, one can employ conventional variable size aperture scanning and Hartmann test techniques to measure far field beam profile [16]. One can note that such approaches are easy to apply and do not require reconfiguration of set-up, nonetheless, reaching high spatial resolution, especially for high THz frequencies, can be rather

complicated because it is determined by the aperture size, and its reduction, consequently, induces the decrease in SNR.

### 3.1. Mode Control in Electronic Multiplier Sources

Initially, the focus of the investigation was attributed to spatial features of THz radiation delivered from electronic multiplier sources. One can note that profile was artificially perturbed by detuning the source from the optimal working regime. The results are shown in Figure 3, where the performance of Ti-mB to record a continuous wave (CW) mode is demonstrated for different polarizations and at three selected frequencies 0.6 THz, 0.3 THz and 0.15 THz. For comparison, measurement results registered by the pyroelectric detector are illustrated in a panel (a) of Figure 3, while the beam profiles at different polarizations are presented in panels (b) and (c). Pyroelectric detector in principle does not detect the polarization of the incident light, thus, registered signal represents total power value of the THz radiation. Despite this fact, the signal values induced in microbolometer and presented in panel (b) are 4–7 times larger than those in panel (a) if compared within the same frequency. In contrast, the microbolometer is polarization-sensitive, thus, not only the mode profiles, but also their fine structure are clearly resolved, which is visible in Figure 3b,c. Comparing the polarization extinction ratio (PER), it amounts to 11 dB, 11.8 dB and 7.8 dB at 0.6 THz, 0.3 THz, 0.15 THz, respectively, which indicates the suitability of the Ti-mB for polarization-sensitive applications. Special emphasis is required to the results obtained at 0.15 THz (panel (c)). Estimates show that the microbolometer connecting wires can act as additional coupling antennas disturbing consequently precise control of the radiation polarization and the mode shape.

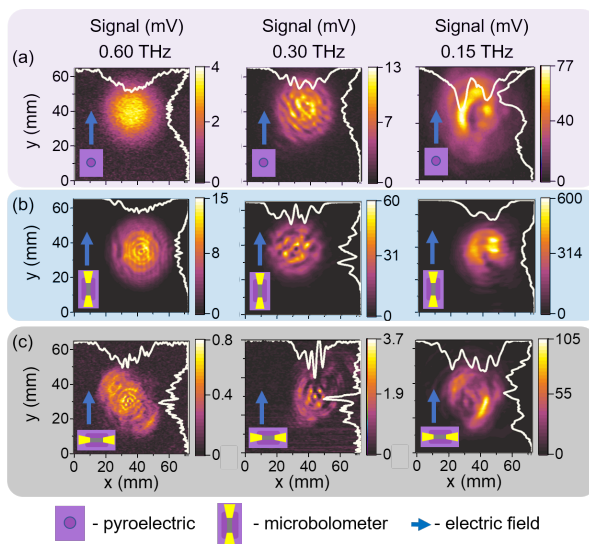


**Figure 3.** Scheme of polarisation orientation and THz beam profiles obtained using electronic multiplier chain source operating in a continuous wave (CW) mode at different frequencies: 0.6 THz, 0.3 THz and 0.15 THz. Reference measurements using pyroelectric detector (a); results using microbolometer when the dipole antenna is in parallel to the electric field of the incident light (b); results using microbolometer when the dipole antenna is perpendicular to the electric field of the incident light (c). White lines indicate intensity cross sections along the relevant axes.

### 3.2. Mode Control in Frequency Domain Spectrometer

One of the important issues to record qualitative spectra, is the precise alignment of the spectroscopic or imaging systems. To illustrate suitability of Ti-mB for such aims, we have performed

a special study using optical mixer-based frequency domain spectrometer. The THz FDS is operating within the frequency range 0.1–2 THz and it delivers radiation of circular polarization of about 1  $\mu$ W power at 0.2 THz. Therefore, no exceptional attention was attributed to the polarization-related features; however, we restricted ourselves to subTHz range, close to the designed antennas resonances. The mode profile was disturbed intentionally to reveal abilities of the device in recording spatial mode structure. The mode profile was not corrected intentionally. A linear array of the bolometers coupled with antennas exhibiting resonances around 0.2 THz and 0.4 THz was investigated. The results of the measurements are presented in Figure 4. As it is seen, spatial mode profiles are clearly resolved, in particular, at 0.2 THz (panel (a)), where delivered power is close to the maximal value.

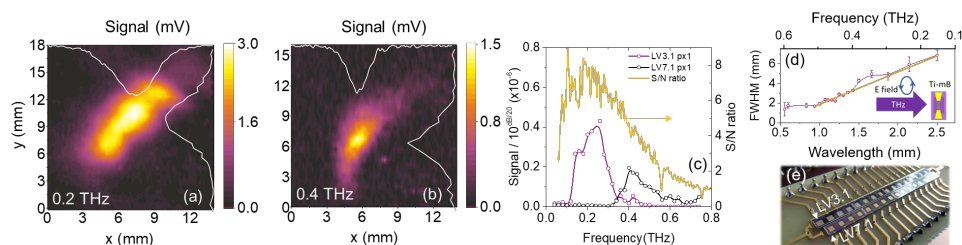


**Figure 4.** THz beam spatial profiles emitted by low-temperature grown GaAs-based emitter in frequency domain spectrometer at 0.2 THz (a) and 0.4 THz (b) recorded using a linear array of the bolometers coupled with antennas. White lines indicate intensity cross sections along the relevant axes. Spectral characteristics of the detectors with different resonant dipole antennas and spectra normalized to the spectrometer signal-to-noise ratio (SNR) (c); full-width half-maximum (FWHM) dependency on the wavelength with linear approximation depicted by the dark yellow line (d), configuration of measurement scheme and polarization are depicted in the inset of (d). A photo of dual frequency THz linear array, where the top line of pixels is designed for frequencies around 0.2 THz and the bottom line for frequencies around 0.4 THz. The pixel pitch is 2 mm (e).

Moreover, the frequency selected exactly falls into relatively broad antenna resonance. The spatial profile presented at 0.4 THz (Figure 4b) is less expressed. It was intentionally done aiming to highlight the convenience and universal operation of the device by detuning the emission frequency to the red side of the spectrum of the antenna resonance as can be evident from panel (c). Despite this fact, the spatial profile can still be precisely controlled although the power absorbed by the microbolometer is significantly reduced. This advantage can further be exploited in determining and monitoring spectral properties of frequency domain spectrometer. It can be illuminated, for instance, via determination of full-width half-maximum (FWHM) dependency on the wavelength of the emission. The results are depicted in Figure 4d. As one can see, the FWHM increases with the wavelength, and the dependence can be approximated by a linear law represented by a dark yellow line (Figure 4d). Thus, Ti-mB microbolometers and their linear array (Figure 4e) can manifest themselves as powerful instruments in fine alignment and control in spectrometers employing weak power CW THz sources.

### 3.3. Mode Control in Time-Domain Spectrometer

In the context of the obtained results in THz frequency-domain, it is reasonable to turn the research into time-domain spectrometry and check a suitability of Ti-mB for this kind of THz systems. In contrast to frequency domain, inherent feature of time-domain spectroscopic systems is their broadband radiation; on the other hand, power of the radiation is in the same range as in THz FDS, i.e., of a few microwatts. Furthermore, THz TDS systems require precise alignment to measure spectra correctly or record images of acceptable quality. In both cases the polarisation of the incident light was parallel to the bolometer axis.

To reveal picture of operation, two types of microbolometers were designed for the experiments: the first one was coupled with resonant antennas for 0.3 THz and the second for 0.7 THz frequency. The choice of the resonant frequencies was motivated by features of the emission—the 0.3 THz line is close to the maximal value in the red side of the spectrum, while 0.7 THz at the blue one, as it can be seen in the measured THz emission spectrum results presented together with experiment schematics in Figure 5a. Sharp lines gracing with the emission spectrum are due to the water vapour absorption in the air. Spatial mode profiles recorded in parallel polarization in respect to microbolometer axis using different coupling antennas are displayed in Figure 5b,c. As it can be seen, the mode profiles can be precisely recorded using both types of antennas. The microbolometer coupled to 0.3 THz resonant antenna removes high-frequency components of the radiation; however, its spatial profile, due to strong low-frequency constituents, reproduces the shape of the mode quite well. The distribution registered at other resonant frequency, around 0.7 THz, shows quite similar picture; however, the spatial mode distribution is narrower in comparison with that at 0.3 THz frequency. One can presume that these data also reproduce correctly the spatial mode distribution despite of the absence of relatively strong low-frequency components recorded. The data obtained allow to infer that the antenna-coupled bolometers can be used for mode profiles control in various optoelectronic THz time-domain spectrometers excited by femtosecond laser pulses [27].

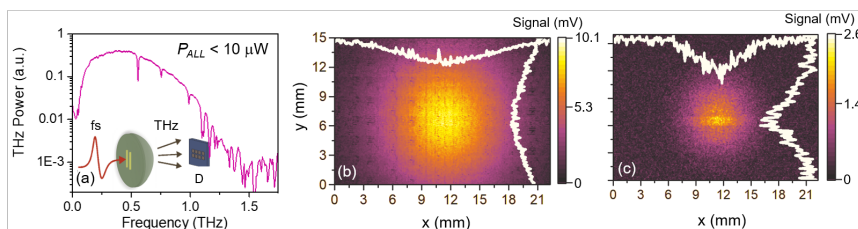


**Figure 5.** Spectrum of THz pulsed emitter (antenna switch) plotted in semi log scale (a). The measurement geometry is shown in the inset, where fs denotes to optical femtosecond pulse exciting THz emission from LTG GaAs optoelectronic switch, D labels Ti-mB detector. Note sharp lines caused by water vapour absorption in the air decorating the THz emission spectrum. Beam profiles of THz pulsed emitter obtained with antenna-coupled Ti-mB optimized for resonant frequencies of 0.3 THz (b) and 0.7 THz (c). White lines indicate intensity cross sections along the relevant axes.

### 3.4. Mode Control in Optically-Pumped Molecular Laser

Since the bolometers exhibit very high sensitivity, it would be of a particular interest to explore their properties far above the coupling antennas resonances. If a mode control could be possible under these unusual conditions, it could extend the device application areas into THz systems with a wider frequency band of operating and hence making the microbolometers more universal. In these experiments, we have chosen THz OPML as a source of radiation delivering discrete spectrum of 0.76 THz, 1.63 THz and 2.52 THz at various power levels. Special attention was given to polarization-related control; it deserves to be mentioned that the spatial mode profile was intentionally disturbed by varying power of the optical pumping and adjusting grating of the pumping laser [28].

The experimental results of bolometers investigation are presented in Figure 6 together with reference data recorded by the commercially available pyroelectric detector. Emission powers at 0.76 THz, 1.63 THz and 2.52 THz frequencies were 1.6 mW, 1.6 mW and 7 mW, respectively, i.e., they were kept in a low level in comparison to conventional powers used in this type of lasers. As it can be seen, reference data presented in Figure 6a can be understood as the averaged signal since the detector used is insensitive to the polarization. The polarization-resolved mode structures—both for parallel and perpendicular polarizations—are displayed in panels (b, c) and allow to analyse in details spatial profiles of the unfocused modes. As the diameter of the laser beam profile amounts to 11 mm, its

spatial deviations can be also nicely distinguished. The estimated polarization extinction ratio was found to be of 2.2 dB, 11.3 dB and 8.9 dB at 0.76 THz, 1.63 THz, 2.52 THz, respectively, suggesting additional application option of the Ti-mB for polarization-sensitive mode profile far above the antenna resonances. Relatively low PER value obtained at 0.76 THz can be explained by two constituents of the mode distinctly observed in Figure 6c.

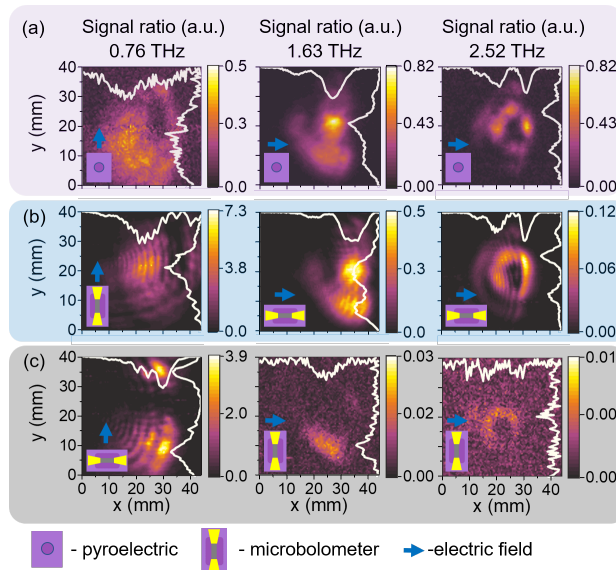


**Figure 6.** THz beam profiles of different polarizations obtained using optically-pumped molecular THz laser operating in a continuous wave mode at frequencies: 0.76 THz, 1.33 THz and 2.52 THz. Reference measurements using pyroelectric detector (a); results using microbolometer when the dipole antenna is in parallel to the electric field of the incident light (b); results using microbolometer when the dipole antenna is perpendicular to the electric field of the incident light (c). White lines indicate intensity cross sections along the relevant axes.

### 3.5. Imaging with Spatial Filtering Methods

To illustrate the sensitive operation of the developed Ti-mBs and their versatile operation using weak power sources we have proceeded in an opposite way that is usually applied in a conventional THz imaging. Here, as a rule, THz images come from scanning the object with the focused beam and registering the focused radiation on the detector making thus induced signal much larger—we have oriented our research for future applications when images without raster scanning, e.g., employing detectors arrays will be required. In such cases, the apertures of imaging optical elements become of a particular importance as the THz wavelength is large in comparison with diameters of optical elements and propagation distances. Therefore, a novel optical solutions [15] are needed allowing to design and manufacture compact optical elements with large aperture sizes and reasonable focal lengths. A special role can be attributed to the case of low absorbing or transparent samples, when the object observation and registration of its internal structure grow into a tremendous challenge [29]. It is related to the fact that power detectors record intensity of the radiation which suffers almost no observable change in the given circumstances, and the shift of the phase of incident radiation becomes a single quantity to be recorded.

In what follows, we employ both single pixel and arrays of the sensitive Ti-mB to record THz images of low absorbing objects under unfocused THz illumination. Both techniques—direct imaging and spatial filtering methods—are used to create a THz image of object inducing phase changes

(uniform amplitude) and that can be registered by intensity sensitive Ti-mB. Conventionally, such filter must be inserted in the Fourier plane in the used imaging system and it will affect only some spatial frequencies of the Fourier spectrum of the object. One can distinguish different methods like bright and dark field [30], Schlieren [31] or phase contrast [32,33] depending on the filter type. They differ in principles and type of the filter; however, all of them permit to create an intensity pattern corresponding to phase changes in the object. The phase contrast method enables linear mapping between phase shift introduced by the object and recorded intensity pattern. In a given study we preferred a phase contrast and dark field methods to register not focused radiation with sensitive Ti-mB.

Results of the investigation together with experimental set-up are given in Figure 7. To elucidate sensing features of the microbolometers, a sample consisting of various low absorbing objects—rubber, paper towel, napkin, sponge, sponge with metal wire inside, plastic (from 1 to 4 layers), aperture of 4 mm in diameter, dots made of silicone, acrylic and wax as well as metal as the reference—was composed and prepared. Measurement set-up for this kind of research is depicted in Figure 7a. As one can see, it is slightly different from that displayed in Figure 2 because of the filter inserted.

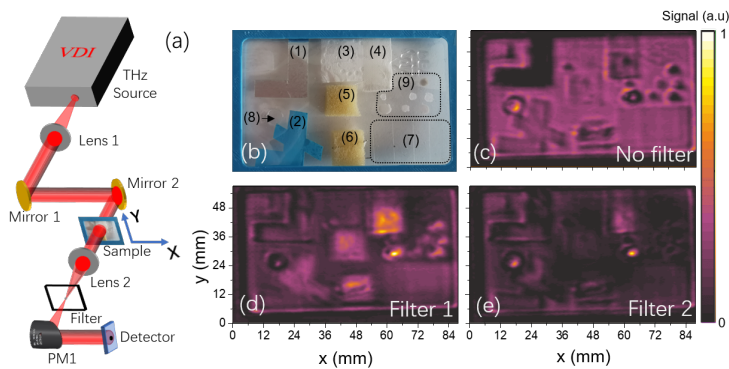


**Figure 7.** Principal scheme of phase contrast imaging set up for 0.3 THz, where L1—HDPE lens with  $f = 12$  cm, M1, M2—gold plated flat mirrors, sample, L2—TPX lens with  $f = 6$  mm, Filter—(1):  $\varnothing = 2$  mm circle shaped four paper sheets, (2)— $\varnothing = 2$  mm circle shaped aluminum foil, PM1—off axis parabolic mirror with  $f = 5$  cm (a). Photo of the sample with plastic substrate film, it consists of: (1)—metal, (2)—rubber, (3)—paper towel, (4)—napkin, (5)— sponge, (6)—sponge with metal wire inside, (7)—plastic (from 1 to 4 layers), (8)—aperture (diameter: 4 mm), (9)—dots, made of silicone, acrylic and wax (b). Direct raster scan image of the sample at 0.3 THz (c). Phase contrast images obtained using filter 1 (d) and filter 2 (e). THz image pixel size:  $0.3 \text{ mm} \times 0.3 \text{ mm}$ ; images consist of  $292 \times 190$  pixels.

Two types of filters were used in the experiments: the filter 1, consisting of 2 mm circle shaped four paper sheets, was a phase filter introducing a phase retardation of  $\pi/2$  only in the central part of the Fourier spectrum and enabling thus to create an image using phase contrast method; second one, filter 2, circle shaped aluminum foil of 2 mm diameter, was an amplitude filter, blocking low spatial frequencies, which resulted in creating an intensity image of phase object having dark background (which is related to removal of low spatial frequencies).

Sample photo and its direct image as well as two corresponding intensity images of phase objects are shown in the corresponding panels (b–d) of Figure 7. It can be easily seen that even direct imaging nicely resolves all the objects illustrating suitability of Ti-mB for imaging of low absorbing objects. As for deeper insight, transparent objects like sponge (5 and 6) and paper tissue (4) are much better visible in case of phase contrast method (filter 1), whilst dark field method (filter 2) gives much better results for imaging of thin rubber glove (2), where we can clearly see edges of the rubber shape.

Finally, it is worth to notice the operation speed of the device. Earlier it was determined that the Ti-mB coupled with a 0.3 THz frequency dipole antenna exhibited the response time of 1  $\mu$ s range and maintained a sensitivity of 300 V/W and NEP as low as 14  $\text{pW}/\sqrt{\text{Hz}}$  [26]. If compared with other similar devices based on thermoelectricity-related phenomena, for instance, with uncooled antenna-coupled terahertz detectors based on BiSb/Sb thermocouples with 22  $\mu$ s response time and NEP of 170  $\text{pW}/\sqrt{\text{Hz}}$  [34] and bow-tie diodes operating on hot-electrons effects with sensitivity of 5 V/W, NEP of 5.8  $\text{nW}/\sqrt{\text{Hz}}$  and response time less than 7 ns [35], the described titanium-based microbolometers with readout electronics exhibit high sensitivity exceeding 200  $\text{kV}/\text{W}$  and relatively short response time (5 microseconds including electronics circuit). Therefore, these parameters together with electronics that can work up to 200 ksp/s (kilo samples per second) simultaneous sampling speed, makes the Ti-mB promising for real-time fine optical adjustment and mode profile control aims in THz spectroscopic and imaging systems as well as imaging applications and inspection of low-absorbing objects.

#### 4. Materials and Methods

Each microbolometer was fabricated from titanium, which was chosen among several appropriate materials, as its micromachining properties were found to be most suitable for silicon processing technology, temperature coefficient and reliability. The sensor was processed on the silicon nitride (SiN) membrane of 2  $\mu$ m thickness; subsequently, the titanium thermistor film is electro-deposited onto the membrane, along with the aluminum antenna and metal interconnections. The thermistor is suspended in the air by etching out the underlying membrane. The microbolometer was connected either to double-dipole or to log-periodic type THz antenna [23]. Both single pixel bolometers and their linear arrays consisting of 32 pixels were used in the experiments, where pixel size was  $2.5 \times 2.5 \text{ mm}^2$ , pixel pitch was 2.5 mm. Just one pixel of the linear array was active during all experiments. Sensitivity and NEP of the arrays of sensors exceeds 200  $\text{kV}/\text{W}$  and less than 20  $\text{pW}/\sqrt{\text{Hz}}$ , respectively. Linear arrays of titanium microbolometers were produced by Luvitera, Ltd, Vilnius, Lithuania.

Electronic multiplier sources (Virginia Diodes, Inc., Charlottesville, Virginia, United States of America) were used to generate radiation of 0.15 THz, 0.3 THz and 0.6 THz frequencies in continuous wave mode with power of 29 mW, 13.2 mW and 0.56 mW, respectively.

Commercially available frequency-domain terahertz spectrometer (Toptica Terascal 780) based on GaAs photo-mixer coupled with silicon lens was engaged in the experiments. Its operation range is within 0.1–2 THz, it delivers radiation of circular polarization of about 1  $\mu$ W power.

For the experiment a broadband photoconductive low-temperature grown gallium arsenide (LTG-GaAs) antenna coupled with silicon lens from time-domain spectrometer (Teravil, Ltd., Vilnius, Lithuania) was also used. The microbolometer was connected to the lock-in amplifier to modulate signal optically chopped at frequency of 500 kHz. The emitter was pumped with femtosecond Ti-Sapphire optical laser of 100 fs pulse duration and generating broadband THz pulses in frequency range of 0.1–2.5 THz with average emission power of 1.2  $\mu$ W. The THz beam was investigated by scanning it in the  $xy$  plane perpendicular to the direction of propagation with detector being fixed to  $xy$  motorized positioning stage. No additional focusing optical components are used in radiation measurements. In beam imaging recording, position synchronized raster scan technique was implemented similar to that described in Ref. [9]. Scanning parameters were selected to enable sufficient SNR with resolution up to  $0.1 \times 0.25 \text{ mm}^2$  which is comparable with the wavelength of upper frequency limit of emitted radiation (or the size of the microbolometer).

Optically pumped continuous-wave molecular THz laser FIRL-100 (Edinburg Instruments, Ltd., Livingston, United Kingdom) was used to generate discrete spectrum at 0.76 THz, 1.63 THz and 2.52 THz frequencies with corresponding powers of 1.6 mW, 1.6 mW and 7 mW, respectively. The emitted unfocused radiation was of 11 mm in diameter; the power was artificially reduced varying the power of optical pumping from 20 W down to 9.8 W range.



The absolute power was measured using a calibrated power meter (Thomas Keating Absolute Power Meter System, Version 2, Thomas Keating Ltd., Billingshurst, West Sussex, UK).

Commercially available pyroelectric sensor SPH62 THz with 2 mm<sup>2</sup> active area from Spectrum Detector Inc. was used in the experiments.

All experiments were conducted in the ambient air conditions.

## 5. Conclusions

Versatile operation of universal, convenient and easy-to-use antenna coupled sensitive titanium-based microbolometers dedicated to the precise alignment and the control of spatial mode profiles without additional focusing optical components of weak power THz sources are demonstrated. Spatial mode profile control and polarization-resolved mode structures are recorded for different type THz emitters—electronic multiplier sources, optical THz mixers-based frequency domain and femtosecond optoelectronic THz time-domain spectrometers as well as optically pumped molecular THz laser—operating either in continuous wave or pulsed modes. Features of the microbolometers coupled with resonant antennas within 0.15–0.6 THz range are exposed and discussed, and their ability to detect spatial mode profiles far above the antennas resonances, up to 2.54 THz, are explored as well. It is found that a broadband antenna (below 1 THz) coupled microbolometer reproduces well the spatial mode profile of time-domain spectrometer. Polarization-sensitive mode control possibilities are examined in details; suitability of the resonant antenna-coupled bolometers to resolve low-absorbing objects at 0.3 THz is revealed via direct, dark field and phase contrast imaging techniques. The microbolometer, for instance, coupled with a 0.3 THz frequency dipole antenna exhibits the response time of 1 μs range, sensitivity of 300 V/W, and noise-equivalent power of 14 pW/√Hz. Microbolometers display corresponding values of 200 kV/W and less than 20 pW/√Hz, respectively, and the response time in the 5 μs range. These parameters make the devices promising for real-time fine adjustment of THz spectroscopic and imaging systems as well as imaging applications and inspection of low-absorbing objects.

**Author Contributions:** Conceptualization of the research, G.V. and L.M.; methodology, G.V., L.M. and A.S. (Agnieszka Siemion); software, D.J.; development of antenna-coupled Ti-microbolometers, A.S. (Aleksander Sešek), A.S., I.K., and J.T.; investigation using electronic sources, L.M., A.S. (Agnieszka Siemion), L.Q. and D.J.; investigation using frequency domain spectrometer, D.S.; investigation using THz time-domain spectrometer, I.K.; investigation using optically-pumped molecular THz laser, D.S., L.Q., and L.M.; data acquisition, L.M. and G.V.; experimental data analysis, L.M., A.S. (Agnieszka Siemion), L.Q., and G.V.; writing—original draft preparation, G.V.; writing—review and editing, L.M., A.S. (Agnieszka Siemion), I.K. and G.V.; visualization, L.M., A.S. (Agnieszka Siemion), L.Q., and D.J.; supervision and coordination, G.V.; project administration, G.V. All authors have read and agreed to the published version of the manuscript.

**Funding:** L.M. and I.K. acknowledge financial support from “KOTERA-PLAZA” project supported from European Regional Development Fund (Grant No. 01.2.2-LMT-K-718-01-0047).

**Acknowledgments:** Authors are very grateful to Rimvydas Venckevičius and Ramūnas Adomavičius for their kind assistance in experiments with femtosecond optoelectronic THz emitters and for illuminating discussions.

**Conflicts of Interest:** The authors declare no conflict of interest.

## Abbreviations

The following abbreviations are used in this manuscript:

THz	Terahertz
THz ELS	Terahertz electronic multiplier source
THz FDS	Terahertz frequency domain spectrometer
THz TDS	Terahertz time domain spectrometer
THz OPML	Optically pumped molecular THz laser
Ti-mB	titanium-based microbolometer
CW	continuous wave
SNR	Signal-to-noise ratio
Ksps	Kilo samples per second

## References

1. Mittleman, D.M. Twenty years of terahertz imaging [Invited]. *Opt. Express* **2018**, *26*, 9417. [[CrossRef](#)] [[PubMed](#)]
2. Son, J.H.; Oh, S.J.; Cheon, H. Potential clinical applications of terahertz radiation. *J. Appl. Phys.* **2019**, *125*. [[CrossRef](#)]
3. Puc, U.; Abina, A.; Jeglič, A.; Zidanšek, A.; Kašalynas, I.; Venckevičius, R.; Valušis, G. Spectroscopic Analysis of Melatonin in the Terahertz Frequency Range. *Sensors* **2018**, *18*, 4098. [[CrossRef](#)]
4. Sun, Q.; He, Y.; Liu, K.; Fan, S.; Parrott, E.P.; Pickwell-MacPherson, E. Recent advances in terahertz technology for biomedical applications. *Quant. Imaging Med. Surg.* **2017**, *7*, 345–355. [[CrossRef](#)] [[PubMed](#)]
5. Trofimov, V.A.; Varentsova, S.A. A possible way for the detection and identification of dangerous substances in ternary mixtures using thz pulsed spectroscopy. *Sensors* **2019**, *19*, 2365. [[CrossRef](#)] [[PubMed](#)]
6. Palka, N.; Szala, M. Transmission and Reflection Terahertz Spectroscopy of Insensitive Melt-Cast High-Explosive Materials. *J. Infrared Millimeter Terahertz Waves* **2016**, *37*, 977–992. [[CrossRef](#)]
7. Puc, U.; Abina, A.; Rutar, M.; Zidanšek, A.; Jeglič, A.; Valušis, G. Terahertz spectroscopic identification of explosive and drug simulants concealed by various hiding techniques. *Appl. Opt.* **2015**, *54*, 4495. [[CrossRef](#)] [[PubMed](#)]
8. Bauer, M.; Venckevičius, R.; Kašalynas, I.; Boppel, S.; Mundt, M.; Minkevičius, L.; LISAUSKAS, A.; Valušis, G.; Krozer, V.; Roskos, H.G. Antenna-coupled field-effect transistors for multi-spectral terahertz imaging up to 4.25 THz. *Opt. Express* **2014**, *22*, 19235. [[CrossRef](#)]
9. Kasalynas, I.; Venckevičius, R.; Valušis, G. Continuous Wave Spectroscopic Terahertz Imaging With InGaAs Bow-Tie Diodes at Room Temperature. *IEEE Sens. J.* **2013**, *13*, 50–54. [[CrossRef](#)]
10. Minkevičius, L.; Tamošiūnas, V.; Kašalynas, I.; Seliuta, D.; Valušis, G.; LISAUSKAS, A.; Boppel, S.; Roskos, H.G.; Köhler, K. Terahertz heterodyne imaging with InGaAs-based bow-tie diodes. *Appl. Phys. Lett.* **2011**, *99*, 131101. [[CrossRef](#)]
11. Murate, K.; Kawase, K. Perspective: Terahertz wave parametric generator and its applications. *J. Appl. Phys.* **2018**, *124*, 160901. [[CrossRef](#)]
12. Trofimov, V.A.; Varentsova, S.A.; Zakharova, I.G.; Zagursky, D.Y. New possibilities of substance identification based on THz time domain spectroscopy using a cascade mechanism of high energy level excitation. *Sensors* **2017**, *17*, 2728. [[CrossRef](#)]
13. Abina, A.; Puc, U.; Jeglič, A.; Prah, J.; Venckevičius, R.; Kašalynas, I.; Valušis, G.; Zidanšek, A. Qualitative and quantitative analysis of calcium-based microfillers using terahertz spectroscopy and imaging. *Talanta* **2015**, *143*, 169–177. [[CrossRef](#)] [[PubMed](#)]
14. Tamošiūnas, V.; Minkevičius, L.; Vaitkunas, A.; Urbanowicz, A.; Maneikis, A.; Šetkus, A.; Valušis, G. Characterization of Silicon Solar Cells and Module Materials Using Terahertz Radiation. *Energy Procedia* **2015**, *77*, 202–207. [[CrossRef](#)]
15. Siemion, A. Terahertz Diffractive Optics—Smart Control over Radiation. *J. Infrared Millimeter Terahertz Waves* **2019**, *40*, 477–499. [[CrossRef](#)]
16. Molloy, J.F.; Naftaly, M.; Dudley, R.A. Characterization of terahertz beam profile and propagation. *IEEE J. Sel. Top. Quantum Electron.* **2013**, *19*, 8401508. [[CrossRef](#)]
17. Bitman, A.; Lumer, Y.; Moshe, I.; Zalevsky, Z. Characterization of spectrally broadband terahertz beam propagation. *J. Opt. Soc. Am. B* **2012**, *29*, 1436. [[CrossRef](#)]
18. Molloy, J.; Naftaly, M.; Dudley, R. Characterisation of Terahertz Beam Profile and Propagation through Complex Quasi-Optic Systems. *Terahertz Sci. Technol.* **2011**, *4*, 99–103. [[CrossRef](#)]
19. Jokubauskis, D.; Minkevičius, L.; Karaliūnas, M.; Indrišiūnas, S.; Kašalynas, I.; Račiukaitis, G.; Valušis, G. Fibonacci terahertz imaging by silicon diffractive optics. *Opt. Lett.* **2018**, *43*, 2795. [[CrossRef](#)]
20. Minkevičius, L.; Jokubauskis, D.; Kašalynas, I.; Orlov, S.; Urbas, A.; Valušis, G. Bessel terahertz imaging with enhanced contrast realized by silicon multi-phase diffractive optics. *Opt. Express* **2019**, *27*, 36358. [[CrossRef](#)]
21. Oda, N. Détecteur matriciel de type bolométrique à température ambiante et camera vidéo pour l'imagerie térahertz. *C. R. Phys.* **2010**, *11*, 496–509. [[CrossRef](#)]
22. Oden, J.; Meilhan, J.; Lalanne-Dera, J.; Roux, J.F.; Garet, F.; Coutaz, J.L.; Simoens, F. Imaging of broadband terahertz beams using an array of antenna-coupled microbolometers operating at room temperature. *Opt. Express* **2013**, *21*, 4817. [[CrossRef](#)] [[PubMed](#)]

23. Trontelj, J.; Valušis, G.; Venckevičius, R.; Kašalynas, I.; Sešek, A.; Švigelj, A. A high performance room temperature THz sensor. *Terahertz Emit. Receiv. Appl. V* **2014**, *9199*, 91990K. [[CrossRef](#)]
24. Sešek, A.; Švigelj, A.; Trontelj, J.; A compact THz imaging system. In *Image Sensors and Imaging Systems 2015*; Widenhorn, R., Dupret, A., Eds.; SPIE: San Francisco, CA, USA, 2015; pp. 7–14. [[CrossRef](#)]
25. Trontelj, J.; Sešek, A.; Electronic terahertz imaging for security applications. In *Terahertz, RF, Millimeter, and Submillimeter-Wave Technology and Applications IX*; Sadwick, L.P., Yang, T., Eds.; SPIE: San Francisco, CA, USA, 2016; pp. 161–166. [[CrossRef](#)]
26. Kašalynas, I.; Venckevičius, R.; Minkevičius, L.; Sešek, A.; Wahaia, F.; Tamošiūnas, V.; Voisiat, B.; Seliuta, D.; Valušis, G.; Švigelj, A.; et al. Spectroscopic Terahertz Imaging at Room Temperature Employing Microbolometer Terahertz Sensors and Its Application to the Study of Carcinoma Tissues. *Sensors* **2016**, *16*, 432. [[CrossRef](#)]
27. Krotkus, A. Semiconductors for terahertz photonics applications. *J. Phys. D Appl. Phys.* **2010**, *43*, 273001. [[CrossRef](#)]
28. Kašalynas, I.; Venckevičius, R.; Tumonis, L.; Voisiat, B.; Seliuta, D.; Valušis, G.; Račiukaitis, G. Reflective terahertz imaging with the TEM01 mode laser beam. *Appl. Opt.* **2013**, *52*, 5640–5644. [[CrossRef](#)]
29. Jokubauskis, D.; Minkevičius, L.; Seliuta, D.; Kašalynas, I. Terahertz homodyne spectroscopic imaging of concealed low-absorbing objects. *Opt. Eng.* **2019**, *58*, 023104. [[CrossRef](#)]
30. Hall, C.E. Dark-field electron microscopy. I. Studies of crystalline substances in dark-field. *J. Appl. Phys.* **1948**, *19*, 198–212. [[CrossRef](#)]
31. Hargather, M.J.; Settles, G.S. Natural-background-oriented schlieren imaging. *Exp. Fluids* **2010**, *48*, 59–68. [[CrossRef](#)]
32. Zernike, F. Diffraction theory of the knife-edge test and its improved form, the phase-contrast method. *Mon. Not. R. Astron. Soc.* **1934**, *94*, 377–384. [[CrossRef](#)]
33. Zernike, F. Diffraction theory of the knife-edge test and its improved form: The phase-contrast method. *J. Micro/Nanolithogr. MEMS MOEMS* **2002**, *1*, 87–95. [[CrossRef](#)]
34. Huhn, A.K.; Spickermann, G.; Ihring, A.; Schinkel, U.; Meyer, H.G.; Haring Bolívar, P. Uncooled antenna-coupled terahertz detectors with 22  $\mu$ s response time based on BiSb/Sb thermocouples. *Appl. Phys. Lett.* **2013**, *102*, 121102. [[CrossRef](#)]
35. Kašalynas, I.; Seliuta, D.; Simniškis, R.; Tamošiūnas, V.; Köhler, K.; Valušis, G. Terahertz imaging with bow-tie InGaAs-based diode with broken symmetry. *Electron. Lett.* **2009**, *45*, 833–835. [[CrossRef](#)]



© 2020 by the authors. Licensee MDPI, Basel, Switzerland. This article is an open access article distributed under the terms and conditions of the Creative Commons Attribution (CC BY) license (<http://creativecommons.org/licenses/by/4.0/>).

Vilniaus universiteto leidykla  
Saulėtekio al. 9, LT-10222 Vilnius  
El. p. [info@leidykla.vu.lt](mailto:info@leidykla.vu.lt),  
[www.leidykla.vu.lt](http://www.leidykla.vu.lt)  
Tiražas 20 egz.